

Effect of Iron Oxidation State and Annealing Atmosphere on Functional Properties of Zinc Oxide Thin Films

By:

Miguel Angel Santiago Rivera

A thesis submitted in partial fulfillment of the requirements for the degree of

MASTER OF SCIENCE
in
PHYSICS

UNIVERSITY OF PUERTO RICO
MAYAGÜEZ CAMPUS

2019

Approved by:

Oscar Perales-Pérez, Ph.D.
President, Graduate Committee

Date

Sergyi Lysenko, Ph.D.
Member, Graduate Committee

Date

Samuel Santana Colón, Ph.D.
Member, Graduate Committee

Date

Rocío Zapata Medina, M.A.
Representative of Graduate School

Date

Rafael Ramos Maldonado, Ph.D.
Chair, Department of Physics

Date

ABSTRACT

The ability to produce high-quality single-phase diluted magnetic semiconductors (DMS) is the driving factor to study DMS for spintronic applications. ZnO is a wide band gap semiconductor of the II-VI semiconductor group and exhibits several favorable properties. The effective incorporation of dopant species into ZnO host structure should induce changes in its physical and chemical properties enabling the establishment of novel functional properties. In the case of doping with transition metal ions, such as Fe ions, the subsequent exchange interaction from magnetic spins should induce a ferromagnetic behavior, but we found a paramagnetic response in our Fe doped ZnO thin films.

The present research addresses the study of the effect of the oxidation state of Fe species and the influence of the annealing atmosphere on the structural and functional properties of nanocrystalline ZnO thin films. We report structural, optical and magnetic properties of annealing temperature of paramagnetic Fe doped ZnO thin films, in a range of 500°C to 700°C. Fe-doped ZnO films samples were synthesized via a sol-gel approach. The produced $\text{Zn}_{(1-x)}\text{Fe}_x\text{O}$ nanoparticles at $[x = 0, 0.05, \text{ and } 0.07]$, films were grown on silicon wafer substrates.

The structural characterization was performed by X-Ray Diffraction (XRD) examination, Scanning Electron Microscope (SEM) and Transmission Electron Microscope (TEM) analysis to verify the formation of the ZnO host structure after annealing of the precursor phases. Incorporating Fe ions into ZnO did not affect the crystal structure of the wurtzite host. The variation of the average crystallite size of Fe [0-7 at. %] ZnO films annealed in nitrogen and air, in a range of 500°C to 700°C, were negligible and averaged between 10 nm to 20 nm. Also, the size of the particles was calculated using the Scherrer equation.

ZnO thin films prepared, have a hexagonal wurtzite structure based on XRD evidence, with crystals preferentially oriented along the c-axis. After 5 at% Fe is doped, the crystalline quality and the preferential orientation of ZnO thin film was improved. The results show that Fe atoms, were substituting Zn ions successfully due to the small ionic radius of Fe ions, compared to that of a Zn ion, the crystal size decreased with an increasing dopant concentration. There is no evidence of a secondary phase (Fe, FeO, Fe₂O₃ or ZnFe₂O₄). Hence, XRD and Photoluminescence spectroscopy (PL) measurements confirmed an enhanced crystallinity of the ZnO host, with an average crystallite size of 15 nm, for films annealed over 500°C in air and under a nitrogen atmosphere.

The optical properties of thin films were determined by Infrared, Ultraviolet–visible spectroscopy (UV-vis) and (PL) techniques. The results confirmed that the crystallinity of the ZnO is deteriorated due to the Fe-doping. Photoluminescence (PL) measurements corroborated the formation of high-quality ZnO host structure, in films annealed in air and controlled nitrogen atmospheres. Fe-incorporation hardly influences the transmittance in the visible range, however the optical band gaps of ZnO thin films gradually increase with the improved Fe-doping concentration. The PL spectrum displays that all of the samples have an ultraviolet emission peak centered at 388 nm. At, x = 0 at% thin film has the strongest ultraviolet emission peak, which decreased with increasing dopant percentage. As a result of the quenching by concentration effect attributed to the formation of trapping states by the dopant species. First principle calculations indicate that the oxidation states of iron are Iron (II) and Iron (III) with a zinc vacancy or an interstitial oxygen anion, respectively. The calculations predict that the exchange interaction between transition metal (TM) ions can switch from the antiferromagnetic (AFM) coupling into

its quasi-degenerate ferromagnetic coupling by external perturbations. This is further supported and explained the observed paramagnetic behavior at magnetic measurements.

Magnetic measurements revealed a paramagnetic signal comes from Fe ions doped ZnO crystals. Furthermore, introducing Fe into ZnO induces a magnetic moment without any distortion in the geometrical symmetry. M-H measurements evidenced a paramagnetic behavior at room temperature in films that were dependent on the type and amount of the dopant species.

RESUMEN

La capacidad de producir semiconductores magnéticos diluidos monofásicos de alta calidad (DMS) es el factor determinante para estudiar el DMS para aplicaciones espintrónicas. ZnO es un semiconductor de banda ancha del grupo de semiconductores II-VI y exhibe varias propiedades favorables. La incorporación efectiva de las especies dopantes en la estructura del huésped ZnO debería inducir cambios en sus propiedades físicas y químicas que permitan el establecimiento de nuevas propiedades funcionales. En el caso del dopaje con iones de metales de transición (TM), como los iones Fe, la interacción de intercambio posterior de los espines magnéticos debería inducir un comportamiento ferromagnético, pero encontramos una respuesta paramagnética.

La presente investigación aborda el estudio del efecto del estado de oxidación de las especies de Fe y la influencia de la atmósfera de recocido en las propiedades estructurales y funcionales de las películas delgadas de ZnO nanocristalinas. Informamos las propiedades estructurales, ópticas y magnéticas de la temperatura de recocido de películas delgadas de ZnO paramagnéticas con Fe, en un rango de 500°C a 700°C. Las muestras de películas de ZnO dopadas con Fe se sintetizaron a través de un enfoque sol-gel. Las nanopartículas de $Zn_{(1-x)}Fe_xO$ producidas en $[x = 0, 0.05 \text{ y } 0.07]$ at.% se cultivaron en sustratos de silicio.

La caracterización estructural se realizó mediante examen de Difracción de Rayos X (XRD), Microscopio Electrónico de Barrido (SEM) y Microscopio Electrónico de Transmisión (TEM) para verificar la formación de la estructura del huésped ZnO después del recocido de las fases precursoras. La incorporación de iones Fe en ZnO no afectó la estructura cristalina del huésped wurtzita.

La variación del tamaño promedio de cristalita de Fe [0-7 at. %] de las películas de ZnO recocidas en nitrógeno y aire, en un rango de 500°C a 700°C, fueron insignificantes y promediaron entre 10nm y 20nm. Las películas delgadas de ZnO preparadas tienen una estructura de wurtzita hexagonal basada en la evidencia XRD, con cristales orientados preferentemente a lo largo del eje c.

Después de dopar 5 at.% de Fe, se mejoró la calidad cristalina y la orientación preferencial de la película delgada de ZnO. Los resultados muestran que los átomos de Fe estaban sustituyendo con éxito los iones Zn debido al pequeño radio iónico de los iones Fe, en comparación con el de un ion Zn, el tamaño del cristal disminuyó al aumentar la concentración de dopante. No hay evidencia de una fase secundaria (Fe, FeO, Fe₂O₃ o ZnFe₂O₄). Por lo tanto, las mediciones de XRD y de espectroscopia de fotoluminiscencia (PL) confirmaron una cristalinidad mejorada del huésped ZnO, con un tamaño promedio de cristalino de 15 nm, para películas recocidas a más de 500°C en aire y bajo una atmósfera de nitrógeno.

Las propiedades ópticas de las películas delgadas se determinaron mediante infrarrojos, espectroscopia de luz ultravioleta (UV-vis) y técnicas (PL). Los resultados confirmaron que la cristalinidad de la ZnO se deteriora debido al dopaje con Fe. Las mediciones de fotoluminiscencia (PL) corroboraron la formación de una estructura huésped de ZnO de alta calidad, en películas recocidas en atmósferas de aire y nitrógeno controladas. La incorporación de Fe apenas influye en la transmitancia en el rango visible. Sin embargo, los intervalos de bandas ópticas de las películas delgadas de ZnO aumentan gradualmente con la concentración mejorada de dopaje con Fe. El espectro PL muestra que todas las muestras tienen un pico de emisión ultravioleta centrado en 388 nm. En, x = 0 at.% de película delgada tiene el pico de emisión ultravioleta más fuerte, que disminuyó al aumentar el porcentaje de concentración del dopante.

Como resultado de la extinción por efecto de la concentración del dopante, atribuida a la formación de estados trampa, por las especies dopantes. Los cálculos de primeros principios indican que los estados de oxidación del hierro son el hierro (II) y el hierro (III), con una vacante de zinc o un anión intersticial de oxígeno, respectivamente. Los cálculos predicen que la interacción de intercambio entre los iones de metal de transición (TM) puede cambiar del acoplamiento anti-ferromagnético (AFM) a su acoplamiento ferromagnético cuasi degenerado por perturbaciones externas. Esto se apoya y explica además el comportamiento paramagnético observado en las mediciones magnéticas.

Las mediciones magnéticas revelaron que una señal paramagnética proviene de los cristales de ZnO dopados con iones de Fe. Además, la introducción de Fe en ZnO induce un momento magnético sin distorsión en la simetría geométrica. Las mediciones de M-H evidenciaron un comportamiento paramagnético a temperatura ambiente en películas que dependían del tipo y la cantidad de la especie dopante.

Copyright © 2019
by
Miguel Ángel Santiago Rivera

DEDICATORY

To Jesus and to his holy mother, the Holy Virgin Mary for inspiring me to persevere, and to my daughter and wife for their patience throughout the past years.

A Jesús y a su santa madre, la Santísima Virgen María por inspirarme a perseverar, y a mi hija y esposa por su paciencia a lo largos de los pasados años.

ACKNOWLEDGMENTS

By this I want to thank the University of Puerto Rico at Mayagüez for giving me the opportunity to develop as a student and researcher, but also, I want to thank:

- ❖ To my advisor, Dr. Oscar Perales Perez for his motivation, guidance, scientific discussions, and the opportunity to work at the Material Science and Engineering Department.
- ❖ To Graduate Committee of the Department of Physics.
- ❖ Special thanks to Miss Gina Montes, M.S. for the collaboration in the Zinc Oxide research.
- ❖ To the Director of Dept. of Geology at UPRM, for the structural measurements by the XRD at the Earth X-ray Laboratory Center (EXACT!)
- ❖ Boris Rentería, M.S. for the training with some instruments at The NANO materials Processing Laboratory at UPRM.
- ❖ To the Material Characterization Center (MCC) at the UPR – Molecular Center, for SEM images.
- ❖ To Sonia Bailón, Ph.D. for the PL Measurements at UPR-Ponce

This material is based upon work supported by the DOE-Grant No. FG02-08ER46526.

TABLE OF CONTENTS

ABSTRACT	ii
RESUMEN	iv
COPYWRIGHT	viii
DEDICATORY	ix
ACKNOWLEDGEMENTS	x
TABLE OF CONTENTS	xi
LIST OF TABLES	xv
LIST OF FIGURES	xvi
1. INTRODUCTION	1
1.1 JUSTIFICATION	1
1.2 MOTIVATION	3
1.3 PURE AND DOPED ZINC OXIDE LITERATURE REVIEW	3
1.4 OBJECTIVES	8
1.4.1 Main	8
1.4.2 Specifics	8
1.5 CONTENTS OF THE THESIS	9
2. BACKGROUND	11
2.1 PURE AND DOPED ZnO SEMICONDUCTOR FILMS	11
2.1.1 An Overview of Zinc Oxide	11
2.1.1.1 ZnO Structural Properties	12

2.1.1.2	ZnO Optical Properties	15
2.1.2	ZnO Lattice Parameters	22
2.1.3	Structural Defects of ZnO	23
2.2	ZnO-DILUTED MAGNETIC SEMICONDUCTORS	25
2.2.1	Diluted Magnetic Semiconductor	25
2.2.2	Dilute Magnetic Semiconductor Oxide	26
2.3	Types of Magnetic Materials	30
2.4	Characterization Techniques	33
2.4.1	Films Thickness Determination	35
2.4.2	Structural Characterization	37
2.4.3	Optical Characterization.....	39
2.4.4	Magnetic Characterization	41
3.	EXPERIMENTAL	47
3.1	ZnO-Based Powder and Thin Films	47
3.1.1	Materials	47
3.1.2	Synthesis of Powders	47
3.1.3	Synthesis of Thin Films	48
4.	RESULTS AND DISCUSSION	49
4.1	Zinc Oxide Nanoparticles	49
4.1.1	Structural Properties of ZnO	49
4.1.2	Optical Properties of ZnO Thin Films	60

4.1.3 Remarks	63
4.2 Fe (II)-ZnO Thin Films Annealed in Air	64
4.2.1 Structural Properties	64
4.2.2 Optical Properties	69
4.2.3 Magnetic Properties	74
4.2.4 Remarks	77
4.3 Fe (II) - ZnO with Thin Films Annealed in Nitrogen Atmosphere .	79
4.3.1 Structural Properties	79
4.3.2 Optical Properties	82
4.3.3 Magnetic Properties	85
4.3.4 Remarks	85
4.4 Fe (III) - ZnO Thin Films Annealed in Air	88
4.4.1 Structural Properties	88
4.4.2 Optical Properties	90
4.4.3 Magnetic Properties	93
4.4.4 Remarks	96
4.5 Fe (III) - ZnO Thin Films Annealed in Nitrogen Atmosphere	97
4.5.1 Structural Properties	97
4.5.2 Optical Properties	99
4.5.3 Magnetic Properties	101
4.5.4 Remarks	103
5. CONCLUSIONS	104

6. REFERENCES 108

LIST OF TABLES

Table 1: Properties of different semiconductor oxides	28
Table 2: Average crystallite size of Pure ZnO thin films in air and N ₂ atm	51
Table 3: Average crystallite size of Fe (II)-ZnO thin films in air	67
Table 4: Average crystallite size of Fe (II)-ZnO thin films in N ₂ atm	79
Table 5: Average crystallite size of Fe (III)-ZnO NP's thin films in air	90
Table 6: Average crystallite size of Fe (III)-ZnO NP's thin films in N ₂ atm	97

LIST OF FIGURES

1. Figure – 1: Schematic of Sol-Gel, chemical process	3
2. Figure – 2: Wurtzite Hexagonal Crystal Structure of Zinc Oxide.....	11
3. Figure – 3: ZnO Atomic Wurtzite Structure.....	14
4. Figure – 4: The optical absorption due to a direct transition from a valence band state to a conduction band state	16
5. Figure – 5: The schematic of non-radiative electron-hole recombination.....	17
6. Figure – 6: Limiting types of excitons	19
7. Figure – 7: Exciton levels in relation to the conduction band edge	20
8. Figure – 8: Energy levels of an exciton created in a direct process.....	21
9. Figure – 9: Structural Defects in Zinc Oxide.....	24
10. Figure – 10: Computational values of the temperature for semiconductors.....	27
11. Figure – 11: of the temperature as a function of the energy gap of several Semiconductors.....	29
12. Figure – 12: Alignment of the magnetic dipoles for different types of magnetism: (a) Ferromagnetism, (b) Antiferromagnetic, (c) Ferrimagnetism.....	31
13. Figure – 13: Material characterization for structural, optical and magnetic prop.	34
14. Figure – 14: Schematic Ellipsometry technique.....	36
15. Figure – 15: Reflection of X-rays from different atomic planes.....	38
16. Figure – 16: Schematic representation of photoluminescence (PL) Measurement.....	40
17. Figure – 17: Schematic representation of a VSM's coils.....	42

18. Figure – 18: a) Virgin curve, b) Hysteresis loop of a ferromagnetic material...	45
19. Figure – 19: Flow chart of the synthesis process of pure and Iron- doped ZnO Thin Films by Sol-gel method.....	49
20. Figure – 20: Figure – 20: (A) XRD for Pure ZnO annealed at different temperatures in air, (B) ZnO XRD Data JCPDS Card No.36-1451.....	52
21. Figure – 21: (A) XRD for Pure ZnO annealed at different temperatures in controlled nitrogen atmosphere. (B) ZnO XRD Data JCPDS Card No.36-1451.....	53
22. Figure – 22: XRD of Pure ZnO powder and thin films samples annealed in air at 500°C for one hour.....	55
23. Figure – 23: XRD of Pure ZnO powder and thin films samples annealed in N ₂ atmosphere at 500°C for one hour.....	55
24. Figure – 24: XRD of Pure ZnO powder and thin films samples annealed in air at 700°C for one hour.....	56
25. Figure – 25: XRD of Pure ZnO powder and thin films samples, annealed in N ₂ atmosphere at 700°C for one hour.....	56
26. Figure – 26: SEM images showing the morphology of pure ZnO film (a) annealed in air at 700°C (b) annealed in nitrogen-controlled atmosphere at 700°C.....	58
27. Figure – 27: TEM images showing the morphology of pure ZnO powder annealed at 700°C.....	59
28. Figure – 28: Room temperature PL spectra for Pure ZnO annealed at a range temperature between 500°C and 700°C in air.....	62
29. Figure – 29: Room temperature PL spectra for Pure ZnO annealed at a range temperature between 500°C and 700°C in N ₂ atmosphere	62

30. Figure – 30: XRD for Fe (II)-ZnO thin films annealed at 500°C in air.....	64
31. Figure – 31: XRD for Fe (II)-ZnO thin films annealed at 700°C in air.....	66
32. Figure – 32: SEM images of Fe (II)-ZnO at annealed at 700°C in air; (a) 5% dopant concentration and (b) 7% dopant concentration.....	68
33. Figure – 33: Room tempt. PL spectra for Fe (II)-ZnO annealed at 500°C in air..	69
34. Figure – 34: Room tempt. PL spectra for Fe (II)-ZnO annealed at 700°C in air..	71
35. Figure – 35: Room temperature PL Relative intensity Fe (II)-ZnO in air.....	73
36. Figure – 36: Room temperature M-H loop for Fe (II)-ZnO thin films annealed at 500°C in air.....	75
37. Figure – 37: Room temperature M-H loop for Fe (II)-ZnO thin films annealed at 700°C in air.....	75
38. Figure – 38: XRD for Fe (II)-ZnO thin films annealed at 500°C in N ₂ atmosphere	80
39. Figure – 39: XRD for Fe (II)-ZnO thin films annealed at 700°C in N ₂ atmosphere	80
40. Figure – 40: SEM images of Fe (II)-ZnO at annealed at 700C in nitrogen atmosphere; (a) 5% dopant concentration and (b) 7% dopant concentration	81
41. Figure – 41: Room temperature PL spectroscopy for Fe (II)-ZnO annealed at 500°C in N ₂ atmosphere.....	83
42. Figure – 42: Room temperature PL Relative intensity Fe(II)-ZnO in N ₂ atm.....	83
43. Figure – 43: PL spectroscopy for Fe (II)-ZnO annealed at 700°C in N ₂ atm.....	84
44. Figure – 44: Room temperature M-H loop for Fe (II)-ZnO at 500°C in N ₂ atm....	86
45. Figure – 45: Room temperature M-H loop for Fe (II)-ZnO at 700°C in N ₂ atm....	86
46. Figure – 46: XRD for Fe (III)-ZnO thin films annealed at 500°C in air.....	89
47. Figure – 47: XRD for Fe (III)-ZnO thin films annealed at 700°C in air.....	89

48. Figure – 48: PL spectra for Fe (III)-ZnO TF annealed at 500°C in air.....	91
49. Figure – 48: PL spectra for Fe (III)-ZnO TF annealed at 700°C in air.....	91
50. Figure – 50: PL relative intensity for Fe(III)-doped ZnO thin films in air.....	93
51. Figure – 51: M-H loop for Fe (III)-ZnO thin films annealed at 500°C in air.....	94
52. Figure – 52: M-H loop for Fe (III)-ZnO thin films annealed at 700°C in air.....	95
53. Figure – 53: XRD for Fe (III)-ZnO thin films annealed at 500°C in N ₂ atmosphere	98
54. Figure – 54: XRD for Fe (III)-ZnO thin films annealed at 700°C in N ₂ atmosphere	98
55. Figure – 55: PL spectra for Fe (III)-ZnO thin films annealed at 500°C N ₂ atmos...	99
56. Figure – 56: PL spectra for Fe (III)-ZnO thin films annealed at 700°C in N ₂ atmos.	100
57. Figure – 57: Room-temperature PL relative intensity for Fe ³⁺ -ZnO thin films.....	101
58. Figure – 58: Room temperature M-H loop for Fe (III)-ZnO thin films annealed at 500°C in N ₂ atmosphere.....	102
59. Figure – 59: Room temperature M-H loop for Fe (III)-ZnO thin films annealed at 700°C in N ₂ atmosphere.....	102

1 INTRODUCTION

1.1 JUSTIFICATION

Industry and academia have a strong interest in the application of the material semiconductors. Both sectors have been pursuing to improve semiconductor materials for applications in data storage, spintronic-based devices, etc. Among various semiconductor oxides that are expected to become suitable platforms for multifunctional applications, zinc oxide (ZnO) is one of the most attractive alternatives.

ZnO is a wide-bandgap semiconductor, having a hexagonal wurtzite structure with lattice parameters $a = 3.249 \text{ \AA}$ and $c = 5.207 \text{ \AA}$. This semiconductor oxide has several favorable properties, including good transparency, high electron mobility, and a wide band gap of 3.3 eV at room temperature, and strong luminescence at room-temperature, too. Those properties are used in emerging applications for transparent electrodes in liquid crystal displays, in energy-saving or heat-protecting windows, and in electronics as thin-film transistors, and light-emitting diodes (LED's).

The effective incorporation of dopant species into ZnO host structure induces changes in its physical and chemical properties enabling the establishment of novel multi-functional properties. In the case of doping with transition metal ions, such as Fe, Mn and V ions, the subsequent exchange interaction between available spins of the magnetic species were expected to induce a ferromagnetic behavior in the so-called ZnO-based diluted magnetic semiconductor. This ferromagnetic functionality would enable the application of this material in data storage and in spintronic-based devices.

Nevertheless, among the acceptor impurities that could affect in ZnO, nitrogen is thought to be considered the most suitable p-type dopant due to both atomic-size and electronic-structure considerations. The energy of the valence 2p states and the electronegativity of nitrogen are also the closest to those of the oxygen atom, particularly when compared with other column-V dopants [10]. Several groups have reported on the incorporation of N in ZnO, and many have claimed that N substitutes for O. Because the nitrogen atom is the closest in atomic size to oxygen, therefore, it is expected to result in minimum strain in ZnO.

Thus, for the purpose of the influence of oxidant state of the dopants and the annealing atmosphere in air, and an inert gas, e.g. nitrogen, should be investigated. Because, nitrogen seems to be the best acceptor of group V elements, since nitrogen has nearly the same radius as oxygen and is the shallowest acceptor. A first principle investigation by Van de Walls suggests that the simultaneous incorporation of nitrogen may be beneficial for achieving p-type doping in ZnO [20].

Regarding the syntheses approaches, the sol-gel method route is relatively simple, easy-to-scale and allows the synthesis of well crystallized powders and films. Sol-gel is a wet-chemical process that involves the formation of an inorganic colloidal suspension (sol) and gelation of the sol in a continuous liquid phase (gel) to form a three-dimensional network structure, see Figure – 1. The precursors for synthesizing colloidal sols consist of organometallic compounds surrounded by reactive functional groups. Sol-gels can be in the form of films, particles, fibers, aerogels and dense materials at micro- and nanoscale following a heat treatment. Initially are amorphous, so the crystalline sol-gel products can be achieved using appropriate heat treatments.

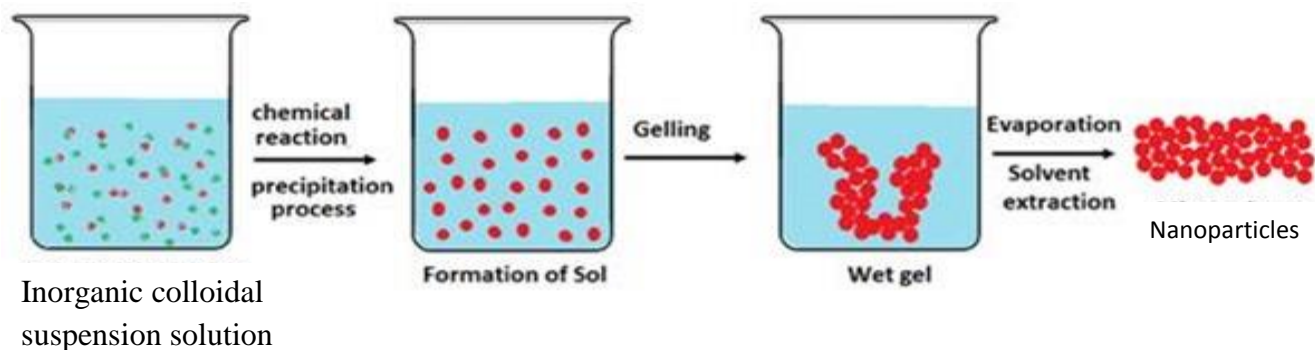


Figure – 1: Schematic of Sol-Gel, chemical process [109].

The range of applications of sol–gel, derived products in the industry continuously expand because of their resulting strength, density and chemical inertness. One of the largest applications is thin-film coating, which can be produced by spin-coating, spray-coating, roll-casting, electrophoresis and dipping.

On the above basis, this thesis is focused on the development of a modified sol-gel technique where the film growth has been improved by proper selection of viscosity-controlling additives, such as MEA, in precursor sol for spin-coating, for the best control of thickness by layer deposition. ZnO will be doped with different transition metal ions, e. g. Fe^{+2} and Fe^{+3} , to study their structural, optical and magnetic properties as a function of the type and amount of dopant and the thermal treatment temperature and time. Also, we want to investigate the effect of the structural defects on the functional properties of nanocrystalline ZnO powders and thin films under controlled nitrogen or air atmosphere.

1.2 MOTIVATION

Based on the available information, our research addresses a systematic study of the structural, optical and magnetic properties of ZnO, as a function of the type of Iron (II) and Iron (III) species and of their dopant concentration, as well as the effect of the annealing atmosphere. The main challenge was the development of suitable sol-gel based synthesis protocols to optimize the synthesis conditions for pure and doped Fe ions ZnO powders and thin films. We expected to control functional properties by tuning the effect of dopant oxidation defect on. By annealing with nitrogen atmosphere (inert gas) we expect to prevent oxide formation and reduce oxides on the films surface.

1.3 PURE AND DOPED ZINC OXIDE- LITERATURE REVIEW

Doping of ZnO with transition metals or rare earth ions would generate magnetic and magneto-optical behavior with the possibility of making it a room-temperature dilute magnetic semiconductor (DMS). DMS's materials have been the subject of diverse studies oriented towards the development of ZnO-based spintronic devices that would operate based on a quantum mechanical property of electrons called "spin" rather than on the electron's electrical charge.

The quantum properties of superposition and entanglement may someday permit quantum computers to perform certain types of computations much more quickly using less power than the required by conventional charge-based devices.

ZnO thin films have been synthesized by different techniques, including sputtering, chemical vapor deposition, pulsed laser deposition, and sol- gel processes.

The dopants were chosen based on of the size compatibility with Zn species in the host oxide lattice as well as their availability of d-electrons that would contribute with magnetic moments in the semiconductor host.

The nitrogen atom is the closest in atomic size to oxygen and, therefore, it is expected to result in minimum strain in ZnO. However, the reports on p-type conductivity in N-doped ZnO still remain controversial. Nitrogen is a shallow acceptor in other II–VI semiconductors and has been considered as a suitable p-type dopant for ZnO for some time.

Minegishi reported p-type doping of ZnO films grown on sapphire (0 0 0 1) by chemical vapor deposition, using NH₃ as nitrogen source [76]. Minegishi reported a carrier concentration of $1.5 \times 10^{16} \text{ cm}^{-3}$ with estimated ionization energy of 100 meV and Hall mobility of $12 \text{ cm}^2 \text{ V}^{-1} \text{ s}^{-1}$. He also proposed that hydrogen may play a role in the nitrogen incorporation, and that the appropriate growth/annealing conditions for obtaining p-type material are limited to such a narrow range that control turns out to be very difficult. Thonke performed photoluminescence spectroscopy measurements at low temperatures on ZnO bulk single crystals that were grown using the seeded chemical vapor transport (SCVT) technique by Eagle-Picher[76]. They derived an acceptor binding energy of 195 meV based on an analysis of donor–acceptor pair transitions, and assigned it to NO. ZnO single crystals in the experiments by Thonke were not intentionally doped, but were supposed to contain nitrogen. Carlos have reported EPR signals for NO in ZnO single crystals from Eagle-Picher, finding g values $g_{||} = 1.9953$ and $g_{\perp} = 1.9633$. [41]

These values seem to be in reasonable agreement with the observations by Garces who reported $g_{||} = 1.9948$ and $g_{\perp} = 1.9632$. The large anisotropy in the hyperfine interaction was

attributed by Carlos to a Jahn–Teller distortion along the c axis away from the substitutional site, that would make N a deep acceptor in ZnO. [76]

Guo, reported the growth of LED structures with nitrogen-doped ZnO films using plasma-enhanced laser deposition. The films were grown on n-type ZnO single crystal wafers, using N₂O as nitrogen source in the N-doped ZnO layer. Four-probe van der Pauw measurements showed a relatively high resistivity of 100–200 cm, which led Guo to suggest that N introduces a relatively deep level in ZnO. The observed bluish emission observed in the electroluminescence measurements by Guo is consistent with sub-band-gap recombination. [1]

Look *et al.* investigated the electrical and optical properties of N-doped ZnO grown by molecular-beam epitaxy on Li-diffused semi-insulating ZnO bulk single crystals from Eagle-Picher. Nitrogen was incorporated by using a flux of N₂ gas added to the O₂ gas flow in the RF plasma source [101].

Hall-effect and conductivity measurements resulted in a hole concentration of 9×10^{16} cm⁻³, mobility of $2 \text{ cm}^2 \text{ V}^{-1} \text{ s}^{-1}$, and resistivity of 40 cm. Photoluminescence measurements at 2K revealed a peak at 3.315 eV, which was attributed to a bound-exciton to neutral–acceptor recombination. Based on the band gap of 3.437 eV for ZnO at 2 K and a donor binding energy of 60 meV, and a LO-phonon replica at 3.238 eV supposedly related to the 3.315 eV peak, Look estimated the acceptor ionization energy to be 0.17–0.20 eV. They also noted that the high ionization energy and relatively low holes concentration are consistent with secondary-ion mass spectroscopy measurements which showed N concentrations of about 10^{19} cm^{-3} in the N-doped films, approximately two orders of magnitude higher than the ionized acceptor concentration.

Meyer performed photoluminescence measurements in nitrogen-implanted ZnO bulk crystals from Eagle-Picher and from CRYSTEC, as well as N-doped ZnO epitaxial films grown by vapor phase deposition (CVD) using NH₃ as the nitrogen source. The appearance of a donor–acceptor recombination at 3.235 eV after implantation and activation (annealing at 950°C), instead of a peak at 3.315 eV as reported by Look. [101]

Tsukazaki reported the realization of a ZnO LED by laser MBE on insulating ScAlMgO₄. The p-type N-doped layer was grown by a repeated temperature modulation technique in which 15 nm high-N-concentration layers were grown at low temperatures (~450°C), then annealed at higher temperatures, followed by 1 nm low-N-concentration layers at high temperatures (~1050 °C). The whole process was intended to lead to an overall high N incorporation in the N-doped layer. [41] Tsukazaki also reported blue light emission from a p–n ZnO homo-junction using N as the acceptor in the p-type layer, and estimated the holes mobility and acceptor activation energy as 5–8 cm² V⁻¹ s⁻¹ and 100 meV, respectively [41].

However, it is important to note that the band gap of ZnO is 3.4 eV and, as such, one should expect UV light emission from a ZnO p–n junction. As in the case of previous reports on N-doped ZnO, the work of Tsukazaki was not followed up with further developments, leading to doubts on the reliability and reproducibility of the p-type doping. [41]

The compensation of nitrogen substitutional acceptors by intrinsic defects as well as by nitrogen incorporated in different configurations has been theoretically investigated by Lee [76]. Based on calculations using density functional theory (DFT) and Local Density Approximation (LDA), they concluded that a low N doping level would result from N incorporation using a normal N₂ source, with the N acceptors being compensated mainly by oxygen vacancies. At high doping

levels, N acceptors would be compensated via the formation of defect complexes with Zn antisites. Also, if a N_2 plasma is used to increase the nitrogen incorporation (due to an increased N chemical potential), N acceptors would still be compensated by N_2 molecules at oxygen sites $[(N_2) O]$ and $NO-(N_2) O$ complexes, which would explain the difficulty in achieving low-resistivity p-type ZnO.

On the other hand, recent first-principles calculations by Fons indicate that nitrogen does not predominantly incorporate in the form of $(N_2) O$ when a plasma source is used. Instead, a comparison between N K-edge X-ray absorption spectra and results from first-principles calculations indicates that nitrogen incorporates substituting on O sites, where it is expected to act as an acceptor. Moreover, annealing at relatively high temperatures (800°C) may lead to the formation of N_2 bubbles, suggesting that the incorporation of high concentrations of 10^{20} cm^{-3} NO in ZnO can be achieved only in a metastable mode [76].

For Lee, it is important to note that the mechanism of compensation of NO acceptors in ZnO is still under debate. For instance, the $\epsilon(0^-)$ transition level (or ionization/binding energy) of NO at 0.44 eV above the valence-band maximum as predicted by Lee et al is too high for a shallow acceptor [68]. More importantly, this carries a large uncertainty, mainly due to the band gap underestimation by the standard DFT-LDA approach. That is, even the shallow/deep nature of the NO acceptor is not well established, and more sophisticated methods will be necessary to elucidate the electronic structure of N in ZnO. Hence, few research groups have studied the characteristics of Fe-doped ZnO films synthesized by various physical and chemical techniques like RF and DC magnetron sputtering, sol-gel, spray pyrolysis, hydrothermal process, electro-deposition and dip coating technique [68].

In general, the efficiency of the dopant element depends on its electronegativity and difference between dopant ionic radius and zinc ionic radius. Therefore, out of these transition metal dopants, iron (Fe) is chemically stable and exists in two possible oxidation states, Fe^{2+} and Fe^{3+} having ionic radii (0.76 Å and 0.64 Å) close to ionic radius of Zn^{2+} (0.74 Å). Thus, it can easily enter into Zn lattice sites either substitutionally or interstitially without disturbing the crystal structure of ZnO and can contribute more charge carriers in order to improve the multifunctional properties, [68].

1.4 OBJECTIVES

1.4.1 Main – Determine the effect of dopant oxidation state and annealing atmosphere on the functional properties of ZnO based nanostructured thin films as a function of structure, and composition.

1.4.2 Specifics

1.4.2.1 Synthesize films via a sol-gel technique, to increase the viscosity of the precursor solutions and promote the adhesion of precursor and final oxides onto quartz and/or silicon substrates.

1.4.2.2 Determine the optimum conditions to synthesize pure and doped Fe ions ZnO thin films via a modified sol- gel method.

1.4.2.3 Characterize ZnO-based thin films systems from structural, morphological, compositional, optical and magnetic viewpoints.

1.4.2.4 Determine the effects of composition and grain size on the structural, optical and magnetic properties for ZnO and Fe doping at different atomic percentage (at %).

1.4.2.5 Determine the effects of the annealing temperature for pure and Fe-doped ZnO thin films at different Fe concentrations.

1.4.2.6 Determine the effects of the annealing temperature in nitrogen of pure and Fe-doped ZnO thin films at different dopant concentrations.

1.4.2.7 Discuss mechanisms involved with the functional properties attained in pure and doped systems.

1.5 CONTENTS OF THE THESIS

An overview of the content of this thesis is as follows. In the first chapter the justification, motivation and objectives of the research was presented. Chapter – 2, consists of a review of the background of ZnO overview, structure, defects, based DMS and the theoretical of magnetic behavior. Chapter – 3 is an updated review of description of the experimental procedures, synthesize as well as the characterization of the ZnO samples nanocrystalline powders and thin films. Chapter – 4 is dedicated to discussion and interpretation of our experimental results. The Chapter – 5 presents the general conclusion of this research. Finally, Chapter – 6 lists the reference consulted.

2 BACKGROUND

2.1 PURE AND DOPED ZnO SEMICONDUCTOR FILMS

2.1.1 An Overview of Zinc Oxide - ZnO is a wide band semiconductor (band gap energy of 3.37 eV) and a great band of exciton bond of 60 meV at room temperature. The difference of electronegativity between zinc and oxygen produces a high degree of ionicity in its bond, making it one of the most ionic compounds in this family. This causes a considerable repulsion among its cargo clouds, making more stable crystal structure to be a hexagonal form, Figure – 2, shows the wurzite structure of ZnO.

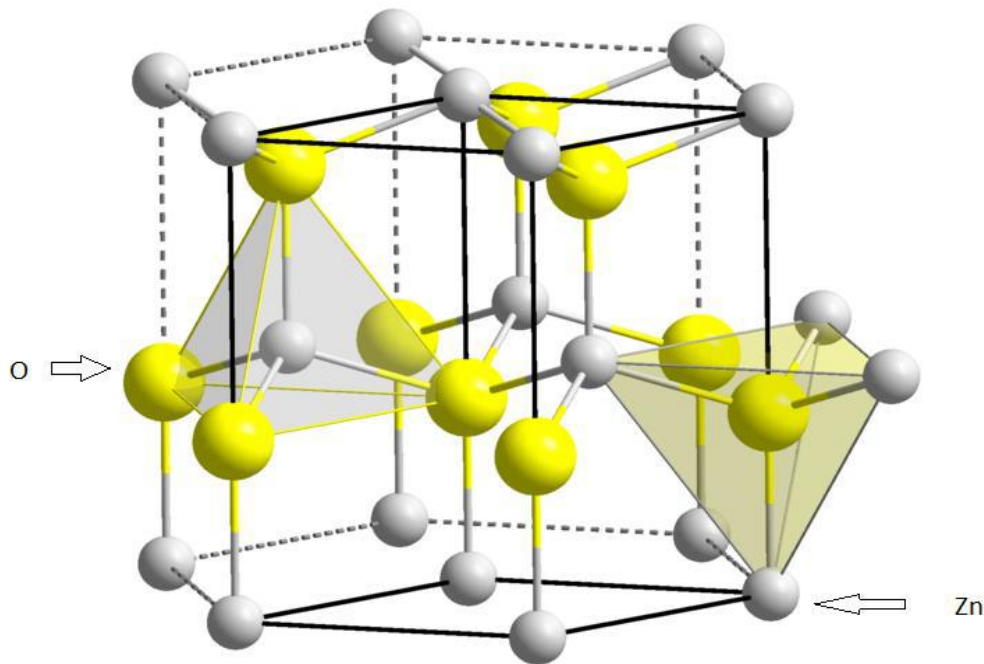


Figure – 2: Wurtzite Hexagonal Crystal Structure of Zinc Oxide [50].

Thus, each zinc atom is surrounded by a tetrahedron of 4 oxygen atoms and vice versa, forming in this way an alternate combination of planes of oxygen atoms and planes of zinc atoms,

which are along the c axis, with a displacement between them of $0.38c$, where c is the lattice parameter in the vertical direction. The values of the network parameters for said material, under normal conditions of pressure and temperature, are $a = 3.253 \text{ \AA}$ and $c = 5.213 \text{ \AA}$. The most important physical characteristic of ZnO is it exhibits gap direct energy of 3.35 eV , at room temperature. This large gap energy to room temperature, makes this metal oxide in an excellent candidate for applications like optoelectronic devices, acoustic transducers, varistors, and gas sensors, electrodes transparent, optical windows in solar panels, field-emitting devices, and transparent conductors. It is of special interest, its possible application in optoelectronic devices with emission in the range of short wavelengths.

2.1.1.1 ZnO Structural Properties [37, 91-92] - The ZnO wurtzite phase is thermodynamically stable at ambient conditions while the zinc blende ZnO is metastable and can be stabilized only by heteroepitaxial growth on cubic substrates. The Rocksalt (NaCl) structure might be achieved at relatively high pressures (15GPa) from wurtzite ZnO [92]. In the hexagonal wurtzite structures each anion (O^{2-}) is surrounded by four cations (Zn^{2+}) at the corners of a tetrahedron, and vice versa. A representative image of this arrangement of ions in wurtzite ZnO is displayed in Figure – 3. The tetrahedral coordination present in ZnO is usual in sp^3 covalent bonding; however, ZnO also possess a substantial ionic character that is inherent at the borderline between covalent and ionic semiconductor.

The experimental value for the cohesive energy per bond of the ZnO wurtzite phase is - 7.52 eV/atom [91-94]. The ZnO wurtzite structure belongs to the space group of C_{6v}^4 or $\text{P6}_3 \text{mc}$, it has a hexagonal unit cell with two lattice parameters “ a ” and “ c ”.

ZnO structure can be seen as two interpenetrating hexagonal close-packed (hcp) sub-lattices; each one made of one type of atom and displaced with respect to the other the amount of $u = 3/8 = 0.375$ in fractional coordinates along to the threefold c-axis (for an ideal crystal). The “u” parameter is determined by the length of the bond parallel to the c-axis in units of c. Therefore, each sub-lattice has four atoms per unit cell and every atom of one type (group-II) is surrounded by four other atoms of the other type (group VI), or vice versa in tetrahedral coordination.

In a real ZnO crystal, the wurtzite structure moves away from the ideal arrangement changing the c/a ratio (1.633 in the ideal case) or the u parameter. There is a strong correlation between the c/a ratio and the u parameter, when the c/a ratio decreases the u parameter increases in certain amount that the four tetrahedral distances are kept nearly constant under a distortion of the tetrahedral angles product of long-range polar interactions. Also, since the c/a ratio is related to the electronegativity of the lattice constituents, the component with highest electronegativity difference will present the greatest deviation from the ideal c/a ratio [37, 91].

The ZnO wurtzite structure is made of triangularly arranged alternating bi-atomic (Zn and O) close-packed (001) planes and the stacking sequence of the (001) plane is AaBbAaBb in the [001] direction. The stacking sequence is represented in Figure – 3(b).

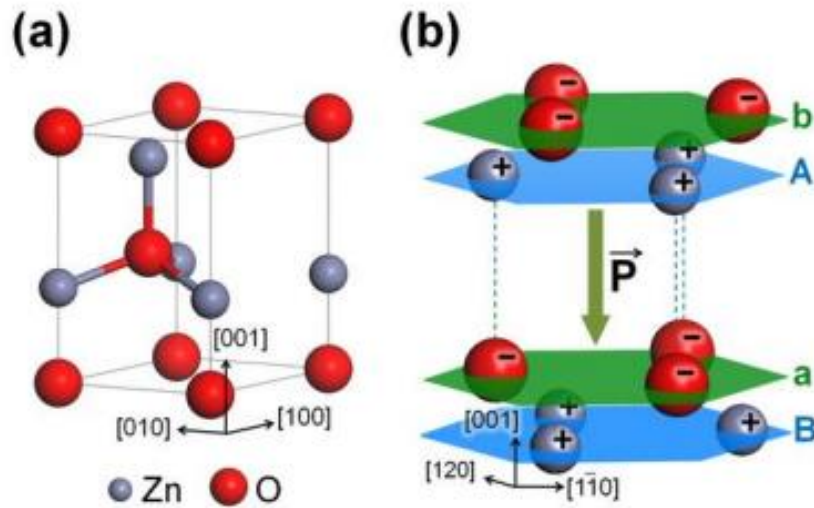


Figure – 3: *ZnO Atomic Wurtzite Structure [37].*

None of the ZnO crystalline structures presents inversion symmetry, for that reason the crystal displays a crystallographic polarity. This polarity indicates the direction of the bonds; it means for example, that the corresponding (001) basal planes in the wurtzite structure differs from the (001) planes. The convention is that the [001] axis goes from the face of the O plane to the Zn plane and is the positive z direction, see Figure – 3. Therefore, when the bonds are from cation Zn to anion O along the c direction we have the so called Zn polarity and vice versa, when the bonds goes from anion O to cation Zn along the c direction there is oxygen polarity. The crystallographic polarity is associated to several properties of the materials such as growth, etching, defect generation, malleability, spontaneous polarization and piezoelectricity [37].

2.1.1.2 ZnO Optical Properties - The photoluminescence spectrum of ZnO consists of mainly of two emission bands. One is in the Ultraviolet (UV) region and corresponds to the band near the edge of emission (near-band-edge) which is attributed to the excitonic states, the other band is in the visible region and it's because of the defects structural and impurities. Although several previous works have shown the emission in the UV of nanostructured ZnO materials, the detailed optical properties related to the band of energy and the presence of defects and impurities are still to be solved. Photoluminescence spectroscopy is generally adopted to investigate the processes of radiative recombination (emission), due to the excitons, defects, and levels of impurities in the semiconductors. The photoluminescence technique is a powerful tool for its high sensitivity and high spatial resolution [60].

Photoluminescent properties of ZnO are very sensitive to the crystal structure and defects. Next we relate some works that report the photoluminescent behavior of ZnO as n-type semiconductor with many defects intrinsic, such as interstitial zinc, vacancy oxygen, etc. Yang et al., successfully prepared ZnO nanowires and reported that such arrangements show laser emission properties with low threshold compared with the thin films of ZnO [60]. Dijten et al., prepared ZnO nanoparticles with different sizes average of particles and attributes the emission in the green to the transition of an electron from the driving band to a deep trap. It is worth mentioning that the improvement in the green emission of ZnO is also observed in silica aerogels nanopores and attributed to the increase of oxygen vacancies caused due to the lack of oxygen in the silica nanopores aerogels [60].

2.1.1.1.1 Photoluminescence Spectrum - It is the result of the absorption of a photon that generates an electron-hole pairs and produces emission of a photon of a different wavelength. When the incident photons are absorbed, electrons are promoted from the valence band to the conduction band as it was explained above. Once there the electrons and holes thermalize to the lowest energy state of their respective bands through phonon emission (they will relax very rapidly $\sim 10^{-13}$ s) before recombining across the fundamental band gap or the defect levels, trap levels, within the band gap and emitting photons to the corresponding energies. Figure – 4, shows a schematic representation of the photoluminescence of a direct and an indirect band gap semiconductor. In Figure – 5, there is a scheme of non-radiative transition of electron through trap levels within the band gap result of defects in the material.

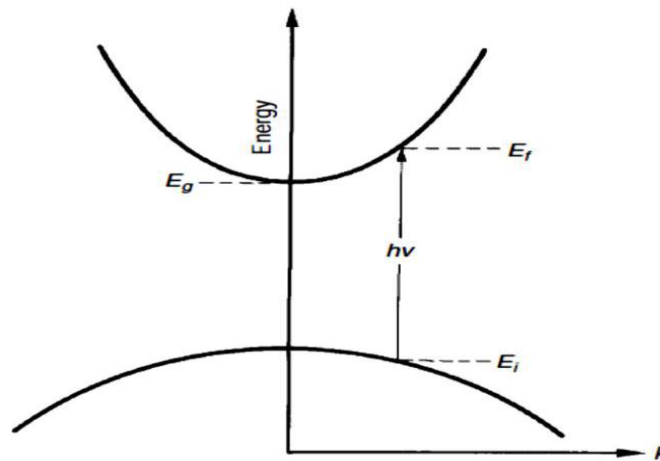


Figure – 4: The optical absorption due to a direct transition from a valence band state to a conduction band state [57].

If the electron-hole recombination produces photon emissions, the process is called radiative recombination. A recombination processes without photon emissions is called non-radiative recombination, in this process the energy is exchanged with the lattice as heat via phonon emissions through the defect states, trap states, in a direct band gap semiconductor.

Besides, when a radiative process does not involve an electromagnetic field, as in the photoluminescence experiments and light emitting diodes, this process is termed spontaneous emission. Photoluminescence is widely used in extracting important physical properties and materials characterization. Moreover light emission can be induced through an increase in temperature of the semiconductor (thermo-luminescence), electron irradiation (cathode-luminescence) and other high energy particle irradiation. These excitation methods are usually used to reveal the processes concerned with light emission, principally as a characterization tool.

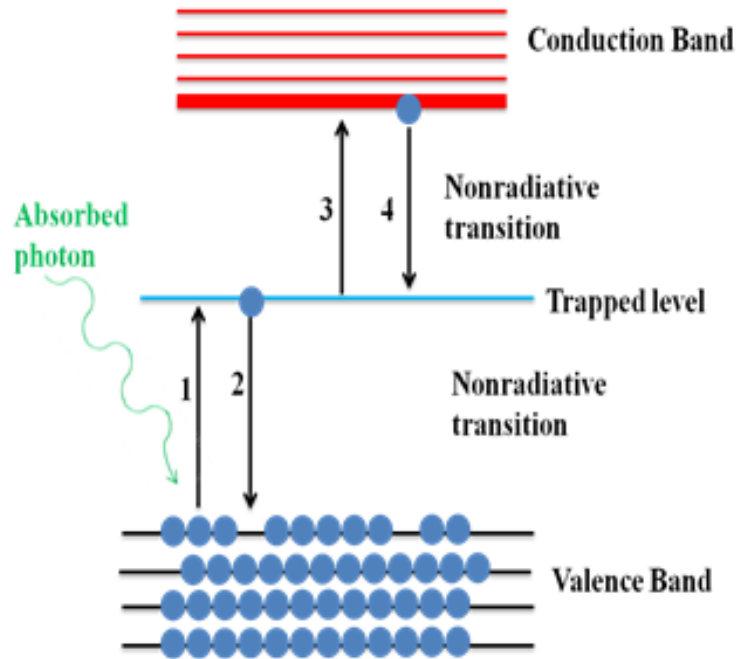


Figure – 5: *The schematic of non-radiative electron-hole recombination [37].*

A hole emission is produced when an electron jumps from the valence band (VB) to the trapped level, in step 1, then a hole capture, an electron moves from an occupied trap to the valence band, a hole disappears in step 2. An electron emission, an electron jumps from trapped level to the conduction band, in step 3. An electron capture occurs, when an electron moves from the conduction band to an unoccupied trap in step 4.

The light emission intensity can be written as:

$$R = B \sum_{k=0}^n p_{ul} n_u n_l$$

where n_u represents the density of electrons existing in upper energy states and n_l is the density of empty states with lower energy. p_{ul} is the probability of a transition from an upper state “ u ” to a lower state “ l ”. The fundamental difference from absorption is that at a given temperature the electrons are found near the minimum of the conduction band and light emission comes out only from these electrons.

Usually, reflectance and absorption spectra display structure for photon energies just below the band gap, where the crystal should be expected to be transparent. These extra-states below the conduction band exist in almost all semiconductors or ionic crystals and are not derived from band theory. They are originated by the absorption of a photon with the creation of a bound electron-hole pair. As an electron is bound to a proton to form a neutral hydrogen atom, an electron and a hole might be bound together by their attractive Coulomb interaction. The bound electron-hole pair is known as exciton.

An exciton can move all over the crystal and transport energy but it does not transport charge since it is electrically neutral. Figure – 6, represents the limiting types of excitons, Frenkel excitons (it is a tightly-bound exciton, and it will travel as a wave throughout the crystal, but the electron is always close to the hole) and Mott-Wannier excitons, is weakly bound, with an average electron-hole distance large in comparison with the lattice constant [57]. Besides, excitons can form complexes, such a bi-exciton from two excitons. All excitons are unstable respect to the ultimate recombination in which the electron falls into the hole.

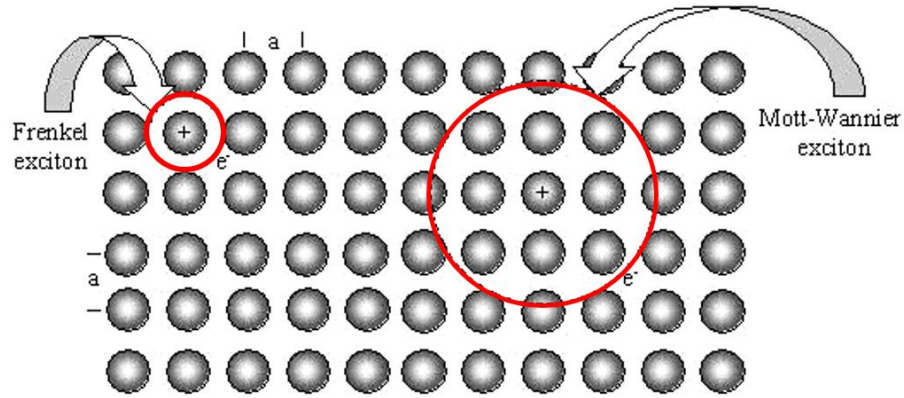


Figure – 6: Limiting types of excitons, © 2009 University of Cambridge [95].

As it was described in the previous section, a free electron and a free hole are created when the crystal absorbs a photon of energy greater than the band gap energy for a direct semiconductor. As a result the threshold for this process is $h\omega > E_g$. Aside from when an exciton is created, the energy is lowered with respect to this threshold by the binding energy of the exciton. The binding energy of exciton is usually in the range 1 meV to 1 eV, [58].

The formation of excitons via photon absorption is produced at any critical point, where $\nabla k \cdot \epsilon v = \nabla k \cdot \epsilon c$ is the group velocities of electrons and holes are equal and the particles may be bound by their Coulomb interaction. An electron with wave-vector \mathbf{k} has group velocity, if an electric field ϵ acts on the electron [49]. Figure – 7 and Figure – 8, indicates the transitions leading to the creation of excitons below the energy gaps. By analogy to a hydrogen atom, the binding energy of an exciton can be calculated as:

$$G_{ex} = -\frac{m_r^* e^4}{32\pi^2 \hbar^2 \epsilon^2} \cdot \frac{1}{n^2}$$

where, n is a quantum number which specifies the states and can take the values $n=1, 2, 3, \dots$, the e is the electric charge, ϵ is the dielectric constant of the semiconductor, $\pi = 3.14, \dots$, $\hbar = h/(2\pi) = 1.0546 \times 10^{-34} \text{ J}\cdot\text{s}$, and (m_r^*) is the reduced mass of an exciton.

The energy levels of the free exciton are displayed in Figure – 7. The limit situation of the $n \rightarrow \infty$, correspond to a state in the conduction band minimum. The lowest state energy can be calculated fixing $n = 1$:

$$E_{\text{ex}}(n=1) = E_g - |G_{\text{ex}}|$$

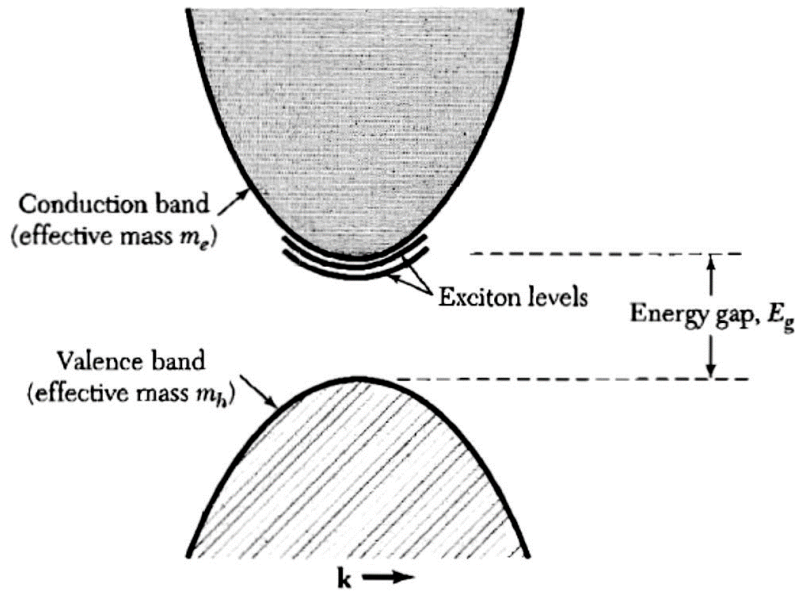


Figure – 7: Exciton levels in relation to the conduction band edge [49].

For a simple band structure with both conduction and valence band edges at $k = 0$. An exciton can have translational kinetic energy. Excitons are unstable with respect to radiative recombination in which the electron drops into the hole in the valence band, accompanied by the emission of a photon or phonons.

The optical transitions from the top of the valence band are shown by the arrows: the longest arrow corresponds to the energy gap. The binding energy of the exciton is E_{ex} , referred to a free electron and free hole. The lowest frequency absorption line of the crystal at absolute zero is not E_{ex} , but is $E_g - E_{ex}$. So, the Figure – 16 represents the effect of the exciton level on the optical absorption spectrum of a direct band gap semiconductor by photons with energy near the band gap. In this spectrum, shows the characteristic exciton peak and an estimation of the band gap.

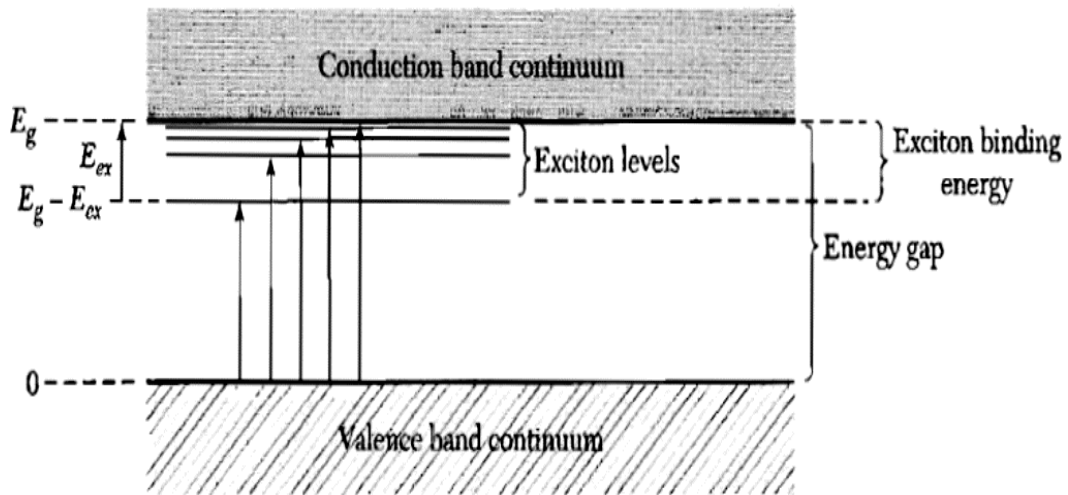


Figure – 8: Energy levels of an exciton created in a direct process [49].

2.1.2 ZnO Lattice Parameters – The most frequently used surface and direction for growth wurtzite ZnO are the primary polar plane (001) and associated direction [001], however there are many other secondary planes and direction in this crystal structure. The lattice parameters in a semiconductor material commonly depend on [92]:

1. Free-electron concentration acting via deformation potential of a conduction-band minimum occupied by these electrons. It has been reported that free charge is the dominant factor responsible for expanding the lattice proportional to the deformation potential of the conduction-band minimum and inversely proportional to the carrier density and bulk modulus.

2. The concentration of foreign atoms and defects and their difference of ionic radii with respect to the substituted matrix ion, like as; doping or point defects such as zinc antisites, oxygen vacancies, and extended defects, like threading dislocations, also increase the lattice constant, although in a lesser extent in the heteroepitaxial layers.

3. External strains such as, those induced by substrate.

4. Temperature.

The lattice constants for ZnO wurtzite structure at room temperature have been determined by Reeber, [91]. Therefore, the lattice parameter “a” mostly ranges from 3.2475 Å to 3.2501 Å and “c” ranges from 5.2042 Å to 5.2075 Å. The c/a ratio and the u parameter present a slightly wider variation, from 1.593 to 1.6035 and from 0.383 to 0.3856, respectively [91]. The deviation of those parameters from the ideal ZnO wurtzite crystal is attributed to the lattice stability and ionicity, [37, 91].

2.1.3 Structural Defects in ZnO – Wide band gap materials, like ZnO, experience

Difficulty in doping control due to native defects in the material structure. In ZnO, native defects in the crystal lattice can influence the structure, affecting the optical and electrical properties and device quality, producing a naturally n-type material, [1, and 99]. Figure – 2, the alignment yields four zinc (grey) cations surrounding each oxygen (yellow) anion. Furthermore, these donors in zinc oxide can be compensated by the incorporation acceptor dopants, preventing p-type conductivity. Structural defects can be dependent on the atmosphere in which the ZnO material is grown and a number of thermal treatment techniques post-synthesis. Characterizing the nature of defects in ZnO thin films will shed light on the material properties and possibilities for tuning.

2.1.3.1 *Oxygen Vacancies* are the most discussed defect in ZnO, as it was once believed

to be one of the main sources for natural n-typing, although density-functional theory calculates that oxygen vacancies (V_o) are too deep to contribute to n-type conductivity. Still, this defect is electrically and optically active, responsible for a green luminescence signal. These deep donors can be filled or manipulated in different annealing atmospheres, such as hydrogen, affecting the optical properties with reports of changing the color from red to transparent. Therefore, annealing a ZnO thin film in an O_2 atmosphere will reduce the number of charge carriers, decreasing the photoluminescence signal [98].

2.1.3.2 *Zinc Vacancies* can easily form as a deep acceptor in n-type ZnO. In oxygen rich atmospheres, a stronger photoluminescence signal is created at the 2.2eV peak, signifying a higher concentration of zinc vacancies. Hydrogen rich atmospheres also have an effect on these zinc vacancies. Due to hydrogen's donor-like nature, its incorporation into the structure will passivate the charge state of zinc vacancies. This in turn will increase the n-type conductivity. Evidence of

this is shown because the green luminescence is quenched when oxygen-rich ZnO is doped with hydrogen [100].

2.1.3.3 Zinc Interstitials bring two electrons above the conduction band minimum in order to stabilize its +2 charge state. These defects are not the source of n-type doping, as their formation energy is too low, but they can be source of p-type compensation [1, and 99]. Zinc interstitials (I_{Zn}) are thought to be a deep donor because they have low ionization energy, but it is still unclear if it is related to sublattice defects or zinc interstitial complex. Zinc interstitials have shown room temperature mobility, creating a complex with ambient nitrogen. This complex acts as a shallow donor and can increase the conductivity of ZnO, see Figure – 9 [102].

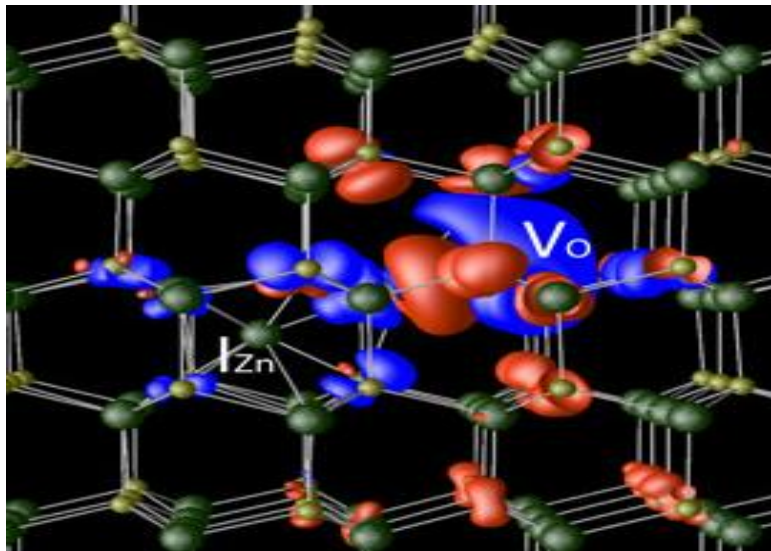


Figure – 9: *Structural Defects in Zinc Oxide. The figure shows a zinc oxide lattice with oxygen vacancy (V_o) and zinc interstitial, (I_{Zn}) defects. These defects cause a redistribution in positive charges (blue) and negative charges (red), ultimately resulting in an increase in n-type conductivity [102].*

2.2 ZnO-BASED DILUTED MAGNETIC SEMICONDUCTORS (DMS)

2.2.1 Dilute Magnetic Semiconductor (DMS)

The dilute magnetic semiconductors (DMS) are semiconductors doped with transition metal atoms. The primary aim of a DMS is compatibility with existing semiconductor structures and materials, in addition to their distinguished electronic, optical and magnetic properties. The electronic devices concept in semiconductors is based on controlling the electrons and holes in the semiconductor either their number or their speed. One could produce the well-known controlled devices such as the transistors which can be made to operate as switches or to operate as amplifier. The tuning of the electrical charge is accomplished by an electric field. Accordingly, this is a direct way to build controlled devices. A magnetic field can be used to control the motion of charged particles, but they must be in the state of motion according to Lorentz force, while the electric field can affect the charges even when they are at rest.

Regarding magnetic materials, they contain uncompensated electron spins and so they could be magnetized by the application of a magnetic field. Therefore, they are used to store data in magnetic domains. The hard disc data storage depends on permanent magnetization of the magnetic domains in magnetic materials. The writing is accomplished by electric current pulse and the reading is accomplished the induction effect.

With DMS it could be expected the viability to produce spintronic devices based on controlling the electron spins rather than electronic charges in the conventional electronic devices. Such devices are expected to have advantages over the conventional devices. Spintronic devices offer the possibility of enhanced functionality, higher speed, and reduced power consumption. This is because the spin is resulting from electron circulating on its own axes.

It can be considered as microscopic current loop that represents a quantum magnet and thereby readily storing a bit of information. Controlling the number and the orientation of the spin one can affect amplification switching and storing signals.

2.2.2 Dilute Magnetic Semiconductor Oxides – Semiconductor oxides can be doped

With transition metals. This gives rise to a material with the following advantages: i) a wide and adequate energy gap for applications with light of short wavelength, ii) high concentration of carrier's type n, iii) capacity to be grown at low temperatures and in a variety of substrates that include plastics or polymers; and iv) durability and low cost.

The general formula for a magnetically diluted semiconductor oxide (DMSO) has the form;



where, A is a non-magnetic cation, M is a magnetic cation and V represents a donor defect and n is usually 1 or 2.

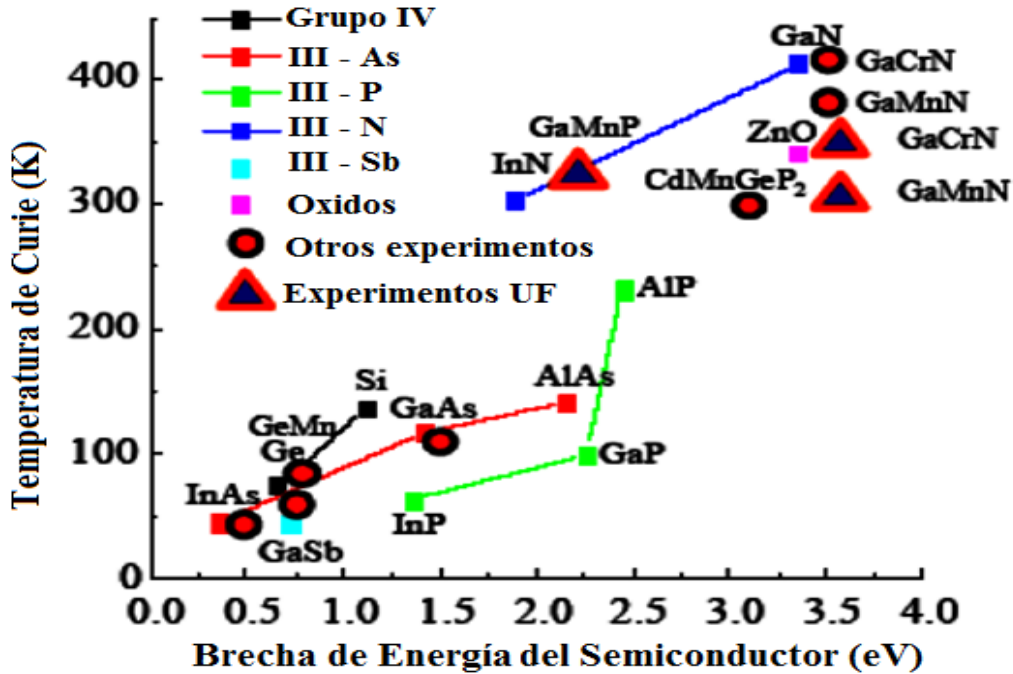


Figure - 10: Theoretical prediction of the variation of the temperature as a function of the energy gap of several semiconductors [37].

The most common properties associated with ferromagnetism in these materials are: i) a large part of the oxides are type n, ii) ferromagnetism occurs at concentrations that are below the level of percolation, the percolation refers to the slow movement of solvents through porous materials, which is related to the coupling of the nearest neighboring cations, iii) ferromagnets can be metallic, iv) for samples with the same nominal composition prepared by different methods of synthesis, the magnetic properties vary, and v) the average total moment per atom or cation of transition metal approaches the time of the spin at low concentrations, ie at low χ ; but this is not true as χ increases, probably caused by magnetic precipitation, see Figure – 10.

Theoretical results obtained by Dietl et al. based on ab initio calculations and local density approximation theory and predict the presence of ferromagnetism at room temperature in ZnO, with a p-type doping, performed with 5% Mn [16]. This theoretical work was the first step for the study of magnetically diluted semiconductor oxides (DMSO). In addition to ZnO, other semiconductor oxides can also be considered. Table – 1, shows the most relevant characteristics for oxides that can be converted into DMS. Generally, most semiconductor oxides, transparent to visible light, have a high energy gap and can be doped with n-type carriers [3].

Table – 1: Properties of different semiconductor oxides [5]

Compound	Structure crystalline	Conductivity (s cm ⁻¹)	Kind of carrier	Gap Energy (eV)	Maximum concentration of carrier(cm ⁻³)
CuAlO₂	Hexagonal	1	<i>p</i>	3.5	1.3 x 10 ¹⁷
CuGaO₂	Hexagonal	0.063	<i>p</i>	3.6	1.7 x 10 ¹⁸
SrCu₂O₂	*	0.05	<i>p</i>	3.3	6.0 x 10 ¹⁷
AgInO₂	Hexagonal	6	<i>n</i>	4.2	2.7 x 10 ¹⁹
ZnO	Hexagonal	20	<i>n</i>	3.2	1.0 x 10 ²¹
In₂O₃	Cubic	10 ⁴	<i>n</i>	3.75	1.0 x 10 ¹⁸
CdSnO₄	Orthogonal	10 ⁴	<i>n</i>	2.7	1.3 x 10 ¹⁷
CuAlO₂	Hexagonal	1	<i>p</i>	3.5	1.3 x 10 ¹⁷
SnO₂	Tetragonal	10 ⁴	<i>n</i>	3.6	8.0 x 10 ²⁰
TiO₂	Tetragonal	*	<i>n</i>	3.0	1.0 x 10 ¹⁹
CuO₂	Cubic	*	<i>p</i>	2.0	1.0 x 10 ¹⁷

* There are no reports in the literature

From these results, several studies based on ZnO and TiO₂, doped with transition metals such as Fe, Mn, Co, Cr [19-29], were reported. They were produced by different synthesis routes, mainly by Pulsed Laser deposition (PLD), Sol-Gel method, mechanical grinding and solid state reactions. Obtained results are controversial due to the uncertainty and lack of reproducibility in the observed paramagnetism or ferromagnetism and the origin of the magnetic properties of the material.

Also, there are studies where the same doped compounds have a non-ferromagnetic behavior with transition metals; while others have found ferromagnetic behavior, presenting T_c values from 30 K to 550 K, as shown in Figure – 11. In the first trials, where this behavior for TiO_2 doped with Co is shown, both in its anatase and rutile phases, several authors agree with the results mentioned above, but later studies conclude that it is possible that co-precipitation of Co is responsible of the ferromagnetic signal of this one. Comparing the two previous oxides, SnO_2 and In_2O_3 doped with Fe, V, Co and Ni [30-39] have few works where ferromagnetism is reported at room temperature; as in the previous oxides, there is controversy about the fact of finding magnetic ordering and that said presence is due to the presence of secondary phases of clusters of the metal or to the formation of oxides.

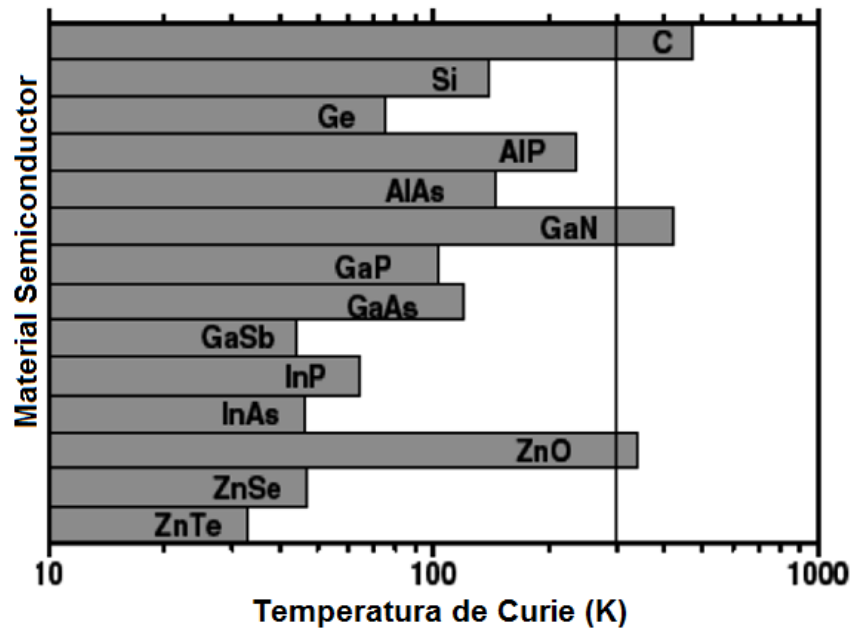


Figure - 11: Computational values of the Curie temperature for semiconductors [51].

The electrical properties of the co-doped semiconductor oxides have been reported and more recently the magnetic characterization of those materials revealed ferromagnetism at room temperature of SnO₂, In₂O₃ and TiO₂ [43-47].

At the experimental level, the results found in the literature for DMSO are not totally conclusive. Although it is noteworthy that ferromagnetism has been observed at room temperature, applying different techniques and synthesis routes, it is suggested that the results have an extrinsic affectation that depends on the presence of foreign agents or contaminants within the material under study. In addition, different theories and models have been proposed to describe the magnetic interaction and explain the origin of this behavior. Mainly regarding the exchange interactions and whether they are mediated by gaps or electrons or if the carriers are dislocated or localized. In conclusion, the origin of ferromagnetism in these systems is still not well defined nor understood.

2.3 Types of Magnetic Materials - Materials can be classified depending on the type of response they have based on the application of a magnetic field, which can be:

2.3.1 *Ferromagnetic:* A ferromagnetic body has a spontaneous magnetic moment even in the absence of the magnetic field; this magnetic moment suggests that electronic spins and magnetic moments are arranged in a regular manner as shown in Figure – 12. The order is not necessarily simple; all the provisions except the simple antiferromagnetic (and the helix if the directions of the spins are coplanar) have a spontaneous magnetic moment generally called saturation moment.

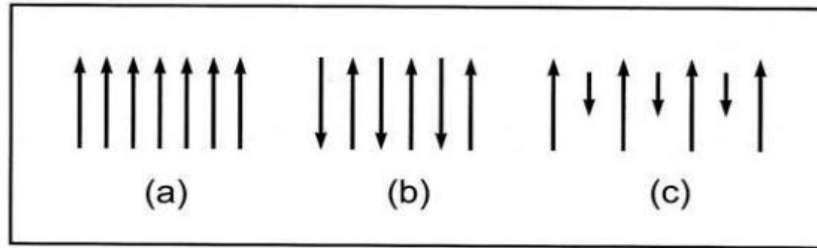


Figure – 12: Alignment of the magnetic dipoles for different types of magnetism: (a) ferromagnetism, (b) antiferromagnetic, (c) ferrimagnetism [52].

2.3.1.1 Ferrimagnetic: An antiparallel magnetic order is observed as in the previous case, whose difference lies in the magnetic moments coming from ions with different individual moments, which does not imply an absolute cancellation of the net magnetization.

2.3.1.2 Paramagnetic: Are those materials that have a small positive magnetic susceptibility by the action of a magnetic field are called paramagnetic. It is given by the individual alignment of the magnetic dipole moments of the atoms or molecules under the action of an applied magnetic field. Paramagnetic, produces magnetic susceptibilities in materials whose range is 10^{-6} up to 10^{-2} . This magnetic effect in the materials disappears when eliminating the applied magnetic field, since the thermal agitation randomly distributes the direction of the magnetic dipoles, an increase in the temperature decreases the paramagnetic effect.

2.3.1.3 Antiferromagnetic: A substance the spins are aligned antiparallel, obtaining a magnetic moment low or zero below the temperature of Néel.

2.3.1.4 Diamagnetic: An external magnetic field acting on the atoms of a material slightly unbalances the electrons of the orbitals by creating small magnetic dipoles in the atoms that oppose the applied field. This action produces a negative magnetic effect known as diamagnetism.

Diamagnetism produces a very weak magnetic susceptibility whose order is found in $\chi_m = 10^{-6}$ emu / mol.

2.3.2 Magnetic Susceptibility –

The magnetic behavior of a substance can be determined by measuring its magnetization in the presence of a magnetic field. The magnetic susceptibility per unit volume measures how susceptible a substance is to magnetization, which is defined as:

$$\chi_v = M / H_o$$

where, M is the magnetization of the sample and H_o is the applied field. Similarly, magnetic susceptibility implies the relationship between the magnetization produced in a sample by the presence of a variable magnetic field in the following way;

$$\chi_v = dM / dH_o$$

2.4 CHARACTERIZATION TECHNIQUES

The characterization techniques used in the samples to investigate the structural, optical and magnetic properties, was as follows in Figure – 13. The instruments we used, were located at the Nanotechnology Lab. (Dept. of Material Science and Engineering), the Earth X-ray Analysis Center (Dept. of Geology) both at the UPR-Mayaguez Campus. Other laboratories facilities used were in UPR- Ponce Campus for the PL measurements and The Material Characterization Center MCC at the UPR Molecular Center for SEM images.

The structure of produced films were determined by X-ray diffraction and estimated from the main diffraction peaks, according to Scherrer's equation, using a SIEMENS D-5000 unit with a Cu-K α radiation with a wavelength, $\lambda = 1.54$. The confirmation of bonding metal-oxygen was done by using a Schimadzu IRAffinity-1. The band for metal-oxygen causes a peak which is a combination of data with the wavelength and the location of that band, which is already categorized or is in a database where all the bands appear.

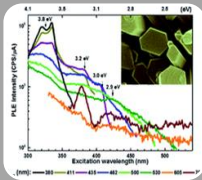
These wavelengths belong to a functional group, which is relate to a material. In the simple case that are the groups that have some metallic element, the band appears in 590 nm you can say that that is the metal oxygen bond. Average crystallite size was determinate by SEM/TEM images.

CHARACTERIZATION



Structural Properties

- X-ray Diffractometer (XRD)
- Scanning Electron Microscope (SEM)



Optical Properties

- Photoluminescence spectroscopy (PL)
- UV-Vis Spectroscopy



Magnetic Properties

- Vibrational Sample Magnetometer (VSM)

Figure – 13: Material characterization for structural, optical and magnetic properties.

SEM morphological analysis provides quantified information about chemistry, size, and amount of phases and particles present, morphological analysis provides information about the physical relationships of the size, crystallinity, and juxtaposition of the present phases [83]. Optical properties of films were measured using a UV-vis DU 800 spectrophotometer and a Fluoromax2 Photo-spectrometer, respectively. The excitation wavelength for photoluminescence measurements was 345 nm. For magnetic properties, the measurements were done at Room-temperature MH loops of doped ZnO thin films, and recorded in a Lake Shore 7410 VSM magnetometer [93].

2.4.1 FILMS THICKNESS DETERMINATION

2.4.1.1 Ellipsometry - Is a technique often used to measure the thickness of a thin film.

Generally speaking, the measurement is performed by polarizing an incident light beam, reflecting it off a smooth sample surface at a large oblique angle and then re-polarizing the light beam prior to its intensity measurement. Since the process of reflecting light off a smooth sample surface generally changes linearly polarized light into elliptically polarized light, the technique has been called ‘ellipsometry’, see Figure – 14.

The earliest ellipsometry measurements were used to determine the optical functions, refractive index n and extinction coefficient k , or equivalently, absorption coefficient α , for several materials. In the 1940s it was discovered that a single-wavelength nulling ellipsometry measurement could be used to determine the thickness of certain thin films very accurately [104]. Since that time, multiple wavelength ellipsometry has been used in spectral scanning and multichannel configurations; this additional data enables the simultaneous extraction of film thickness and material n , k spectra. Spectroscopic ellipsometry has thus become the standard methodology of characterizing thin films for a variety of industrial applications including semiconductors and photovoltaic devices.

The light source can be monochromatic, such as from a laser, or broadband, such as from a xenon or mercury arc lamp. The polarization state generator (PSG) and polarization state analyzer (PSA) are optical instruments that change the polarization state of a light beam passing through them and contain optical elements such as polarizers, retarders and photoelastic modulators. In most ellipsometry experiments, light from the PSG is reflected from the sample surface at a large angle of incidence ϕ . Spectroscopic ellipsometers use a white light source and a monochromator, either before the PSG or after the PSA, to select out specific wavelengths.

Some spectroscopic ellipsometers image the white light from the PSA onto a detector array, thereby allowing the whole spectrum to be collected simultaneously [104].

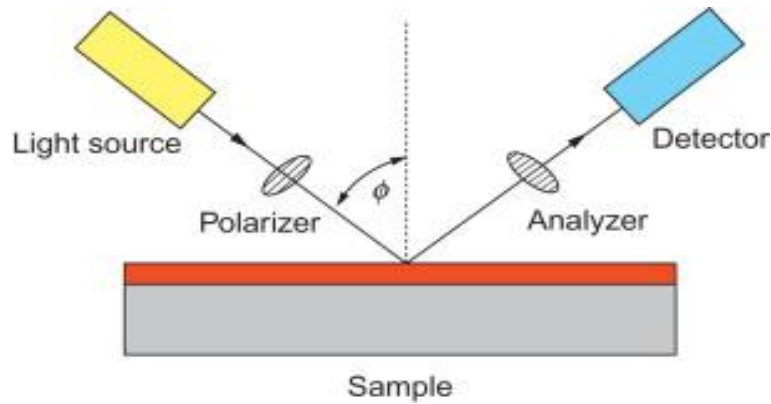


Figure – 14: Schematic Ellipsometry consists of five elements: (1) a light source, (2) a polarization state generator (PSG), (3) sample, (4) polarization state analyzer (PSA), and (5) light detector.

2.4.1.2 Profilometer - It is a measuring instrument used to measure a surface's profile, in order to quantify its roughness. Critical dimensions as step, curvature, flatness have been computed from the surface topography. While the historical notion of a profilometer was a device similar to a phonograph that measures a surface as the surface is moved relative to the contact profilometer's stylus, this notion is changing with the emergence of numerous non-contact profilometry techniques.

Non-scanning technologies are able to measure the surface topography within a single camera acquisition, XYZ scanning is no longer needed. As a consequence, dynamic changes of topography are measured in real-time. Contemporary profilometers are not only measuring static topography, but now also dynamic topography – such systems are described as time-resolved profilometers.

Contact profilometers have a diamond stylus is moved vertically in contact with a sample and then moved laterally across the sample for a specified distance and specified contact force. A profilometer can measure small surface variations in vertical stylus displacement as a function of position. A typical profilometer can measure small vertical features ranging in height from 10 nanometers to 1 millimeter. The height position of the diamond stylus generates an analog signal which is converted into a digital signal, stored, analyzed, and displayed. The radius of diamond stylus ranges from 20 nanometers to 50 μm , and the horizontal resolution is controlled by the scan speed and data signal sampling rate.

Advantages of contact profilometers include acceptance, surface independence, resolution, it is a direct technique with no modeling required. Most of the world's surface finish standards are written for contact profilometers. Contacting the surface is often an advantage in dirty environments where non-contact methods can end up measuring surface contaminants instead of the surface itself. Because the stylus is in contact with the surface, this method is not sensitive to surface reflectance or color. The stylus tip radius can be as small as 20 nanometers, significantly better than white-light optical profiling. Vertical resolution is typically sub-nanometer as well.

2.4.2 STRUCTURAL CHARACTERIZATION

2.4.2.1 X-ray diffraction (XRD) - In this technique, the energy of X-rays is transferred to an electron that is in the internal layers of the atom. The removed photoelectron carries a certain kinetic energy, E_k . This energy corresponds to the initial energy (E_i) of the X-ray photon (minus the barrier of potential that the electron must overcome for can leave the sample, commonly known as link energy ($h\nu$) and the work function (Φ).

$$E_k = h\nu - E_i - \Phi$$

The fact of having a wavelength of the order of Å, usual range for interatomic distances in the solids, turns X-rays into an excellent probe to study the crystalline structure of many materials.

In the interaction between an X-ray beam and a crystalline solid, in addition to the absorption process, has place a diffraction phenomenon. In the latter, meets Bragg's law

$$n\lambda = 2d\sin\theta$$

where, d is the interplanar distance, θ is the angle of Bragg, n , an integer and λ is the wavelength. This expression was formulated by Bragg imposing the condition of a special case of the general Laue equations. Laue, relate the incoming waves to the outgoing waves in the process of diffraction by a crystal lattice, reducing to Bragg's law. Therefore, from the measure of the angles diffraction information can be obtained on the planes formed by the different atoms that constitute the material in question. Most of the literature on XRD measurements in crystals present in ZnO films corresponds to reflection (002) together with the peak (004) which are present in the diffractogram of Figure – 15.

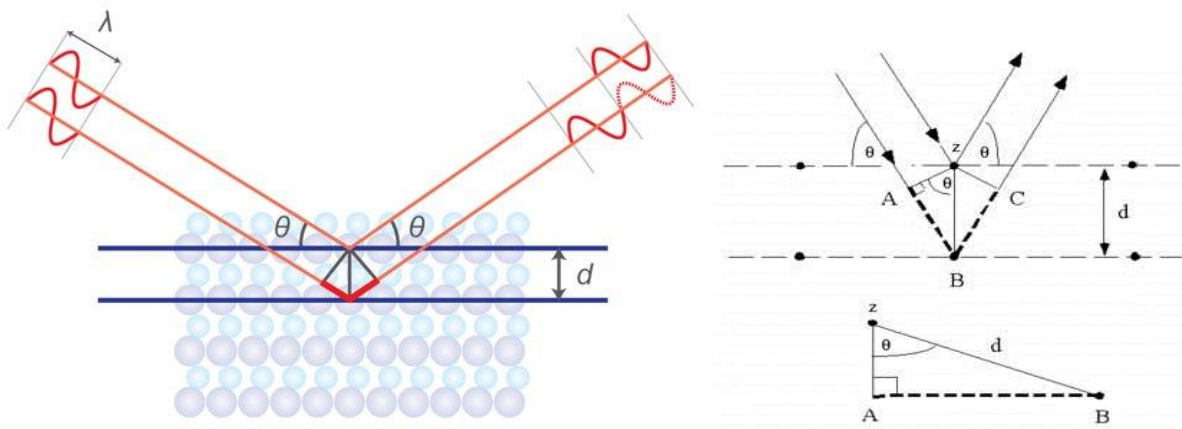


Figure – 15: Reflection of X-rays from different atomic planes, illustrating Bragg's law [34].

The scattering vector, is defined in the inset, different d-spacing. Plotting the angular positions and intensities of the resultant diffracted peaks results in XRD pattern, which is characteristic of the sample.

Where a mixture of different crystalline phases is present, the resulting diffractogram is formed by addition of the individual patterns. In the following section, we will describe the type of X-ray diffraction measurements used in this work.

2.4.3 OPTICAL CHARACTERIZATION – Within the characterization techniques, the study of optical absorption is a complement to the structure characterization for the analysis of ZnO crystals present in the films. For this, we have the optical transmittance and reflectance. The optical characterization techniques help us find the defects that are present in the crystals of ZnO and therefore in the films deposited from this material.

2.4.3.1 Ultraviolet-visible spectroscopy (UV-vis) – The UV-vis spectroscopy or ultraviolet visible spectrophotometry refers to absorption spectroscopy or reflectance spectroscopy in the ultraviolet-visible spectral region. The absorption or reflectance in the visible range directly affects the perceived color of the chemicals involved. In the UV-vis spectrum, an absorbance versus wavelength graph results and it measures transitions from the ground state to excited state, while photoluminescence deals with transitions from the excited state to the ground state.

An excitation spectrum is a graph of emission intensity versus excitation wavelength. An excitation spectrum looks very much like an absorption spectrum.

The greater the absorbance is at the excitation wavelength, the more molecules are promoted to the excited state and the more emission will be observed. By the UV-vis absorption spectrum, the wavelength at which the molecule absorbs energy most and is excited to a large extent can be obtained. Using such value as the excitation wavelength can thus provide a more intense emission at a red-shifted wavelength, which is usually within twice of the excitation wavelength.

2.4.3.2 Photoluminescence (PL) Measurements – Photoluminescence is the optical emission obtained by photon excitation, usually a laser, and is commonly observed with III-V semiconductor materials, see Figure – 16. This type of analysis allows non-destructive characterization of semiconductors (material composition, qualitative investigations, etc.).

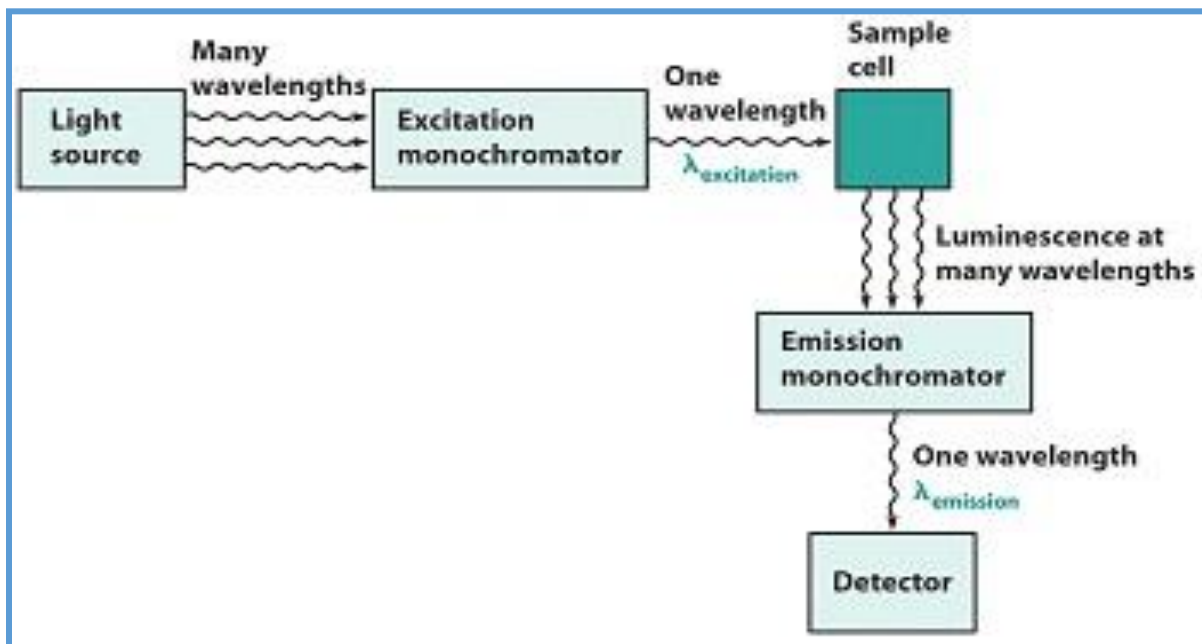


Figure – 16: Schematic representation of photoluminescence (PL) measurement [60].

The sample is irradiated at one wavelength and emission is observed over a range of wavelengths. The excitation monochromator selects the excitation wavelength and the emission monochromator selects one wavelength at a time to observe. A laser beam is focused on the sample which is located in the center of the sample compartment. If the energy of photons coming from the laser source is greater than the energy gap of the semiconductor, the sample emits photons. These are collected and analyzed with a dual flat field spectrograph. Two detectors are used, to follow investigations from 0.75 eV to up.

2.4.4 MAGNETIC CHARACTERIZATION

Magnetic materials are distinguished by their behavior in external magnetic fields. For ferromagnets, the (H) dependence is characterized by domain wall movement and magnetization rotation. According to the theory of Weiss a non-saturated ferromagnet contains a number of small regions called domains, in which the local magnetization is homogeneous and reaches the saturation value.

The direction of magnetization in different domains is not necessarily parallel. Two domains are separated by domain walls which are regions of approximated of 100 nm where the magnetization rotates continuously. They are classified by the angle of rotation (90° or 180°) and the mode of rotation, Bloch or Neel.

When applying an external magnetic field, domains with magnetization parallel to the field will grow at the cost of domains with energetically more unfavorable magnetization alignment. As a result domain walls move through the sample and the overall magnetization increases in field direction.

A second mechanism that increases the magnetization is magnetization rotation within the domains. Due to magnetic anisotropies, certain directions are easier to magnetize than others. The spontaneous magnetization lies preferably along one of these easy directions. If the applied external field is not parallel to such an easy direction, the magnetization rotates and aligns along the magnetic flux lines.

2.4.4.1 Vibrating Sample Magnetometer (VSM) – The VSM is a measurement technique which allows to determine the magnetic moment of a sample with very high precision. It is based on Faraday's law which states that an electromagnetic force is generated in a coil when there is a change in flux through the coil. In the measurement setup, a magnetic sample is moving in the proximity of two pickup coils as indicated in the following Figure – 17.

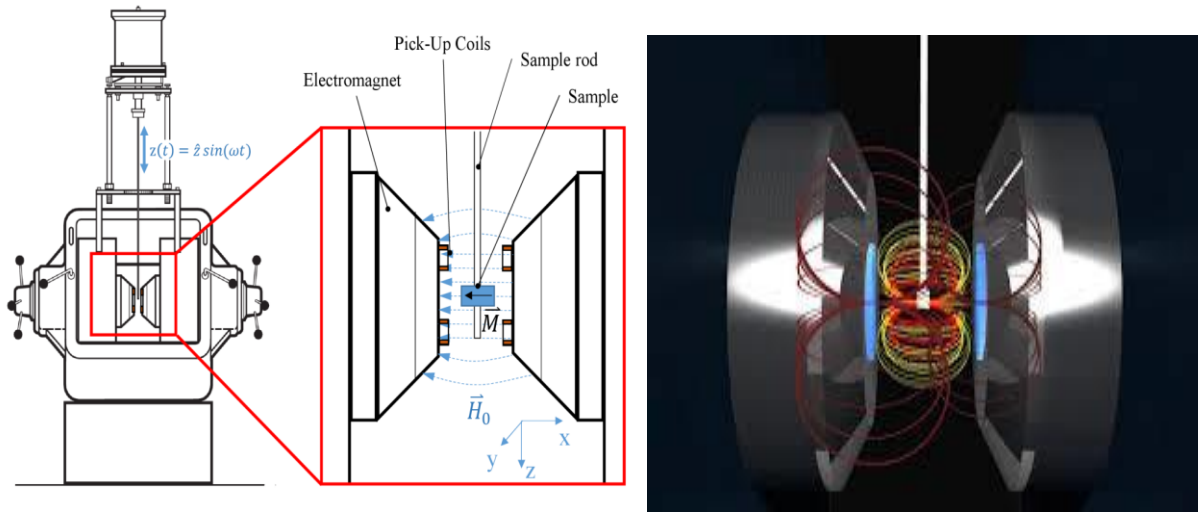


Figure – 17: Schematic representation of a VSM's coils [93].

The oscillator provides a sinusoidal signal that is translated by the transducer assembly into a vertical vibration. The sample which is fixed to the sample rod vibrates with a given frequency and amplitude.

It is centered between the two pole pieces of an electromagnet that generates a magnetic field H^{\rightarrow}_0 of high homogeneity. Stationary pickup coils are mounted on the poles of the electromagnet. Their symmetry center coincides with the magnetic center of the static sample. Hence, the change in magnetic flux originating from the vertical movement of the magnetized sample induces a voltage U_{ind} in the coils. H^{\rightarrow}_0 , being constant, has no effect on the voltage but is necessary only for magnetizing the sample. According to Faraday, the voltage in a single winding of the pickup coil can be written as,

$$U_{ind} = - (\partial\Phi / \partial t)$$

where, Φ is the magnetic flux. For n_c pickup coils with a flat surface A and n_w windings, The previous equation gives us;

$$U_{ind} = \sum n_c \sum n_w \int_A (\partial B / \partial t) dA$$

When we bring the sample into the homogeneous field H^{\rightarrow}_0 along the x axis, it will be magnetized along the direction of the field, resulting in a magnetic moment m^{\rightarrow} of the sample. Then, the sample will be moved periodically relative to the pickup coils. Here, we will consider a sinusoidal movement (z) of the sample perpendicular to the direction of H^{\rightarrow}_0 (along the z axis) with amplitude \hat{z} and frequency ω ,

$$z(t) = (\hat{z} / dt) = \hat{z} \cdot \omega \cdot \cos(\omega t)$$

A moving magnetic moment means a change in the magnetic flux density B^{\rightarrow} . For a point at a distance r^{\rightarrow} from the sample, it is;

$$\partial B^{\rightarrow} = \mu_0 \cdot \delta(t) \cdot \nabla\{H^{\rightarrow}(r^{\rightarrow})\}$$

With the field strength at distance r^{\rightarrow} from the sample being

$$H^{\rightarrow}(r^{\rightarrow}) = [1/(4\cdot\pi)] \cdot [(m^{\rightarrow}/r^3) - (3\cdot(m^{\rightarrow}\cdot r^{\rightarrow})r^{\rightarrow}/(r^5))]$$

and the magnetic moment being oriented along the x axis. Combining the previous equations, gives the induction voltage,

$$U_{ind}(t) = - \{(3z\dot{z})/(4\cdot\pi)\} \cdot m \cdot \mu_0 \cdot \cos(\omega t) \cdot \sum n_c \sum n_w \int_A dA^{\rightarrow} \cdot (1/r^3) \cdot G$$

where G contains information concerning the position and orientation of the pickup coils, summarized as the so called geometric factors g_i .

It is obvious that a change in time of magnetic flux originates from the vertical sample movement relative to the coils. The flux change detected by the coils is therefore proportional to a number of quantities: the frequency ω of the vibration and its amplitude $z\dot{z}$, the magnetic moment of the sample m^{\rightarrow} and the distance to the pickup coils y_0 . Furthermore, U_{ind} can be increased by increasing the number of windings n_w and the number of pickup coils n_c used in the setup.

Also, the geometry of the pickup coils influences the induction. The measurement setup is sensitive even to very low magnetic moments. Today's vibrating sample magnetometers are able to detect magnetic moments of down to the μemu range, which corresponds to approx. 10^{-9} g of iron. So, the vibrating sample magnetometers (VSMs) are used to characterize the DC magnetic properties of materials as a function of magnetic field, temperature, and time, with a broad temperature range capability up to 1,000 °C. These systems measure a wide range of sample types, making them ideal tools for the most demanding materials research applications as well as quality control of magnetic materials.

2.4.4.2 Hysteresis - With a VSM, the magnetic moment of a sample as a function of the external magnetic field strength can be measured. The figure below shows a typical result of such a measurement. The demagnetized sample ($M^{\vec{}} = 0^{\vec{}}$) is firstly magnetized to saturation in an applied field, see Figure – 18(a).

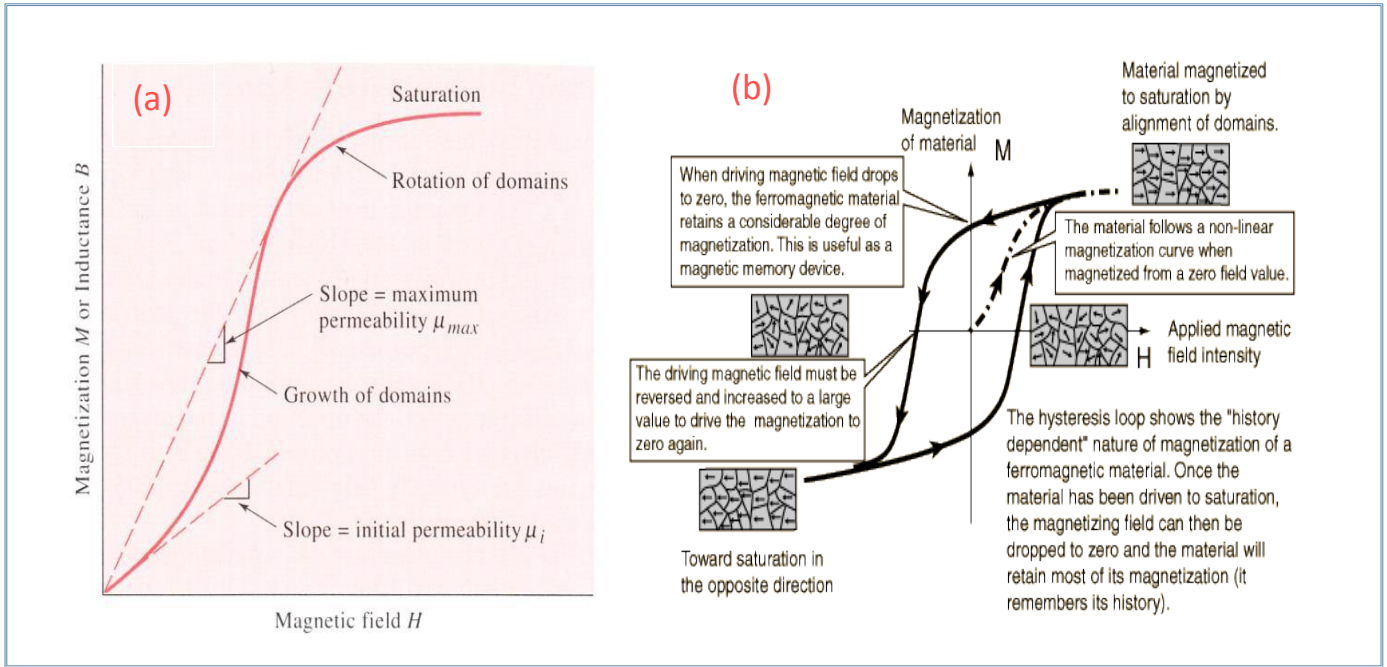


Figure – 18: a) Virgin curve, b) Hysteresis loop of a ferromagnetic material [84].

Two commonly used parameters are; initial permeability μ_i and the maximum permeability μ_{max} . It is defined in terms of a ratio of magnetic flux to field strength. Permeability is the slope of a line between the origin and a particular point on the curve in the upper inflection point before saturation for μ_{max} .

Increasing and decreasing the external field from the demagnetized state to positive saturation to negative saturation and back gives a ferromagnetic hysteresis loop, which is shown in Figure – 18(b). Here, the predominant, underlying mechanisms for each region are indicated.

The region of highest permeability is governed by domain wall motion whereas magnetization rotation occurs rather at higher magnetic fields. When the applied field is reduced to zero the remnant magnetization M_r remains. A magnetic field of opposite direction called coercivity field H_c is needed to macroscopically demagnetize the sample.

Thus, the hysteresis loop contains important information about the magnetic properties of the sample. Characteristic quantities include the saturation magnetization M_s , the remnant magnetization M_r , the coercivity field H_c , permeability μ and the dissipated energy that is necessary to magnetize the sample in the opposite direction. The dissipated energy can be calculated from the area that is included by the hysteresis loop.

3 EXPERIMENTAL

A modified sol-gel approach to synthesize well-crystallized pure and doped ZnO nanocrystalline thin films were developed. The attachment of ZnO into silicon substrate were optimized by selecting suitable organic agents to control the viscosity of precursor solutions and improve the attachment of the material to the substrate surface.

3.1 ZnO-Based Powder and Thin Films

3.1.1 Materials - Pure and Fe(II) and Fe(III) doped ZnO powders and films were synthesized by the sol-gel technique. Zinc Acetate Dehydrate [$\text{Zn}(\text{CH}_3\text{COO}) \cdot 2\text{H}_2\text{O}$, with a purity of 98%-101%], Iron (II) Chloride Tetrahydrate [$\text{FeCl}_2 \cdot 4\text{H}_2\text{O}$ at 98%] and Iron (III) Nitrate Nonahydrate [$\text{Fe}(\text{NO}_3)_3 \cdot 9\text{H}_2\text{O}$ at 98%-101%] were used as-received. Suitable amount of these reagents were used according to the dopant atomic fractions, which ranges between 0.5 at% and 7 at%. Ethanol, alcohol reagent, anhydrous denatured, [94-98%], and oxalic Monoethanolamine (MEA) were used as solvent and viscosity-controlling additive, respectively. The concentration of total metals (Zn dopant) were kept constant at 0.2 mol /L in all tests. Silicon Wafer substrates, provided by Addison Engineering, were ultrasonically cleaned in acetone, and washed out with ethanol and de-ionized water prior to spin-coating.

3.1.2 Synthesis of ZnO Powders - Powdered samples were synthesized by dissolving suitable amounts of Zn and Fe dopant salts in ethanol and heated for an hour for homogenization purpose. Subsequent, this homogenized solution, was dropped in a dish and heating at 150°C for twelve hours to assure the complete removal of the solvent.

The obtained solid precursor was then annealed in air or nitrogen atmosphere for 1 hour in the temperature range between 500°C and 700°C for each case. Annealed powders were submitted for characterization. A complete flowchart of the synthesis route is shown in Figure – 19.

3.1.3 Synthesis of Thin Films - Films samples were synthesized by dissolving suitable amounts of Zn and Fe dopant salts in ethanol and heated for an hour for homogenization purpose, getting a dissolved precursor properly. Subsequent, this homogenized solution, was dropped in a dish and heating at 150°C for twelve hours to assure the complete removal of the solvent. the solution was spin coated on the substrate surface at 2700 rpm for 12 seconds. The process forms a gelatinous network on the substrate surface. Subsequent removal of the solvent solidifies the gel, resulting in a solid film. After each coating cycle, produced films were pre-dried and dried for 5 minutes at two different temperatures (80°C and 120°C) to remove organic residuals.

These spin-coating/drying cycles were repeated for twenty times (20) to thicken the films. The spin-coated films were annealed in air or in controlled nitrogen atmosphere for one hour at temperatures for 500°C, 600°C and 700°C, respectively. The heating rate was controlled at 10 °C / min for each sample. A complete flowchart of the followings steps are shown in Figure – 19. Annealed films were submitted for structural, optical and magnetic characterization, see the Figure – 13.

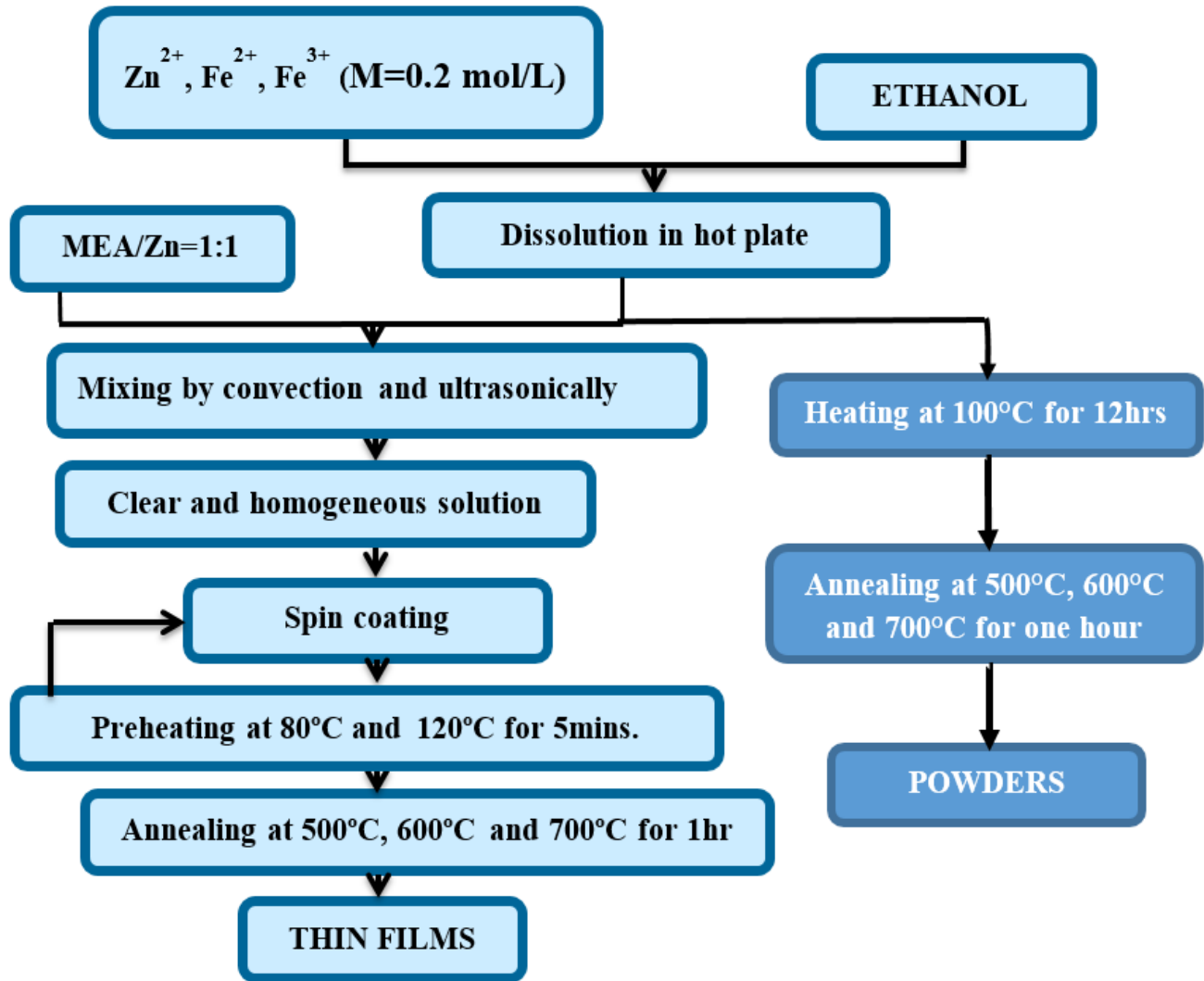


Figure – 19: Flow chart of the synthesis process of pure and Iron (II), Iron (III) doped ZnO for Powder and Thin Films by Sol-gel method.

4 RESULTS AND DISCUSSION

4.1 Zinc Oxide Nanoparticles

4.1.1 Structural Properties of Films of Pure ZnO Thin Films Annealed in Air

4.1.1.1 X-Ray Diffraction (XRD) of Pure ZnO Thin Films Annealed in Air

The X-ray diffraction (XRD) patterns shown in Figure – 20 and Figure – 21, correspond to pure ZnO deposited onto silicon substrate. Two peaks related to (002) planes, (100) and (101) planes were observed too, though with a very low intensity. So, there were a preferential growth along the ‘c’- axis, for thin films samples. For comparison purposes, the XRD patterns for ZnO nanoparticles produced by the similar sol-gel approach are also included (Figure – 20(b) and Fig. – 21(b)), for Pure ZnO annealed in air and controlled nitrogen atmosphere respectively. The average crystallite size was calculated using the Debye-Scherrer formula;

$$d = \frac{0.89 \cdot \lambda}{\beta \cdot \cos\theta}$$

where, 0.89 is Scherrer’s constant, λ is the wavelength of X-rays, θ is the Bragg diffraction angle, and β is the full width at half-maximum (FWHM) of the diffraction peak corresponding to plane (002). The smallest particle size of the sample was found to be 21 nm from different annealing conditions, see Table – 2. XRD measurements also confirm the synthesized thin films were free of impurities.

It is well known that the (002) orientation of ZnO wurtzite structure is generally observed, in ZnO films [85]. It can attributed to the fact that the surface free energy of (002) plane is the lowest in ZnO films, which results on the (002) preferred orientation the ZnO films [112].

Table – 2: Average crystallite size of Pure ZnO thin films in air and nitrogen atmosphere

	T=500°C	T=600°C	T=700°C		a (Å)	c (Å)	c/a
Pure ZnO @ Air	21 nm	45 nm	49 nm	Pure ZnO @ Air 700°C	3.257	5.203	1.5974
Pure ZnO @ Nitrogen Atmosphere	22 nm	41 nm	47 nm	Pure ZnO @ Nitrogen Atmosphere 500°C	3.245	5.203	1.6033

As Figure – 20 evidences, the increase in annealing temperature, in air or nitrogen atmosphere, enhanced the ZnO crystallinity. Similar situation occurred with the sample annealed in nitrogen atmosphere. However, as Figure – 21 shows, there is a remarked decrease in the (100) and (101) intensities when the annealing temperature was increased in presence of nitrogen. It can be attributed to the probable incorporation of N species into the ZnO host lattice [59].

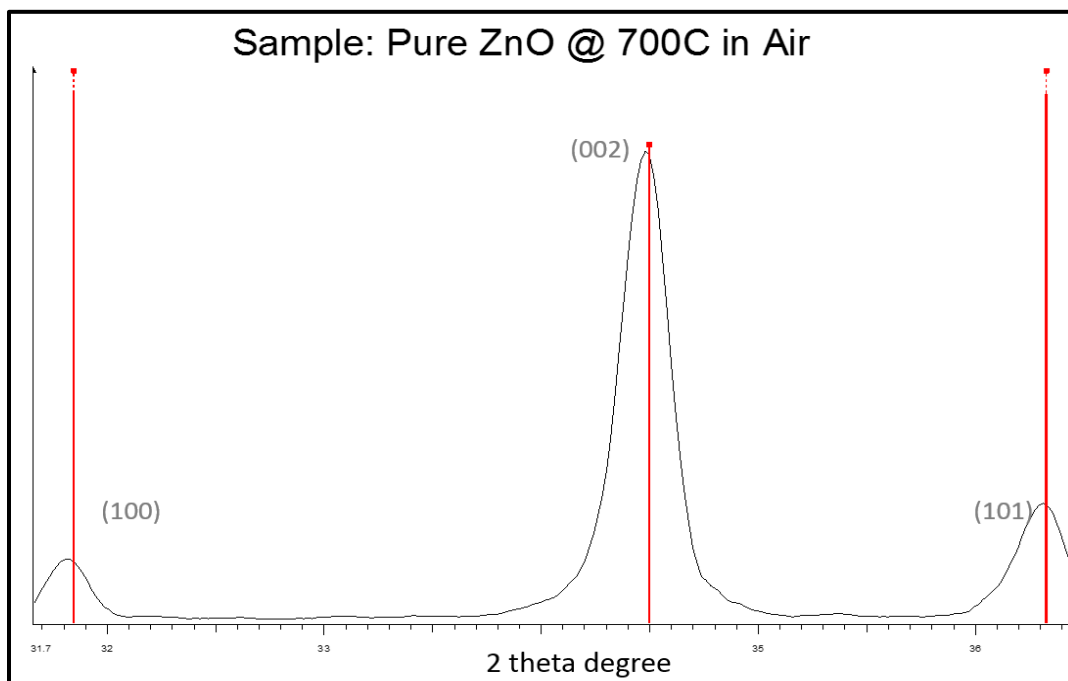
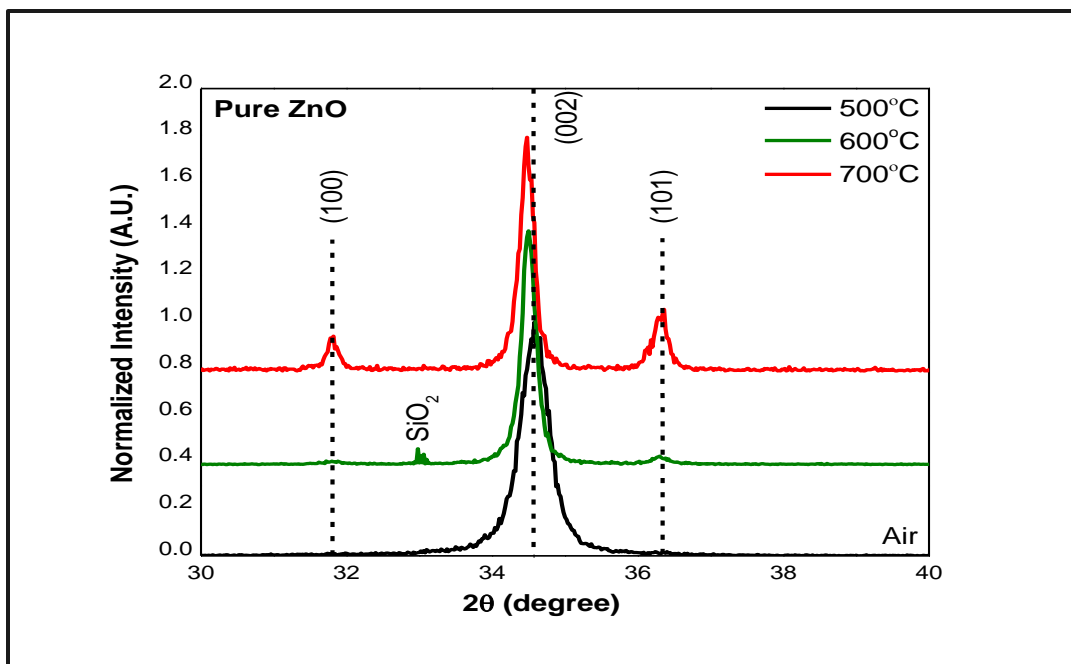


Figure – 20: (A) XRD for Pure ZnO annealed at different temperatures in air, (B) ZnO XRD Data JCPDS Card No.36-1451.

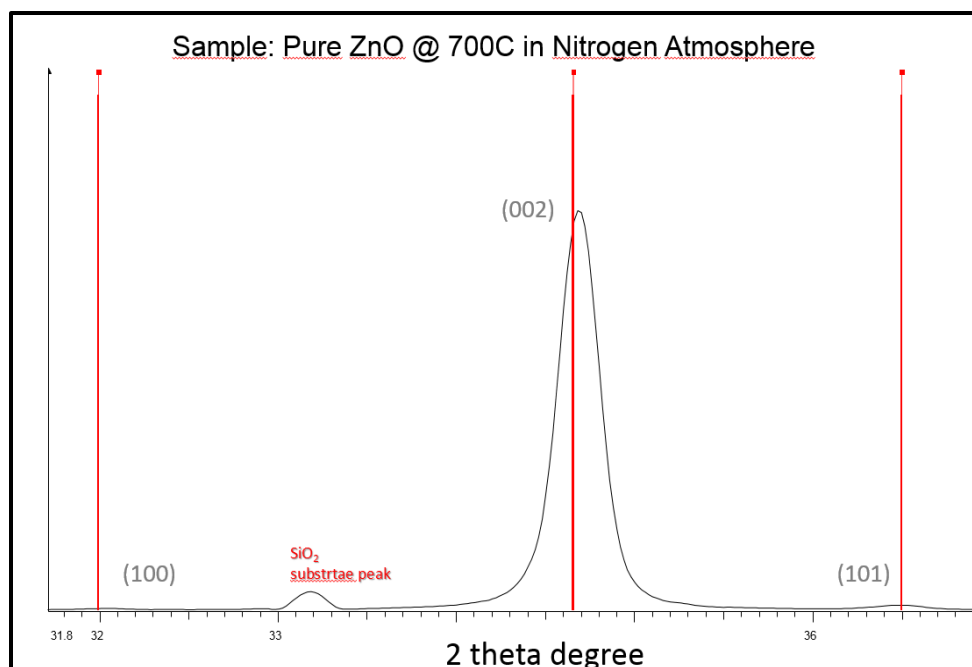
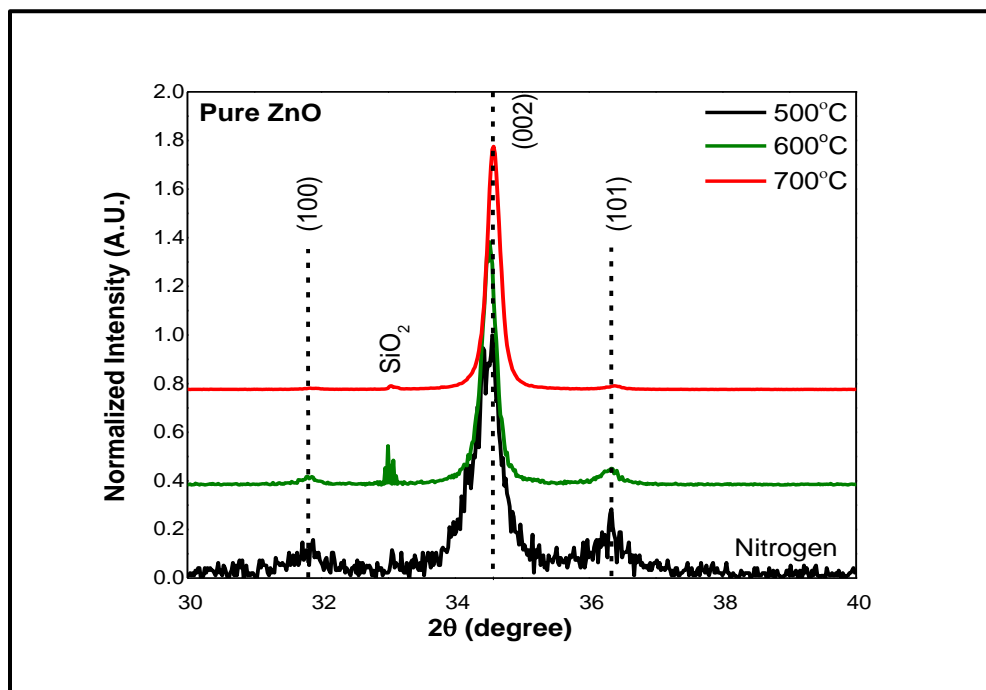


Figure – 21: (A) XRD for Pure ZnO annealed at different temperatures in controlled nitrogen atmosphere. (B) ZnO XRD Data JCPDS Card No.36-1451.

Figure – 21 also shows a shift in position of the (002) peak after increasing the annealing temperature, which can be attributed to better crystallinity with more relaxation caused by annealing. The shift of the (002) peak towards higher angles can also imply relaxation of the residual strain introduced in the films during the deposition process. The growth of epitaxial films depend on whether those films are coherent or not with their underlying substrate. Films that are coherent often tend to form ordered compounds at certain stoichiometric compositions, while films that are not often tend to separate into their pure-component "endpoint" phases. Coherency with an underlying substrate is thus a crucial determinant of the compositional integrity of films. If the layered material is coherent with its substrate, it will be mechanically strained, and its electronic and optoelectronic properties will be modified through strain-induced changes. Then, if the layer is not coherent with its substrate, then structural defects must be present, some of which degrade significantly the performance of semiconductor devices. If the bulk lattice parameters of the epitaxial layer and the substrate differ, then the epitaxial layer accommodates by developing in-plane strain.

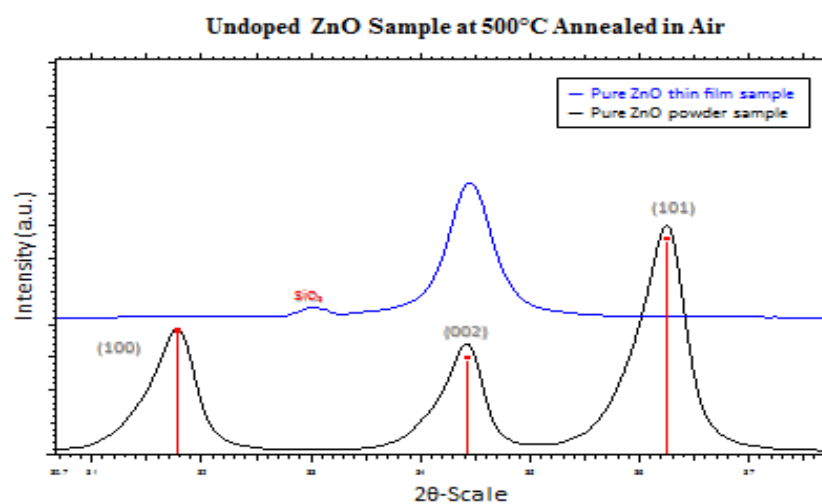


Figure – 22: XRD of Pure ZnO powder and thin films samples annealed in air at 500°C for one hour.

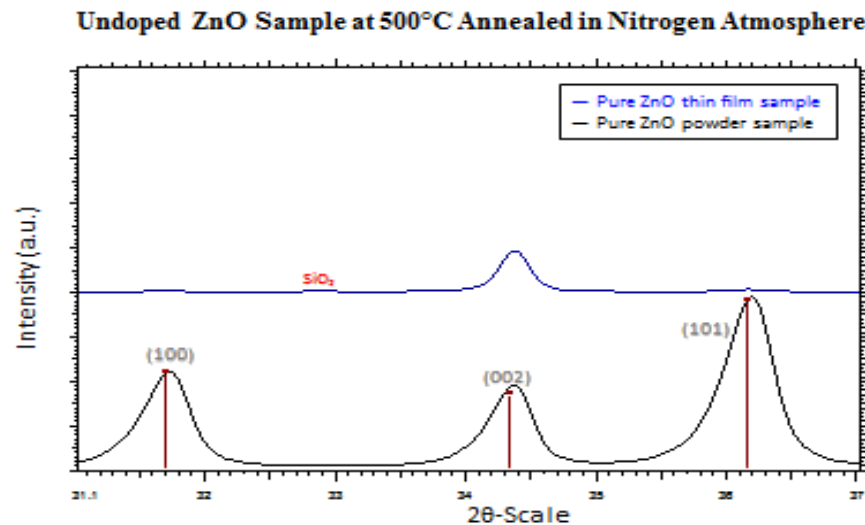


Figure – 23: XRD of Pure ZnO powder and thin films samples annealed in N₂ atmosphere at 500°C for one hour.

Undoped ZnO Sample at 700°C Annealed in Air

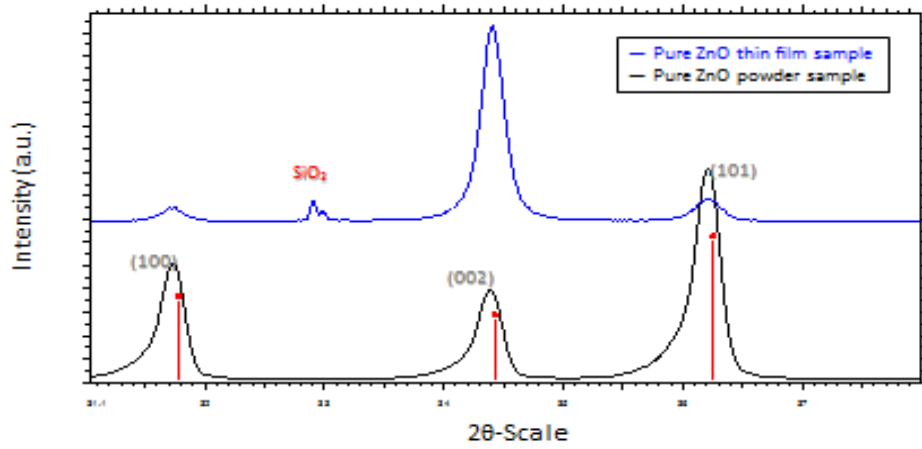


Figure – 24: XRD of Pure ZnO powder and thin films samples annealed in air at 700°C for one hour.

Undoped ZnO Sample at 700°C Annealed in Nitrogen Atmosphere

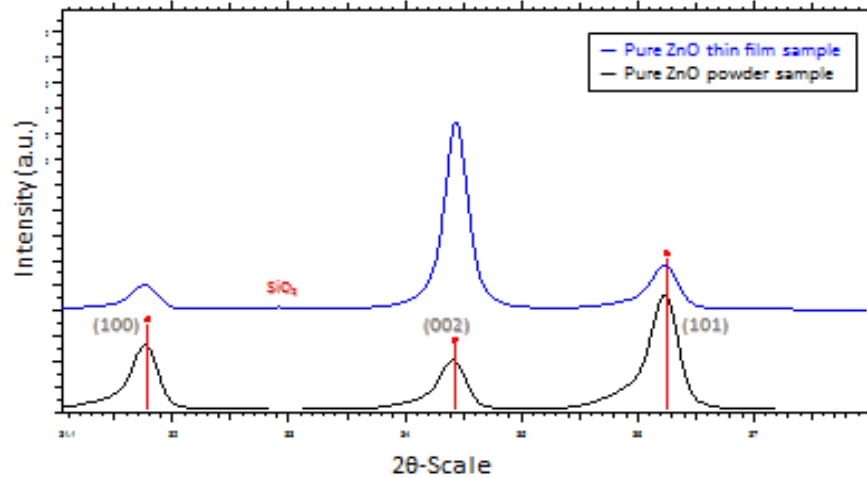


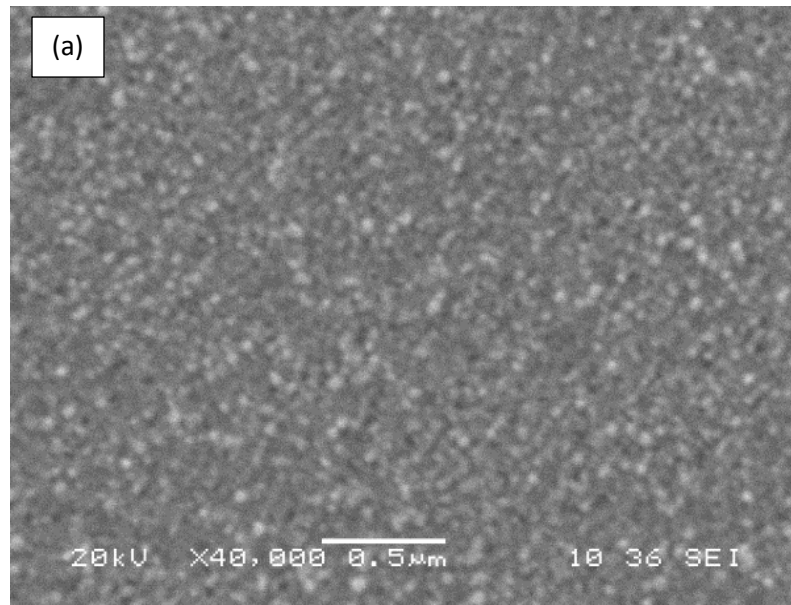
Figure – 25: XRD of Pure ZnO powder and thin films samples, annealed in N₂ atmosphere at 700°C for one hour.

4.1.1.2 ZnO THIN FILMS THICKNESS MEASUREMENTS

The thickness of the ZnO thin films were found to be uniform and approximately 300 nm \pm 17.13 nm. It was determined by using a profilometer (Tencor Alpha-Step D-500 Stylus Profiler), located at the UPRM – CID Clean Room, and corroborated by ellipsometry (Elcometer Positector 6000), hosted by the UPRM - Department of Mechanical Engineering.

4.1.1.3 SEM ANALYSIS OF PURE ZnO FILMS

SEM images of pure ZnO thin films deposited by sol-gel spin coating technique and annealed in air or nitrogen, are shown in Figure – 26. The micrographs are evidence of the nanocrystalline nature of the films and the uniform coverage of the whole surface of the substrate. The results from the SEM analyses evidence the formation of sub-micrometric secondary particles conformed by tiny crystallites visible below the 100 nm range.



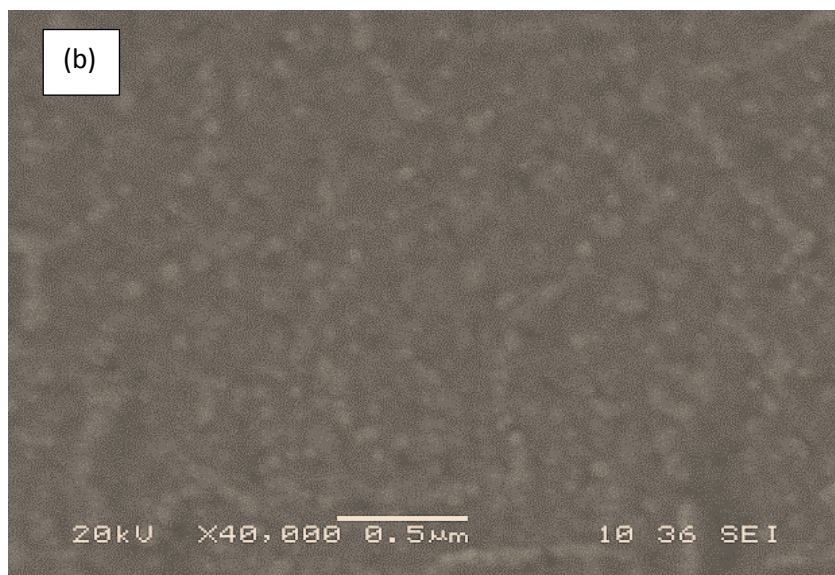


Figure – 26: SEM images showing the morphology of a pure ZnO film (a) annealed in air at 700°C (b) annealed in nitrogen-controlled atmosphere at 700°C.

4.1.1.4 TEM ANALYSIS OF PURE ZINC OXIDE POWDERS

The following images of powder samples were examined by the JEM-ARM200cF Transmission Electron Microscope (TEM) technique. The sizes of the nanoparticles are in agreement with the average crystallite size, between 10 nm to 20 nm, calculated using the corresponding XRD patterns; consequently, the formation of single crystals of ZnO can be suggested.

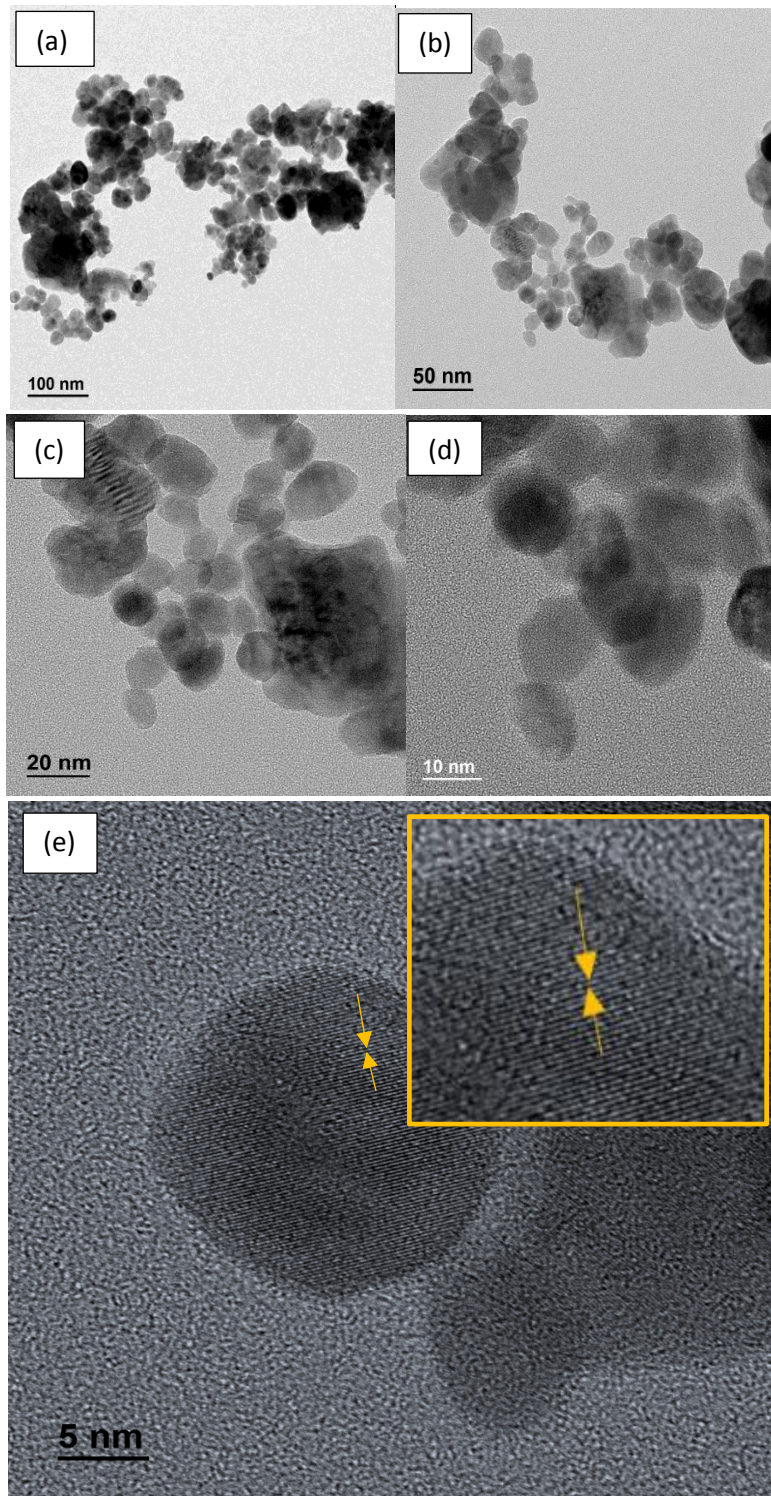


Figure – 27: TEM images showing the morphology of pure ZnO powder annealed at 700°C in air and different magnifications.

4.1.2 Optical Properties of Pure ZnO Thin Films

4.1.2.1 Photoluminescence (PL) Spectroscopy of Pure ZnO Thin Films

Figure – 28 and Figure – 29 show, room temperature Photoluminescence (PL) spectrum of ZnO thin films annealed between 500°C and 700°C in air and nitrogen-controlled atmosphere. The excitation wavelength was 345 nm. The spectra look very similar with the presence of two strong emission peaks; the PL emission peaks centered on 362 nm (500°C samples) and 388 nm (600°C and 700°C samples) are attributed to the exciton emission and transition of shallow donor levels near the conduction band to the valence band. This spectrum displays the characteristic UV emission of ZnO at 362 nm (3.42 eV) that is related to the recombination of the electron-holes pairs. The band at 541 nm corresponds to the green emission of ZnO that is related to the transition from the conduction band to deep levels in the band gap and is usually attributed to superficial defects and oxygen or Zinc vacancies [44, 61, and 62].

There are several bands other than the principal emission band in the UV region, they are centered on 388 nm and 541 nm, and were clearly identified in all samples within the visible region. This fact may suggest that the developed synthesis route creates defects in the structure usually associated with the luminescence in the visible region. These bands are related to the transition from shallow donor levels near the conduction band to the valence band. The second emission band in 388nm is attributed to Zn_i shallow donor levels, in which the electron relaxes from the CB and is captured by a trap state located within a band gap level to finally release photons. This violet emission at 388 nm, has been detected in small NPs and it was attributed to the presence of zinc interstitials (Zn) in the sample [64].

The very intense 388 nm-peak observed in our samples can enable the simple sol-gel synthesis route to be considered a simple process to produce ZnO exhibiting strong violet luminescence [37]. The band around 541 nm in the samples, are related to oxygen vacancies as reported in the literature [43]. The presence of the emission band at 378 nm is attributed to the presence of trap states [43]. These trap states are associated with structural defects, due to incorporation of Zn ions in interstitial sites of host lattice [43].

There is a direct relation, with the decreasing of the photoluminescence intensity as the temperature increases, for air annealing atmosphere samples. Because ZnO materials can concurrently possess visible and invisible light (UV) emission properties, after discounting the self-emitting UV, the visible light emission is considered to result from an internal thin film defect, which is caused by electrons colliding with the luminescent center under high voltages [113] Vanheusden et al., asserted that the green light's luminescent center, which is situated between 510 nm and 525 nm, is related to an O₂ vacancy [113].

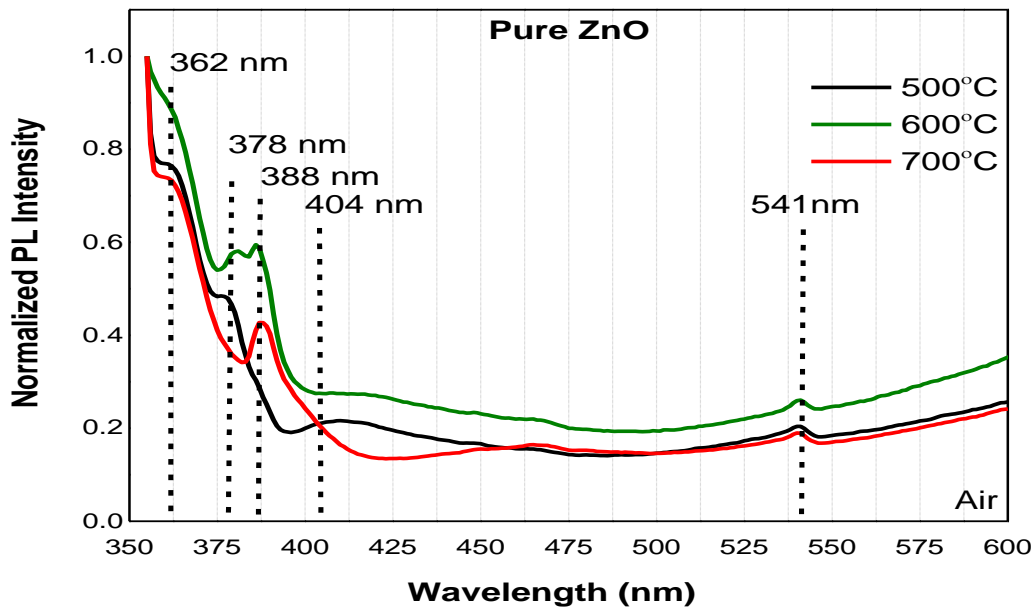


Figure – 28: Room temperature PL spectroscopy for Pure ZnO annealed at a range temperature between 500°C and 700°C in air.

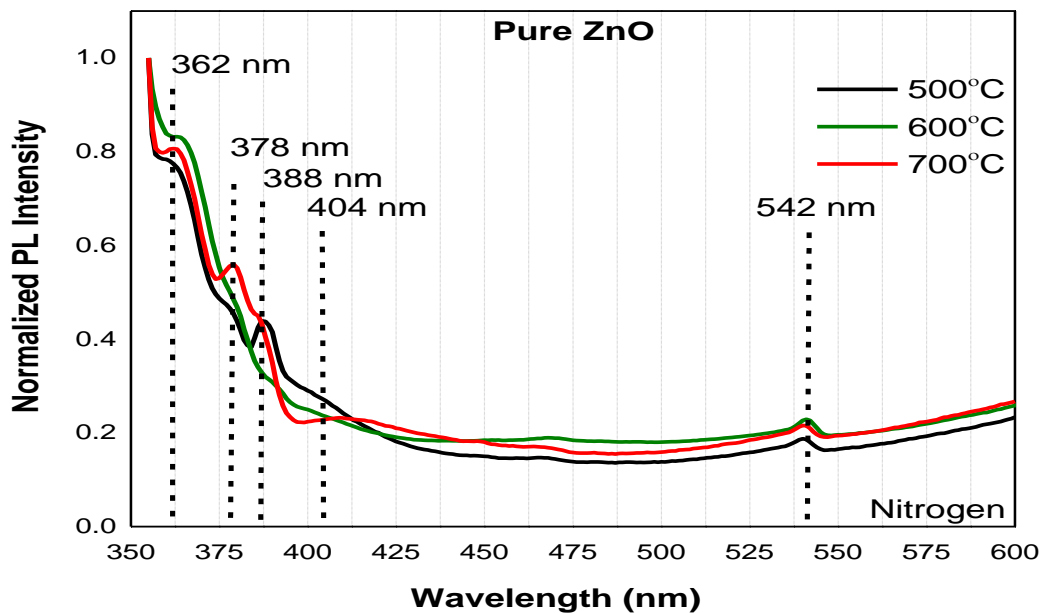


Figure – 29: Room temperature PL spectroscopy for Pure ZnO annealed at a range temperature between 500°C and 700°C in nitrogen atmosphere.

4.1.3 *Remarks:*

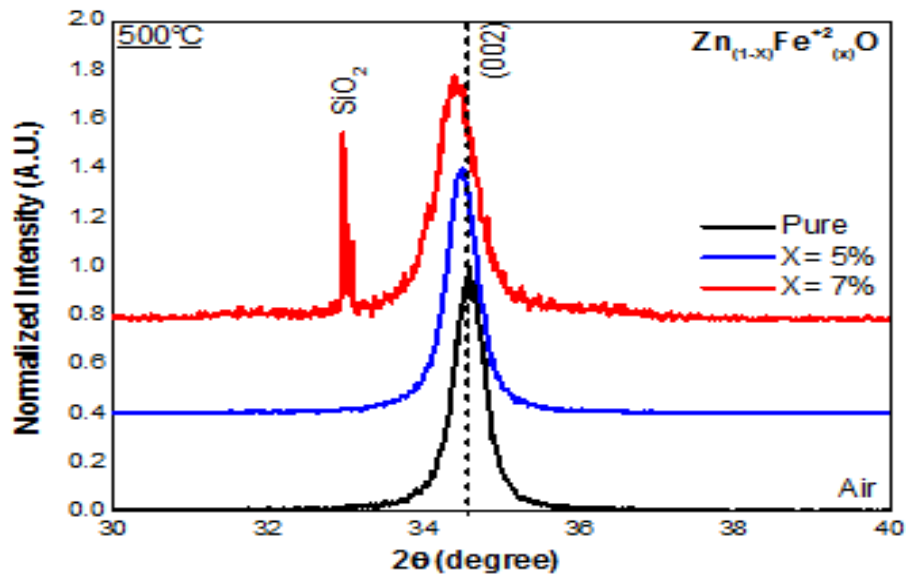
A sol-gel method at different annealing temperatures and atmospheres was developed to produce ZnO thin films, via a suitable control of the synthesis conditions. XRD reveals, that there is a small shift of the diffraction peaks to lower angles as the annealing temperature increases, because of an increase of the unit cell volume. XRD analyses also revealed the preferential growth along the c direction in all films. It can be attributed to coherency with an underlying substrate. As expected, the average crystallite size of ZnO thin films for both annealing environment conditions increased with increasing annealing temperature. PL spectra suggested the formation of defects. The most referred defects in ZnO are Zn interstitial (Zn_i), oxygen vacancies (V_O), Zn vacancies (V_{Zn}), Zn anti-sites (O_{Zn}), etc. However, although the exact origin of the visible emission is still not well understood, the green emission band is considered as the fundamental feature for ZnO. The increase in annealing temperature promotes an increase of defects, such as oxygen vacancies. The spectra exhibit the characteristic UV emission of pure ZnO at 362 nm that is related to the recombination of the electron-holes pairs. The band at 541 nm and 542 nm corresponds to the green emission of ZnO that is related to the transition from the conduction band to deep levels in the band gap and is usually attributed to superficial defects and oxygen or zinc vacancies.

4.2 Fe (II)-ZnO Thin Films Annealed in Air

4.2.1 Structural Properties of Films of Fe (II)-ZnO Thin Films Annealed in Air

4.2.1.1 X-Ray Diffraction (XRD) of Fe (II)-ZnO Thin Films Annealed in Air

The X-ray Diffraction (XRD) graphs in Figure – 30 and Figure – 31 show a Fe^{+2} doped ZnO on silicon substrate for different doping concentration and a range of temperature between 500°C and 700°C in air. Two peaks were observed, one in the ZnO (002) plane, and the other can be assigned to the substrate signal. There are no impurity peaks related to Fe_2O_3 or Fe_3O_4 in the XRD pattern. The absence of other isolated phases may suggest the possible incorporation of Fe^{2+}



within the ZnO host.

Figure – 30: XRD for Fe (II)-ZnO thin films annealed at 500°C in air for one hour.

The lattice parameter values exhibited a variation with the nominal of Fe^{2+} contents, x , with an appreciable effect in the position (002) with respect to pure ZnO.

From the XRD, it is clear that deposited films were in single phase, highly oriented along the c -axis, and maintain wurtzite crystalline symmetry. Figure – 30, also shows a shift of the (002) peak to lower 2θ values, suggesting the substitution of Zn ions by Fe ions in the wurtzite structure. The absence of impurity phases suggests the incorporation of Fe^{2+} (0.76 Å) in the Zn^{2+} (0.74 Å) sites. The average crystallite sizes calculated by Scherrer's equation are presented in Table – 3. In general, we observed a decreasing particle size with increasing dopant concentration. The distortion of the ZnO host lattice by incorporation of Fe dopants could have caused the instability of the structure that would be reflected in the nucleation and growth rate of the ZnO grains in the film.

Figure – 30, demonstrates a detail of the XRD patterns for the pure and Fe^{2+} -doped ZnO based thin films. A systematic shift of the peaks towards lower values of 2θ while increasing dopant concentration (at.%), suggest the actual incorporation of the Fe^{2+} ions into the ZnO lattice host. This shift could be explained in terms of the distortion, by expansion of the lattice due to the substitution of ions with different ionic radii. The corresponding lattice parameters “ a ” and “ c ” showed an interesting trend with the dopant concentration, ‘ x ’, as observed in Figure – 30. The lattice parameter “ a ” decreased while “ c ” increased with the nominal Fe^{2+} contents, x , systematically, suggesting an elongation of the hexagonal lattice of ZnO in the z -direction while reducing the area in the xy -plane as a result of the actual substitution of Zn^{2+} ions by Fe^{2+} ions. The calculated lattice parameters are in agreement with the standard values $a = 3.249\text{Å}$ and $c = 5.207\text{Å}$.

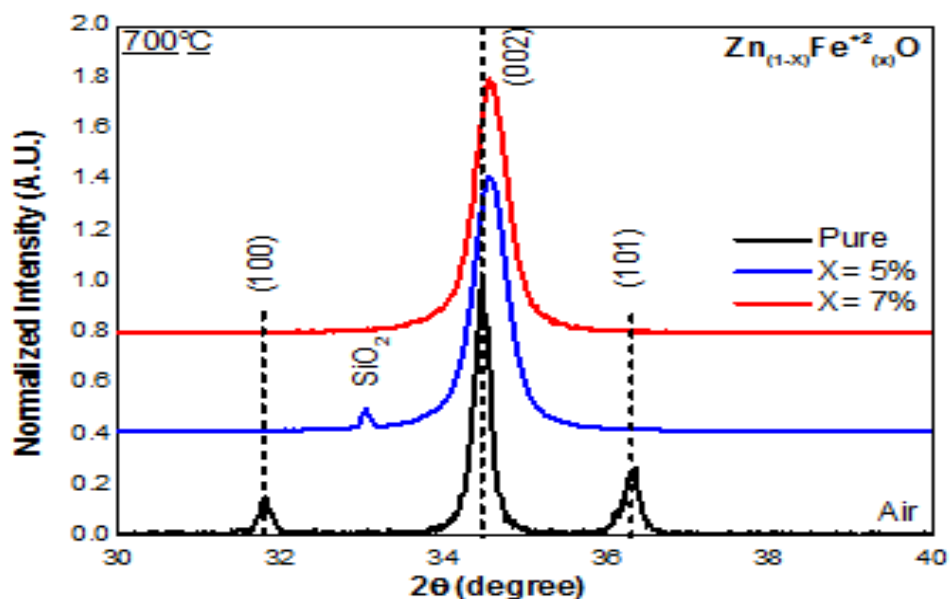


Figure – 31: XRD for Fe (II)-ZnO thin films annealed at 700°C in air for one hour.

Figure – 31, corresponds to the Fe-ZnO films annealed at 700°C and evidences a shift of the XRD peak to higher 2θ values when the dopant concentration was increased. A possible explanation is that as the annealing increases, the Fe^{+2} ions were oxidized to Fe^{+3} , causing a contraction in the unitary cell, contrasting the previous Figure – 30 at 500°C. Alver et al., also observed similar highly Fe-doped ZnO thin films prepared by ultrasonic spray pyrolysis method [71]. This variation shows the impact of doping concentration on the surface texture of the films. The intensities of various diffraction peaks are different, which indicates that the growth of ZnO

in various planes is different and anisotropic. A similar increase of peak intensity with Fe-doping was observed by Rambu et al. [70].

The calculated lattice parameters are in agreement with the standard values, $a = 3.257\text{\AA}$ and $c = 5.220\text{\AA}$, with a lattice parameter of $1.5974 \approx 1.6$. The lattice constants mostly range from 3.2475\AA to 3.2501\AA for the a-parameter and from 5.2042\AA to 5.2075\AA for the c-parameter. The data produced in earlier investigations, reviewed by Reeber are also consistent with the values given in Table – 3 [30]. The c/a ratio vary in a slightly wider range, from 1.593 to 1.6035 and 0.383 to 0.3856 [76].

As can be seen in Table – 3, the incorporation of the Fe species into the ZnO host lattice caused changes in the average crystallite size, as is also suggested by the noticeable widening in the diffraction peaks with respect to the pure material.

Table – 3: Average crystallite size of Fe (II)-ZnO thin films annealed in air

$X = \text{Fe}^{+2}$ at%	T=500°C	T=700°C	a (Å)	c (Å)	c/a
0	21 nm	49 nm	3.257	5.203	1.5974
5	20 nm	19 nm	3.269	5.220	1.5968
7	16 nm	20 nm	3.257	5.220	1.6027

The data in Figure – 30 shows the change in the lattice parameters with the dopant concentrations. The increase of the lattice parameters in Fe-ZnO structure with doping ($a = 3.257\text{\AA}$ to 3.269\AA and from $c=5.203\text{\AA}$ to 5.220\AA) may be indicative of the expansion of the unit cell due to the incorporation of large Fe^{+2} (0.76\AA) ions, substituting the smaller Zn (0.74\AA) ions.

4.2.1.2 SEM Analysis of Fe (II)-ZnO Annealed at 700C in Air

The ZnO particles morphology were observed using SEM as shown in Figure – 32. The results from SEM analyses, evidenced the formation of nanometric particles range. The ZnO particles exhibit a nanometric size and a heterogeneous particle dispersion.

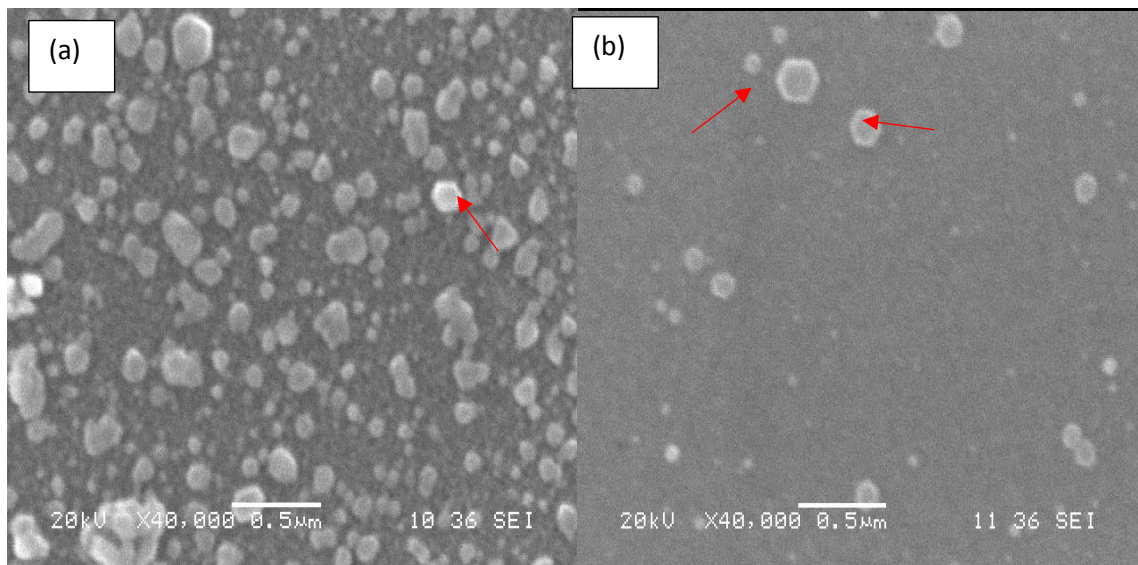


Figure – 32: SEM images of Fe (II)-ZnO annealed at 700C in air; (a) 5% dopant concentration and (b) 7% dopant concentration.

The SEM images of lightly doped ZnO films showed a rough surface topography with tiny grains were unevenly distributed with coarseness and agglomeration of grains were occurred due to the clustering of initial nuclei that led to form a compact film surface. However, with increase of Fe-doping concentration, the grains were distributed more homogeneously over the smooth background. Some complications during the film formation and spin coating could have induced the formation of these larger grains onto the surface of the films.

4.2.2 Optical Properties of Films of Fe (II)-ZnO Thin Films Annealed in Air

4.2.2.1 Photoluminescence (PL) Spectroscopy of Fe (II)-ZnO Thin Films Annealed in Air

The PL spectra at room temperature of Fe²⁺ doped ZnO thin films were obtained using an excitation wavelength of 345 nm and are shown in Figure – 33 and Figure – 34. The spectrum of pure ZnO thin films exhibit UV emission at 360 nm (3.42 eV) and green emission at 540 nm. The PL peak at 360 nm corresponds to the main emission peak of ZnO and is associated with the exciton recombination (i.e. the electron returns from CB to VB occupying the hole that left under the excitation) [37, 57, and 58].

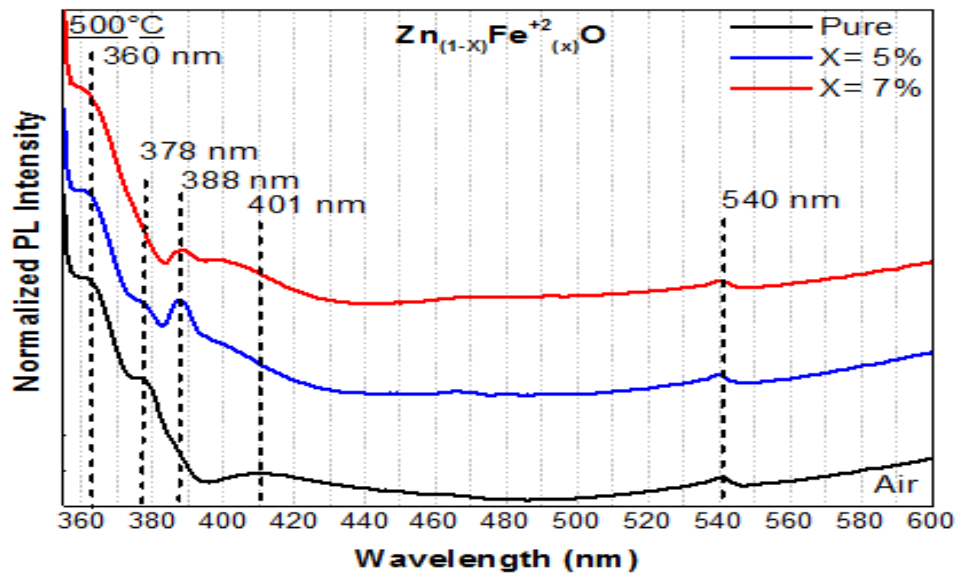


Figure – 33: Room temperature PL spectroscopy for Fe (II)-ZnO annealed at 500°C in air, with dopant concentration of x= 0, 5% and 7%.

The second emission is attributed to ZnO shallow donor levels, in which the electron relaxes from the CB and is captured by a trap state located within a band gap level to finally release photons [57-58]. The green emission of ZnO at 540 nm is related to superficial defects and oxygen or Zinc vacancies [37]. Violet emissions have been detected in small ZnO thin films and were assigned to existence of zinc interstitials (Zn_i) [76]. The main emission peak for the Fe-doped ZnO was centered on 388 nm.

Kramers–Anderson superexchange is the strong (usually) antiferromagnetic coupling between two next-to-nearest neighbor cations through a non-magnetic anion. In this way, it differs from direct exchange in which there is coupling between nearest neighbor cations not involving an intermediary anion. Superexchange is a result of the electrons having come from the same donor atom and being coupled with the receiving ions' spins. If the two next-to-nearest neighbor positive ions are connected at 90 degrees to the bridging non-magnetic anion, then the interaction can be a ferromagnetic interaction.

The presence of the emission band at 378 nm is attributed to the presence of trap states. These trap states are associated with structural defects, due to incorporation of Zn ions in interstitial sites of the host lattice and other defects. The same occurs for the 5% and 7% doping concentration of $Zn_{(1-x)}Fe^{+2}_{(x)}O$, where x is the Fe⁺² dopant concentration with x = 0, 5%, and 7%. Also, the 7% dopant concentration sample of Figure – 33 shows a quenching effect in the 362 nm band. The PL spectrum of Figure – 34 for Fe⁺² doped ZnO annealed at 700C in air were totally inverse to the previously discussed spectra.

The PL spectra of pure and Fe (II) ZnO films annealed at 700⁰ C in air are shown in Figure – 33 and Figure – 34. For 5% of dopant concentration, there is a quenching-by-concentration effect in the UV emission that was observed and attributed to the formation of trapping states by the dopant species. This quenching in photoluminescence occurs when the dopant concentration is so high that the probability of non-radiative transitions exceeds that of emission [73]. The evident dependence of the emissions at 362 nm and 388 nm with the Fe (II) concentration can be observed in Figure – 34. The PL spectra exhibited an intense UV emission peak at 388 nm for the pure ZnO sample. The UV emission increased due to the recombination of free excitons through an exciton-exciton collision process [48]. So, the PL spectra clearly represents the effect of increasing Fe content in ZnO host by showing a peak shift in UV emission.

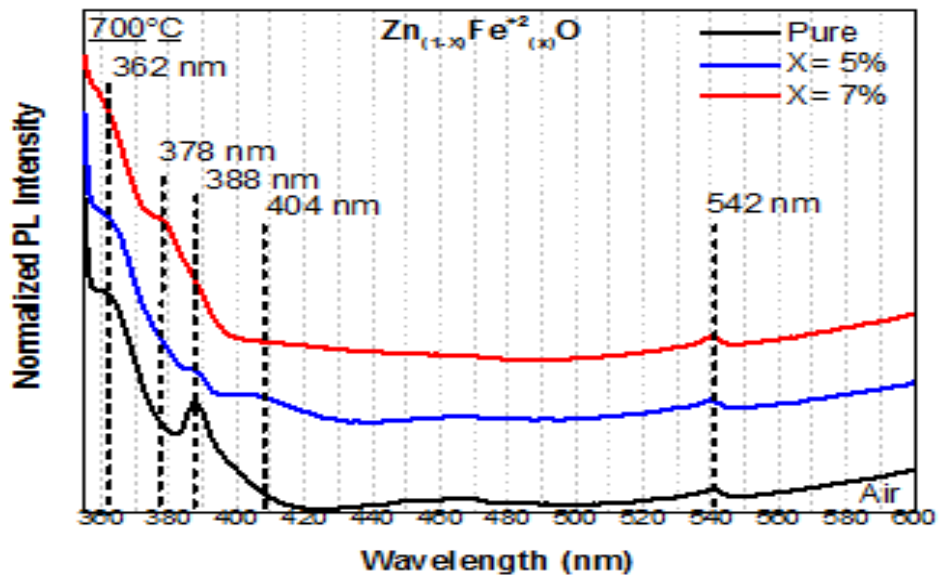


Figure – 34: Room temperature PL spectroscopy for Fe (II)-ZnO annealed at 700°C in air, with dopant concentration of $x= 0, 5\%$, and 7% .

The intensity of the UV emission in the PL for Fe²⁺(0.05 at.%) doped ZnO nanoparticles decreased relative to pure ZnO and the peak related to the violet emission did not present quenching. This quenching in photoluminescence has been observed in other systems when the concentration of the dopant becomes so high that the probability of non-radiative transition through trapping states exceeds the probability of radiative transition [96]. It causes the excitation energy to start migrating through lattice vibrations [96]. Furthermore, the UV emission raised due to the recombination of free excitons through an exciton-exciton collision process [74]. The PL spectra clearly represent the effect of increasing Fe content in ZnO host by showing a peak shift in UV emission.

It is observed that the peak is initially shifted towards the lower wavelength side (for Fe-content 5 at. %) and then to the higher wavelength side (for Fe-content 7 at. %) by quenching the intensity of peak with the increment of Fe concentration in the films. This variation in peak position indicates the variations in the band gap of the films and the quenching of peak intensity might be due to Fe-doping effect [75]. Chen et al. also studied and reported a similar PL behavior of Fe-doped ZnO films prepared by RF magnetron sputtering process [68].

Over the years, oxygen vacancies were believed to be the dominant shallow donors in ZnO. Now, it is becoming clear that these vacancies are formed in noticeable concentrations only after electron irradiation. The green luminescence band in ZnO is commonly attributed to transitions from the oxygen vacancy (V_O) to the valence band. However, it is easy to show that such transition is highly unlikely in n-type ZnO. Problems in the identification of point defects are widely discussed in the literature, from theoretical and experimental points of view [76].

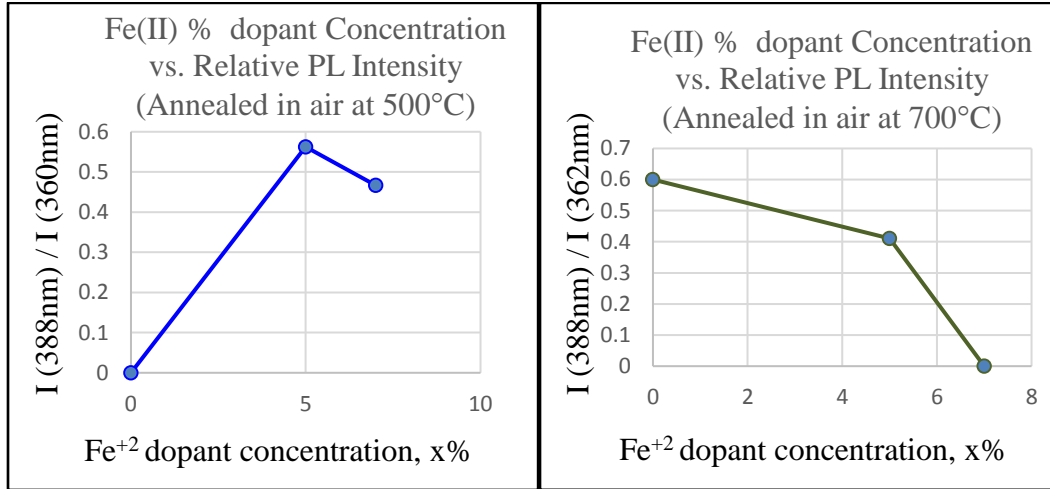


Figure – 35: Room-temperature PL relative intensity for Fe^{2+} -doped ZnO thin films, at different dopant concentrations x , (a) annealed at 500°C, and (b) annealed at 700°C in air.

The major drop in the intensity of the main emission was observed in Fe^{2+} (7 at%) doped ZnO at 500°C where the intensity of the main emission peak decreased 90% relative to pure ZnO. The quenching of UV emission band is presented qualitatively in Figure – 35(b). The intensities ratio of emission bands in presence of interstitials defects decreased as dopant concentration increased, as shown in the Figure – 35(b).

4.2.3 Magnetic Properties of Films of Fe(II)-ZnO Annealed in Air

The M-H loops at room-temperature of Fe (II) doped ZnO films, with $x= 0$ at.%, 5 at. % and 7 at. %, are shown in Figure – 36 and Figure – 37, annealed in air at 500°C and 700°C, respectively. The diamagnetic signal part, was subtracted from the raw information. There was an overlap in the pure ZnO sample in the Figure – 36. The saturation magnetization varied from 0.6 m (emu/cm^3) to 0.4 m (emu/cm^3) for the ZnO doped by Fe^{2+} annealed at 500°C and 700°C, respectively. Almost all the samples displayed a weak paramagnetism, which evidences that the critical temperature of this material is above room temperature [53-54].

The increase in the M-H slope is attributed to the higher concentration of available spins in the sample with the higher dopant concentration. These samples did not exhibit coercivity. Some authors attribute the magnetic response of Fe^{2+} -doped ZnO to the formation of magnetite clusters in the ZnO host [37]; however, as was reported by Blasco et al. the formation of magnetite during the Fe doping of ZnO depends on the synthesis method and synthesis conditions such as temperature, pressure, or inert atmosphere [54].

Literature suggests that magnetism in DMSs would be established only at concentrations that lie far below the percolation threshold. This is associated with nearest-neighbor cation coupling and there is a change in the magnetic features of the DMSs above this threshold, like the presence of a paramagnetic response [2]. In our case, there was no systematic effect of dopant concentration on the magnetization. The observed paramagnetic response could be fostered by the existence of oxygen vacancies and the presence of zinc in the ZnO interstitials site.

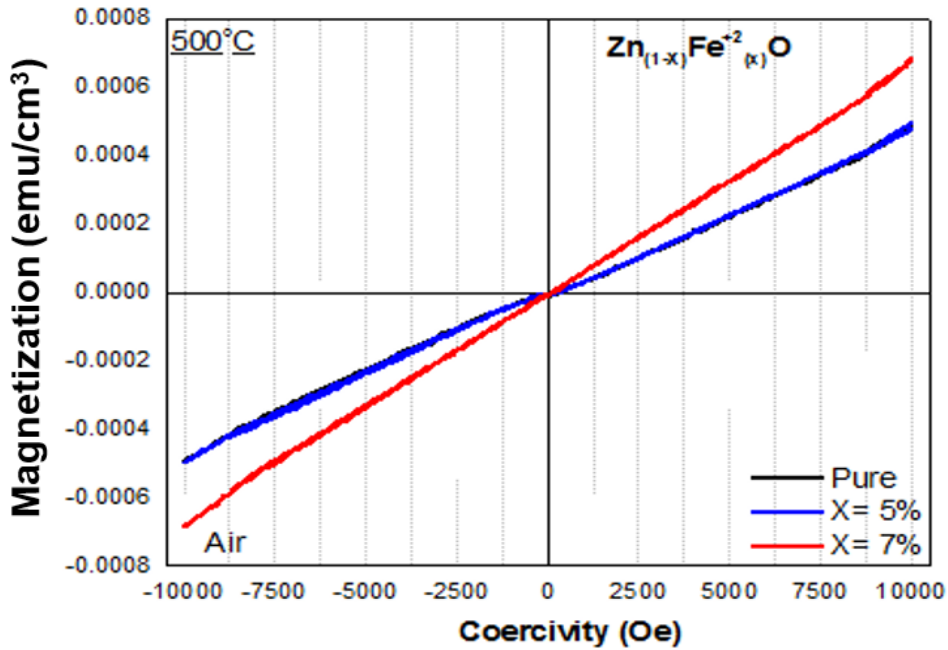


Figure – 36: Room temperature M-H loop for Fe (II)-ZnO thin films annealed at 500°C in air, for one hour.

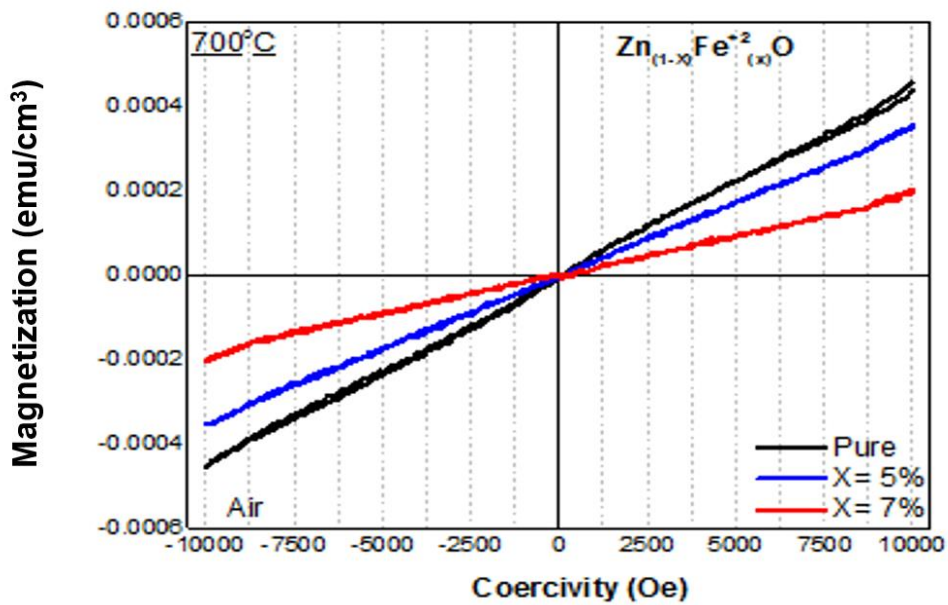


Figure – 37: Room temperature M-H loop for Fe (II)-ZnO thin films annealed at 700°C in air, for one hour.

In materials exhibiting paramagnetic behavior, some of the atoms or ions in the material have a net magnetic moment due to unpaired electrons in partially filled orbitals such as that in transition metals and some rare earth elements. Moreover, a defect induced paramagnetism can be explained in terms of the bound magnetic polarons induced by structural defects (Zn_i). This weak paramagnetism reinforces the hypothesis of an actual incorporation of the dopant species into the ZnO host. A similar behavior in magnetic properties in Fe-ZnO nanoparticles was reported by Wang et al. [37]. The exchange interaction produces the spin polarization of conductive electrons. These spin polarized conductive electrons produce an exchange interaction with the local spin-polarized electrons of other Fe^{2+} ions. Then, through a long-range exchange interaction, almost all Fe^{2+} ions exhibited the same paramagnetic spin direction.

Figure – 36 and Figure – 37 show pure ZnO paramagnetic responses. In a paramagnetic host, this fact has more important consequences for small concentration of magnetic ions. Each ion produces the oscillating magnetization around itself that in-turn generates a magnetic field which acts on the other ions. Hence, there is long range and oscillating interaction between the free carriers. This is known as the Ruderman–Kittel–Kasuya–Yoshida (RKKY) interaction, which is the main coupling mechanism in III–V and II–VI DMS materials [116]. Oxide DMSs usually exhibit low conductivity, and magnetic coupling is localized by oxygen vacancies in hydrogen like orbits, unlike the RKKY model [116]. The observed magnetic moments in oxide DMS materials have also been explained based on formation of a bound magnetic polaron (BMP) [116]. The BMP model was based on the fact that when carrier concentration exceeds a certain value an impurity band is formed and the magnetic dopants couple with localized carriers [116]. According to RKKY interactions, in doped DMS impurity spin has an exchange interaction with the conduction electrons [116].

As a result, local electric and magnetic fields are generated when magnetic ions are present in a paramagnetic host. However, Zn vacancies can be present in these sols and due to the interaction of Zn atoms, nearest to the Zn vacancy, with O-2p electrons, paramagnetic behavior in ZnO sol was observed [116].

4.2.4 Remarks:

A sol-gel method synthesis process was developed to produce Fe (II)-doped ZnO thin films. A hexagonal wurtzite of ZnO structure was evident, without unwanted impurity phases, annealed in air. As we expected the Fe ions were inserted in the wurtzite structure. As annealing temperature increases, there is shift to lower and then to higher 2-theta angles, which could suggest an expansion and contraction by oxygen vacancies as annealing temperature increases. However, Fe²⁺ evidence a stronger quenching of these emissions by dopant concentration effect. This indicates that the oxidation state of iron plays an important role in the optical properties of the material. For the Fe²⁺ doped samples, a quenching of the emission intensity by the dopant concentration was observed.

The least controversial emission from inter band transition occurred in the range of 382 nm – 390 nm for all the samples, where an electron from the free exciton (FX) level recombines with a hole in the VB. The blue region of the emission contains two probable transitions related to V_{Zn} and Zn_i, i.e. an electron from CB recombines with the hole at V_{Zn} or an electron is captured by Zn_i then recombines with the hole in the VB [114].

The M-H hysteresis loops at room temperature did not display coercivity while the magnetization increased with the increase of the iron content. Both annealing conditions in air at 500°C and 700°C exhibited paramagnetic responses at room temperature. The films exhibited hexagonal wurtzite structure, which is more favorable for creating magnetic properties. Zn vacancies have been shown to be the cause of paramagnetic responses, due to Zn deficiency. In the literature this paramagnetic behavior at room temperature is attributed to the exchange interaction between local spin- polarized electrons and conductive electrons interactions.

4.3 Fe (II)-ZnO Thin Films Annealed in Nitrogen Atmosphere

4.3.1 Structural Properties of Films of Fe (II)-ZnO Thin Films Annealed in Nitrogen Atmosphere

4.3.1.1 X-Ray Diffraction (XRD) of Fe (II)-ZnO Thin Films Annealed in Nitrogen Atmosphere

Figure – 38 and Figure – 39 show the XRD patterns for Fe⁺² doped ZnO films deposited onto silicon and annealed in a nitrogen atmosphere at 500°C and 700°C, respectively. Three peaks related to (100), (002) and (110) planes were observed in the XRD pattern for the samples annealed at 500°C. For the samples annealed at 700°C the (002) peak became prominent. No impurity peaks related to Fe₂O₃ or FeO were observed in XRD pattern. From the pattern, it is clear that deposited films were in single phase and highly oriented along the c-axis. The average crystallite sizes were calculated by Scherrer's equation, see below Table – 4; i.e. as dopant concentration increased, the average crystallite size decreased.

Table – 4: Average crystallite size of Fe (II)-ZnO thin films in nitrogen atmosphere.

$x = \text{Fe}^{+2}$ at. %	T=500°C	T=700°C
0	22 nm	47 nm
5	19 nm	18 nm
7	20 nm	17 nm

Figure – 39 evidences a small shift of the (002) diffraction peaks for the 5at% Fe (II)-ZnO sample, towards higher 2θ values. Then, it is suggested, the samples annealed in nitrogen atmosphere prevent the oxidation of Fe⁺² ions into Fe⁺³, contrasting with the air annealing of samples in air.

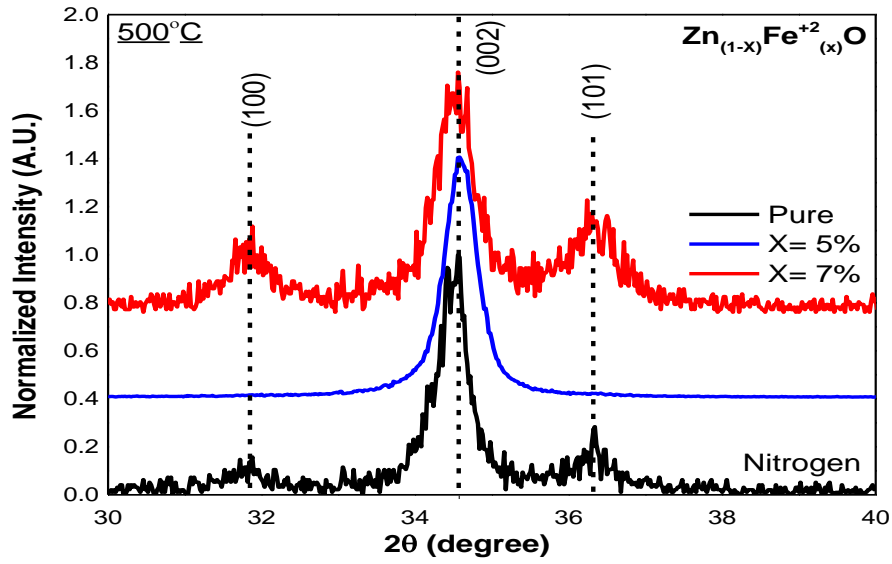


Figure – 38: XRD for Fe (II)-ZnO thin films annealed at 500°C in nitrogen atmosphere, for one hour.

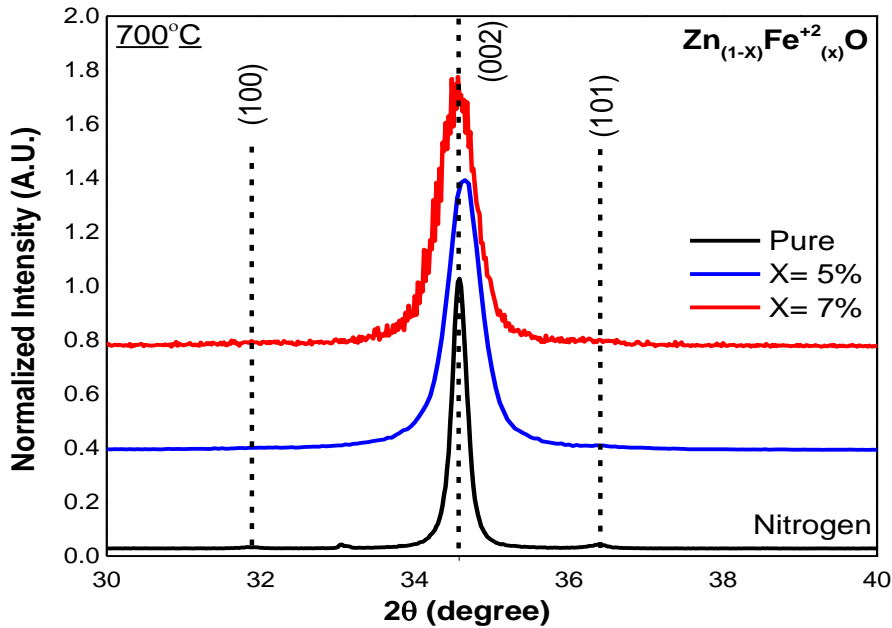


Figure – 39: XRD for Fe (II)-ZnO thin films annealed at 700°C in nitrogen atmosphere, for one hour.

On the other hand, the sharpness of (100), (002), and (101) peaks increased gradually with the annealing temperature, suggesting an improvement of the film's crystallinity (Figure – 39). The absence of impurity phases suggests the incorporation of Fe^{+2} (0.76 Å) in the Zn^{+2} (0.72 Å) sites. The average crystallite size was calculated using the Scherrer's equation [35] and presented in Table – 4. Comparing the annealing atmosphere, a better control of the crystallinity was attained in a nitrogen atmosphere. Compensation by nitrogen ions is suggested when annealing in nitrogen atmosphere, this does not promote oxygen vacancies.

4.3.1.2 SEM Analyses of Fe (II)-ZnO at Annealed at in Nitrogen Atmosphere

The SEM images corresponding to Fe-ZnO films (5 at.% Fe and 7 at.% Fe) are shown in Figure – 40. Both samples were annealed at 500°C for 1 hour. The micrographs evidence the uniformity and homogeneity of the films and suggests the formation of sub-micrometric grains.

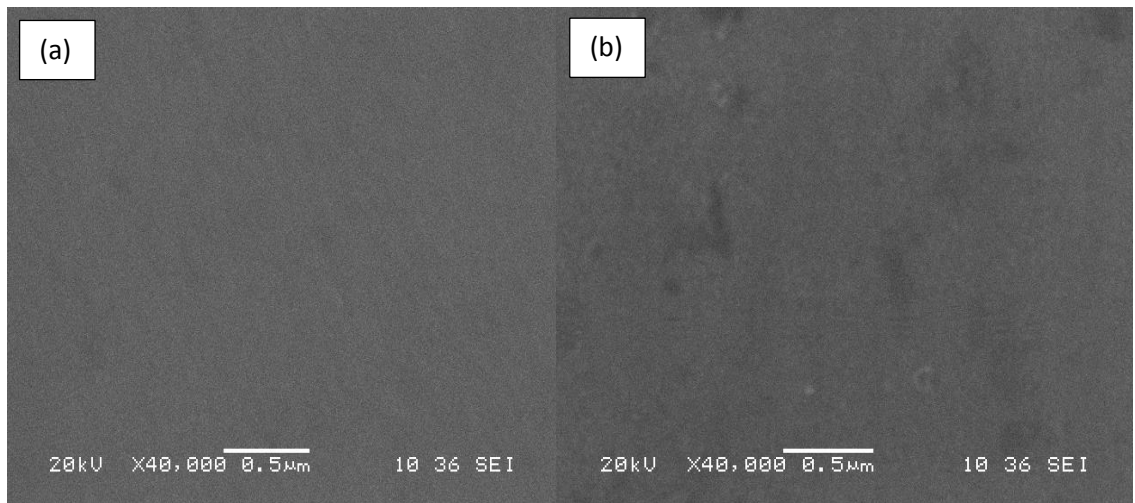


Figure – 40: SEM images of Fe (II)-ZnO annealed at 700°C in a nitrogen atmosphere. (a) at. 5% Fe and (b) at. 7% Fe.

4.3.2 Optical Properties of Fe (II)-ZnO Thin Films Annealed in Nitrogen

4.3.2.1 Photoluminescence Spectroscopy of Fe (II)-ZnO Thin Films Annealed in Nitrogen

The room temperature photoluminescence (PL) spectra of Fe⁺² doped ZnO thin films, were obtained using an excitation wavelength of 345 nm, and are shown in Figure – 41 and Figure – 43. These spectra clearly evidenced the main emission peak at 363 nm and others at 377 nm and 387 nm, respectively for 5 at. % and 7at. % dopant concentration. A peak at 540 nm for both Fe dopant concentrations, are attributed to the vacancies of oxygen. It is evident that when annealed in a nitrogen atmosphere, there is a control of the defects of the material. For the 7% dopant concentration, there is an increase of the photoluminescence intensity in the 363 nm band.

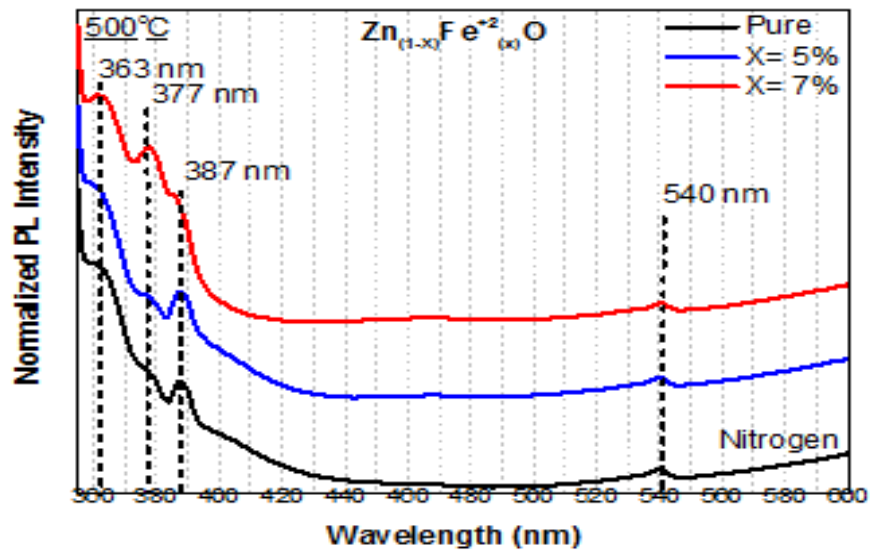


Figure – 41: Room temperature PL spectroscopy for Fe (II)-ZnO annealed at 500°C in nitrogen atmosphere with dopant concentration of $x= 0, 5\%$ and 7% .

For the sample annealed at 500°C, the PL spectra, in Figure – 41, show an increase in intensity in the 363 nm band for 7% dopant concentration, with a remarkable change in the emission characterized by a decrease of the defect (i.e., visible) emission and the appearance of the UV emission around 377 nm and 387 nm. This behavior strongly indicates that oxygen vacancies are at the origin of the defect emissions in the visible region, which supports our previous analysis that the defects are due to oxygen vacancies.

The strong emission peaks centered on 363nm and 387 nm are attributed to the excite emission and transition of shallow donor levels near of the conduction band to valence band, respectively, in Figure – 41. According to Chen’s work on thin films, the incorporation of Fe (II) ions would lead to an increase of the concentration of interstitial Zn. On this basis, it can be that Fe (II) ions fostered the increase of defects of the interstitial Zn type associated to the 387 nm emission peak for 5% dopant concentration [77].

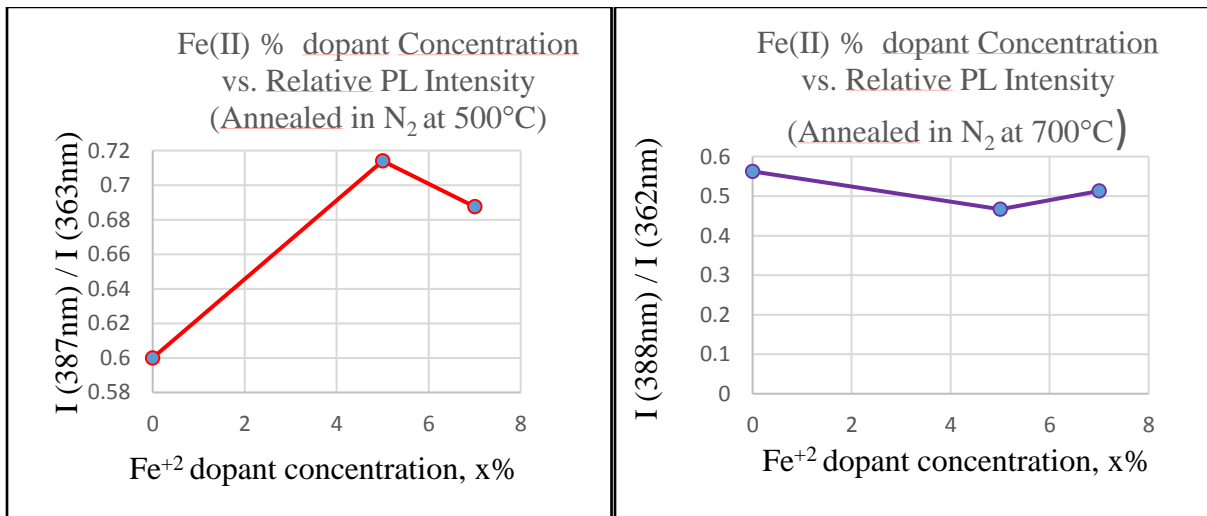


Figure – 42: Room-temperature PL relative intensity for Fe²⁺ doped ZnO thin films, at different dopant concentrations x , (a) annealed at 500°C and (b) annealed at 700°C in N₂ atm.

The relative increment in the 387 nm peak intensity with respect to the one at 362 nm (Figure 42 (a)) may suggest the increase of the concentration trend of trap states associated Zn^{2+} to the incorporation in interstitial sites (zinc interstitials) [78]. Figure 42(b) shows a little decreasing of the defects as the dopant concentration as the N_2 atmosphere annealed at $700^\circ C$ increases. The slight decrease in the defect emissions indicated that the N_2 annealing atmosphere at $700^\circ C$ significantly reduces the oxygen deficiency. Nonetheless, the annealing in N_2 results in an overall decrease of the emission intensity. N_2 atmosphere leads to an increase in the UV emission and a comparatively slight decrease in the defect emissions.

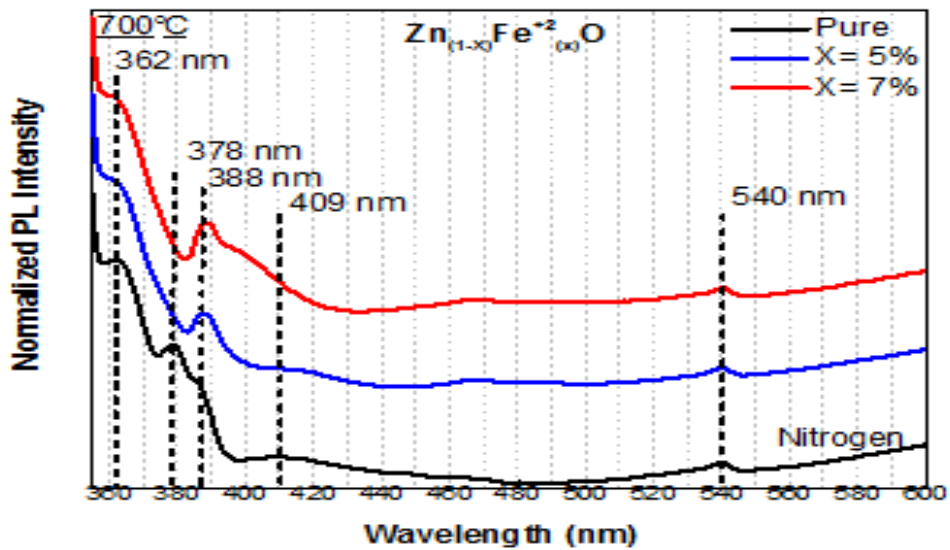


Figure – 43: PL spectroscopy for Fe (II)-ZnO annealed at $700^\circ C$ in nitrogen atmosphere, with dopant concentration of $x= 0, 5\%$, and 7% .

Figure – 41 and Figure – 43, evidence the strong dependence of the emission band intensity with Fe concentration in 362 nm. The intensity of this emission band decreases as the dopant concentration increases, this suggests a quenching-by-concentration effect. This quenching in

photoluminescence has been observed in other systems when the concentration of the dopant becomes so high that the probability of non-radiative transition through trapping states exceeds the probability of radiative transition [37]. The 388 nm band, is a near band edge, which is related to the violet emission related to interstitial zinc (Zn_i) [115].

4.3.3 Magnetic Properties of Fe(II)-ZnO Films Annealed in Nitrogen

Figure –44 and Figure – 45 show the variation of the slope of magnetization with an external magnetic field at different dopants concentration of Fe^{+2} annealed at 500°C and 700°C for one hour. Subtraction of the diamagnetic components was made to all the samples to improve the magnetic component signal. Only a paramagnetic response was observed. The enhanced antiferromagnetic interaction between neighboring Fe–Fe ions suppressed the ferromagnetism in presence of the dopant species. Similar trends were observed by other researchers in Co-doped ZnO [37]. Available literature suggests that ferromagnetism in DMS's would be established only at concentrations that lie far below the percolation threshold. The percolation threshold is associated with nearest-neighbor cation coupling and above of this threshold there is a change in the magnetic features of the DMS's in the presence of a paramagnetic response [38]. This weak paramagnetic behavior cannot be attributed to the presence of parasite phases as oxides since there is good spectroscopic evidence that Fe^{+2} substitutes Zn species in the wurtzite structure [2].

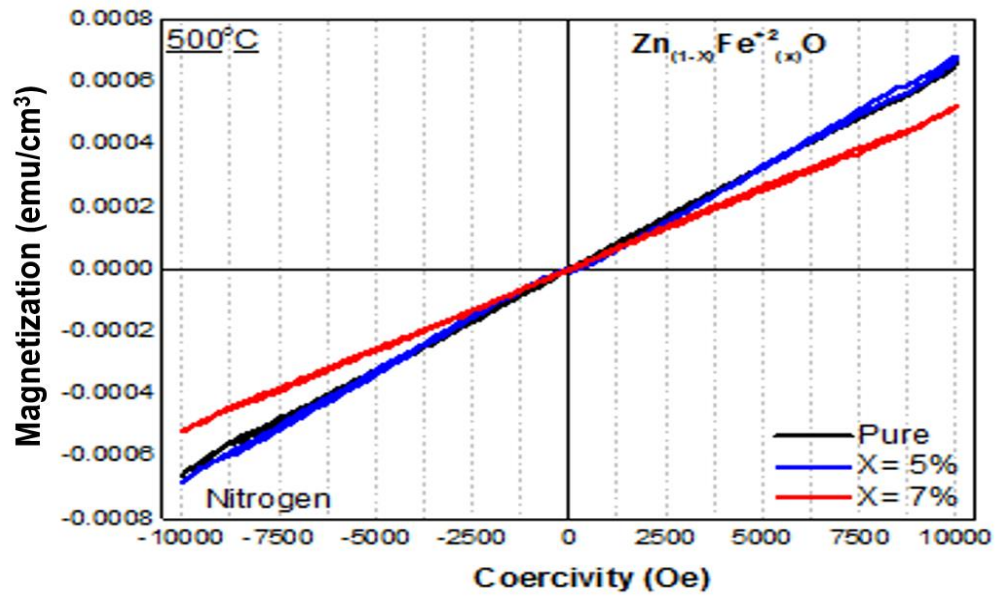


Figure – 44: Room temperature M-H loop for Fe (II)-ZnO annealed at 500°C in nitrogen atmosphere.

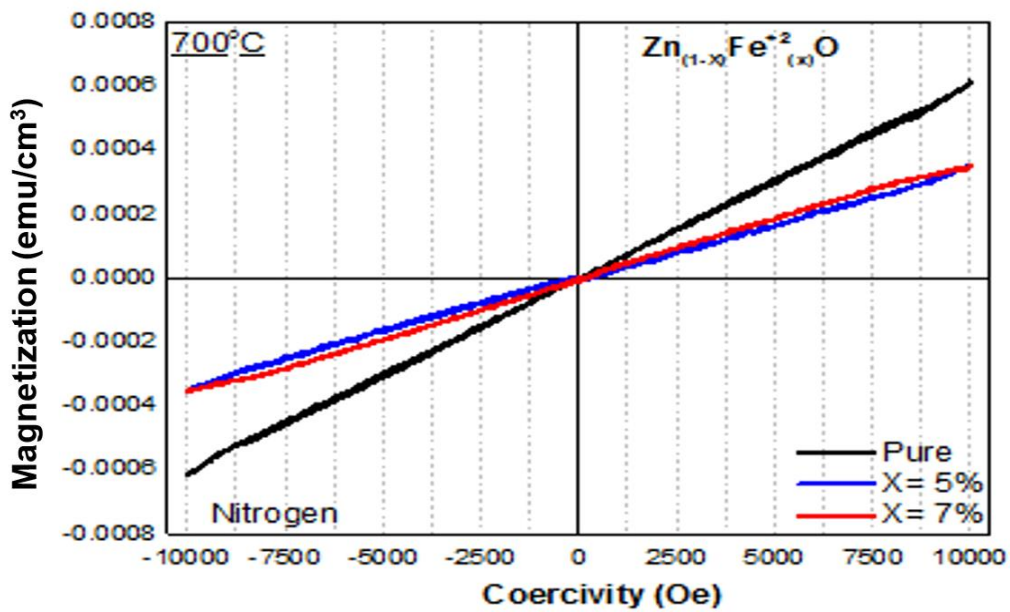


Figure – 45: Room temperature M-H loop for Fe (II)-ZnO annealed at 700°C in nitrogen atmosphere.

4.3.4 *Remarks:*

XRD confirmed the development of well crystallized Wurtzite-ZnO structure without the presence of secondary phases and an average crystallite size of 15 nm. Doped ZnO films exhibited preferential growth along the (002) plane. SEM analyses evidenced a homogenous film without cracking. XRD results suggest the incorporation of Fe dopants in the ZnO host. The presence of intrinsic defects in ZnO nanoparticles was suggested by PL spectroscopy measurements. The emission peaks observed at 388 nm is attributed to the generation of trap states due to interstitial Zn in the host oxide. The quenching-by-concentration effect in luminescence was also observed in the doped samples. The film shows a paramagnetic response.

4.4 Fe (III)-ZnO Thin Films Annealed in Air

4.4.1 Structural Properties of Fe (III)-ZnO Thin Films Annealed in Air

4.4.1.1 X-Ray Diffraction (XRD) of Fe (III)-ZnO Thin Films Annealed in Air

The XRD patterns of Fe (III)-ZnO films for (x = 0, 5 and 7 at. %) are shown in Figure – 46 and Figure – 47, for annealing temperatures of 500°C and 700°C, respectively. No impurities were detected. The main peak corresponds to (002) plane, whereas, the peak at 33° can be assigned to the substrate peak. As before, there is preferential growth along the ‘c’ axis orientation for all the samples.

As Figure – 46 also suggests, the diffraction peaks decreased in intensity in presence of the dopant species. For thin films annealed at 500 °C, the difference of the ionic radius of Zn²⁺ (0.74 Å) compared with that of Fe³⁺ (0.64 Å), supports the actual substitution of Zn by Fe(III) species; however, the expected shift of the XRD peaks towards larger diffraction angles was not observed. The same situation was observed in the XRD patterns of the Fe (III) doped ZnO thin films, annealed in air at 700 °C (Figure – 47). This trend is contradictory, although it could be attributed to a subsequent generation of cationic vacancies to keep the electrical neutrality in the resulting structure. For instance, the incorporation of two Fe (III) species would demand the exchange with three Zn (II) species, causing the generation of a cationic vacancy and the subsequent enhancement of the repulsive interaction between oxygen sites [1].

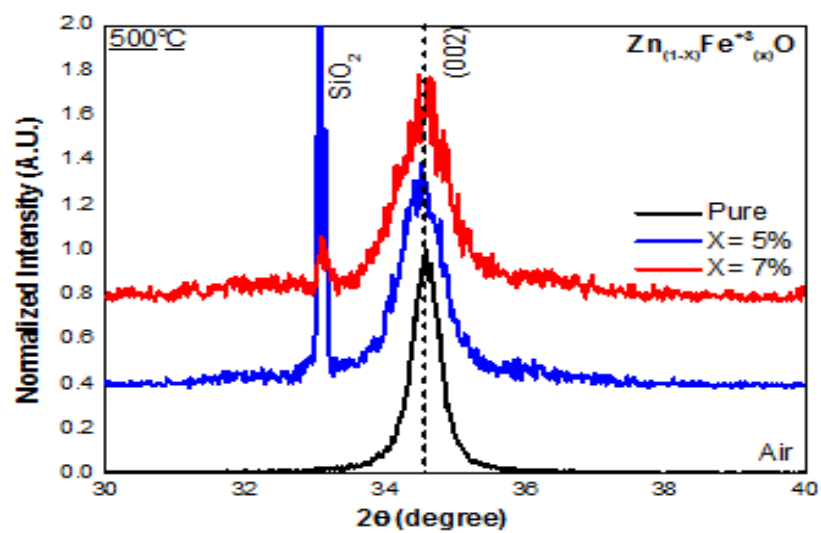


Figure – 46: XRD for Fe (III)-ZnO thin films annealed at 500°C in air, for one hour.

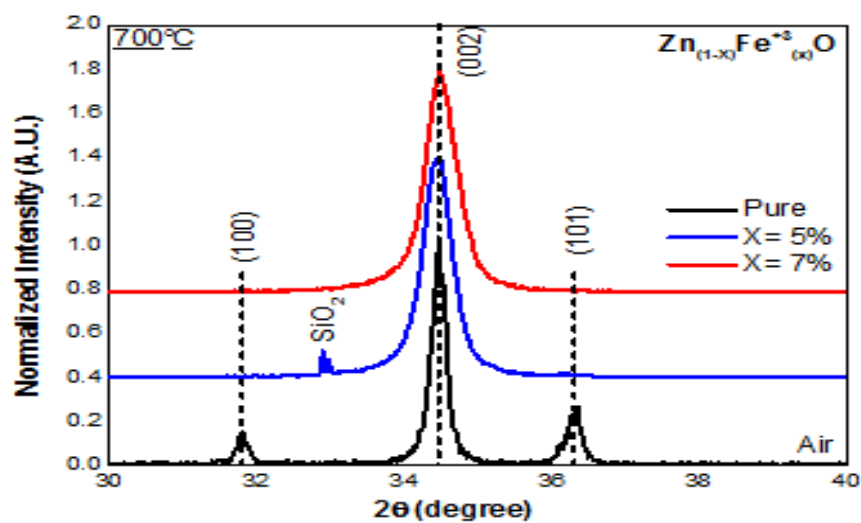


Figure – 47: XRD for Fe (III)-ZnO thin films annealed at 700°C in air, for one hour.

Table – 5: Average crystallite size of Fe (III)-ZnO thin films annealed in air at two different temperatures

$x = \text{Fe}^{+3}$ at%	T=500°C	T=700°C
0	21 nm	49 nm
5	16 nm	20 nm
7	15 nm	19 nm

Table – 5 suggests a decrease in particle size with increasing dopant concentration. Sharma *et al.*, [80] reported that the wurtzite structure of ZnO nanoparticles gradually degrades with the increasing Fe doping concentration leading to smaller crystal sizes. The same behavior has been observed in the doping of ZnO with other trivalent ions such as V^{3+} , Sc^{3+} , and Al^{3+} . A decrease in the crystal quality was observed with an increase in dopant concentration,[80].

4.4.2 Optical Properties of Fe (III)-ZnO Thin Films Annealed in Air

4.4.2.1 PL Spectroscopy of Fe (III)-ZnO Thin Films Annealed in Air

The room temperature photoluminescence (PL) spectra of Fe (III)-ZnO thin films annealed at 500°C and 700°C, using an excitation wavelength of 345 nm, are shown in Figure – 48 and Figure – 49, respectively. The spectra look very similar evidencing the presence of two strong emission peaks centered on 362 nm and 387 nm, which are attributed to the exciton emission and transition of shallow donor levels near of the conduction band to valence band, respectively. Other bands in the visible region (408 nm and 540 nm) are present in most of the samples. These bands are usually attributed to lattice defects like oxygen vacancies [2, 39, and 40].

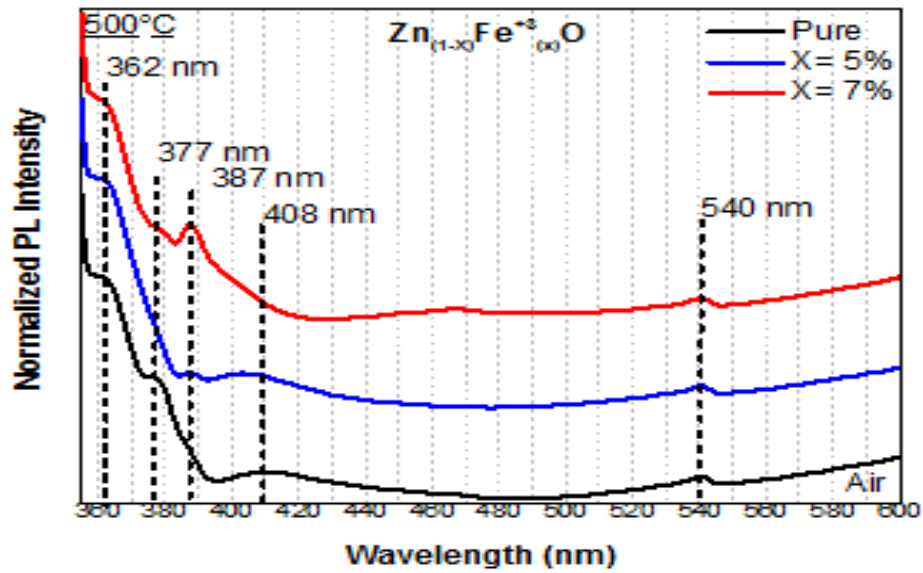


Figure – 48: PL spectroscopy for Fe (III)-ZnO annealed at 500°C in air, with dopant concentration of $x=0$, 5%, and 7%.

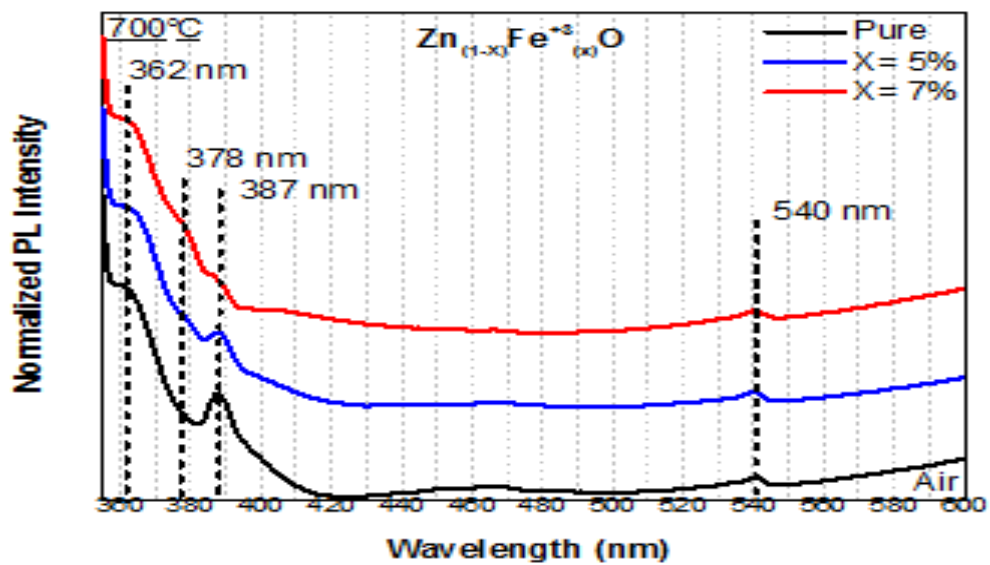


Figure – 49: PL spectroscopy for Fe (III)-ZnO annealed at 700°C in air, with dopant concentration of $x=0$, 5%, and 7%.

The incorporation of Fe (III) ions into the ZnO lattice induced a weaker quenching-by-concentration effect in the 362 nm-UV. Similar behavior was reported in another trivalent (Al^{3+}) doping ZnO system [80].

The corresponding spectra also show the band-band transition related to recombination of the electron-holes pairs at 362 nm (band gap 4.32 eV) and a very intense emission at 390 nm, attributed to transitions from shallow donor levels produced due to the presence of Zn_i [76]. The small band centered on 377 nm can be attributed to transitions from hydrogen interstitial (H_i) levels in ZnO, which usually overlap the Zn_i levels [37].

A quenching by dopant concentration is observable in the 387 nm band. The evolution of the $I_{362\text{nm}}/I_{387\text{nm}}$ ratio with the increase of Fe^{3+} content is presented in Figure – 50. The intensity of the emission at 362 nm is 10% higher in the pure ZnO based thin films relative to the emission at 387 nm, but for samples at 7 at. % the UV emission is 12% higher than the violet emission. The green emission vanished in all doped samples suggesting that some of the dopant species are filling the oxygen vacancies related with this emission.

In general, the 500°C and 700°C samples show an increasing relative intensity as the dopant concentration increased, which represents an increase of defects. Inversely, there were decreasing relative intensities as the dopant concentration increased, promoting less defects (Figure – 50).

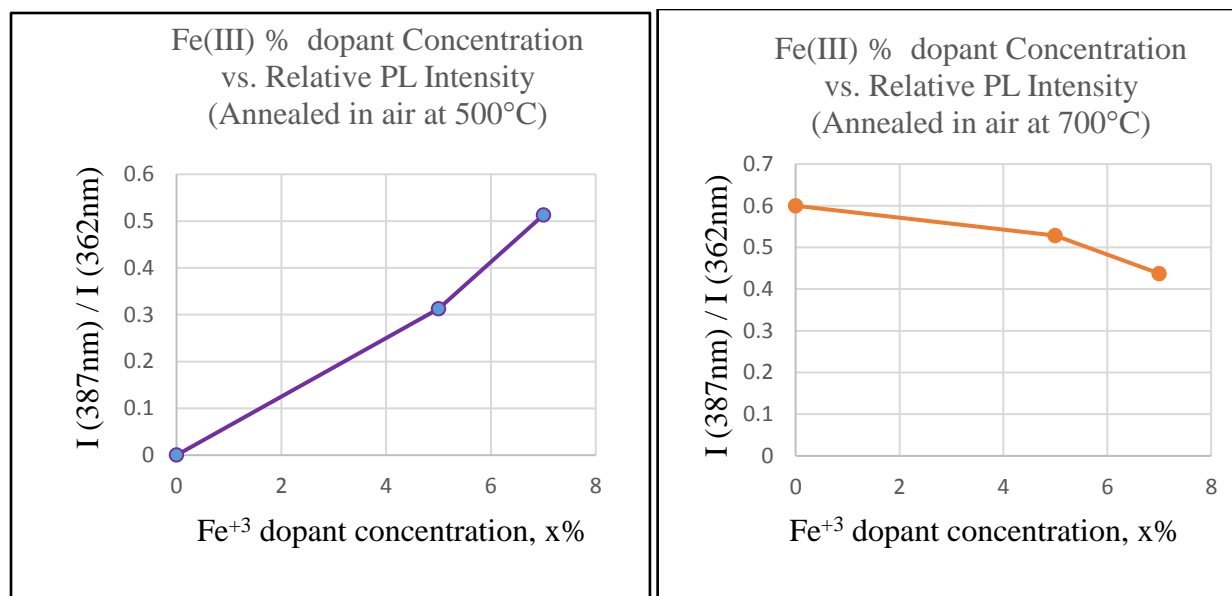


Figure – 50: Room-temperature PL relative intensity for Fe^{3+} -doped ZnO thin films, at different dopant concentrations x , (a) annealed in air at 500°C and (b) at 700°C.

4.4.3 Magnetic Properties of Fe(III)-ZnO Films Annealed in Air

Figure – 51 and Figure – 52 show the M-H profiles for Fe^{3+} doped ZnO films, annealed at 500°C and 700°C, respectively, and different dopant concentrations. The samples exhibited a paramagnetic behavior. The maximum magnetization values were low and varied between 0.7 emu/cm^3 and 0.4 emu/cm^3 . Increasing the annealing temperature caused a decrease of magnetization. Similarly, the Fe^{3+} doped ZnO samples annealed at 700°C in air, show a paramagnetic response except for the Fe (III) 5% dopant concentration.

The observed paramagnetic trend reinforces the hypothesis of an actual incorporation of the dopant species into the ZnO host. Sharma et al. [37] reported Fe^{3+} -doped ZnO nanoparticles (3 nm -10 nm) with similar magnetic response to our films although a noticeable coercivity was

observed at lower dopant concentration of iron (2 and 3 at.%). Sharma et al. [37] attributed this behavior to the enhanced antiferromagnetic interaction between neighboring Fe–Fe ions which suppressed the ferromagnetism at higher doping concentrations of Fe.

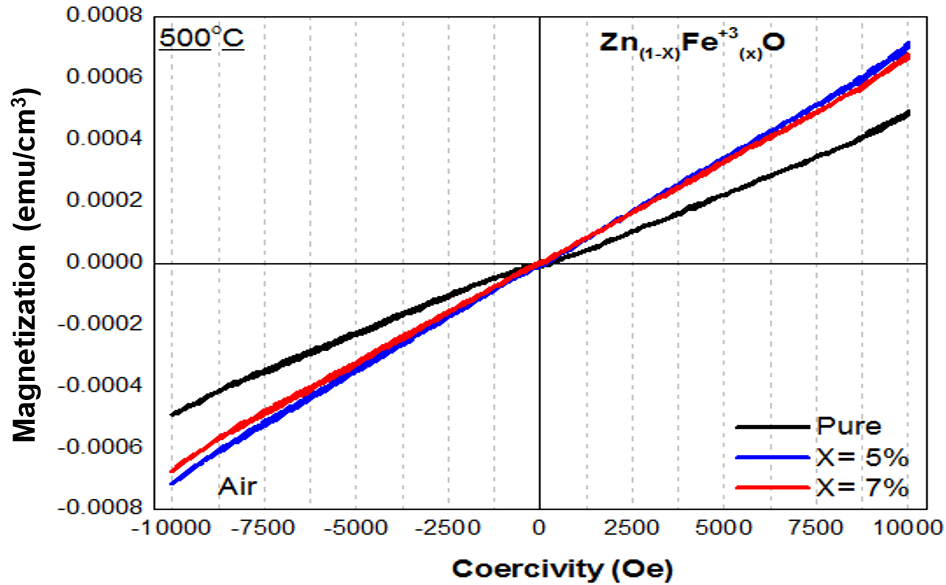


Figure – 51: M-H loop for Fe (III)-ZnO thin films annealed at 500°C in air.

Figure – 52 also shows an evident antiferromagnetic ordering in the Fe (II)-ZnO at 5 at. % of dopant concentration. Literature shows that in Fe-ZnO, the nearest neighboring cations favor the antiparallel alignment, and hence strong antiferromagnetic interactions can take place [105]. Since ZnO is intrinsically non-magnetic, the occurrence of magnetization by impurity substitution suggests that Fe⁺² atoms are the main contributor to the observed magnetization. The observed antiferromagnetism in Fe-ZnO can be attributed to the presence of Fe₂O₃ or ZnFe₂O₄ that are

intrinsically antiferromagnetic in ground state [105]. These phases would have been below the detection limit of the XRD equipment.

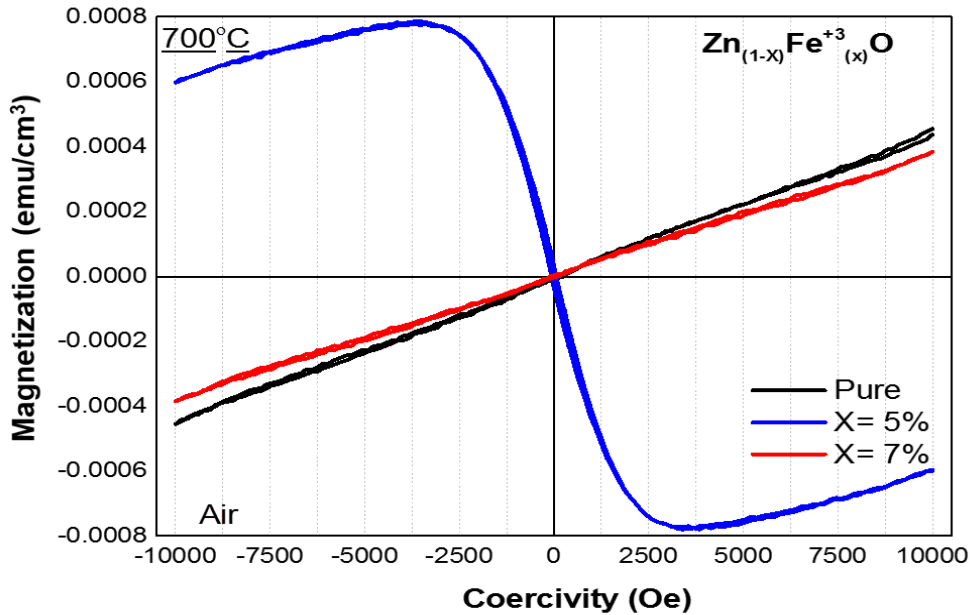


Figure – 52: *M-H loop for Fe (III)-ZnO thin films annealed at 700°C in air.*

In the present work, it is found that the magnetic properties of Fe doped ZnO nanoparticles has not been improved by the sol gel method. We also note that as the Fe concentration in the sample is increased, the magnetization tends to be increased with the applied magnetic field. Previously in TM, transition metal doped oxide systems, it has been reported that as the concentration of magnetic impurities is increased in the host oxide matrix, the saturation magnetic moment decreases, which is attributed to the antiferromagnetic interaction between the dopant species, found Sinhala et al., (2008) [53].

4.4.4 Remarks:

A sol-gel-based synthesis process was developed to produce pure and Iron (III) doped ZnO thin films. Doping of ZnO with Fe^{3+} ions display better optical than magnetic responses. All the doped nanoparticles exhibit strong UV and violet emission at room temperature.

Fe^{3+} induced a stronger quenching of these emission peaks by dopant concentration effect compared with Fe^{2+} doped samples. This indicates that the oxidation state of iron plays an important role in the optical properties of the material. Besides the green emission related to 540 nm, emissions remain for all the doped samples which suggest that some of the dopant species may fill the zinc/oxygen vacancies related with this emission, reinforcing the hypothesis of actual incorporation of the dopant species into the ZnO host.

The samples annealed at 500°C and 700°C exhibited paramagnetic responses at room temperature, but with different features. A 5at.% dopant concentration Fe (III) doped ZnO thin films sample annealed at 700°C showed an antiferromagnetic response. Our work clearly evidences this, in the case of Fe as a dopant for ZnO, the oxidation state principally influences the optical properties.

4.5 Fe (III)-ZnO Thin Films Annealed in Nitrogen Atmosphere

4.5.1 Structural Properties of Films of Fe (III)-ZnO Thin Films Annealed in Nitrogen Atmosphere

4.5.1.1 X-Ray Diffraction (XRD) of Fe (III)-ZnO Thin Films Annealed in Nitrogen Atmosphere

Two peaks related to (002) plane and (101) planes were observed from XRD pattern, see Figure – 53 and Figure – 54. The peak related to (002) is clearly visible by its high intensity. The average crystallite sizes were calculated using Scherrer's equation and are presented in Table – 6. Evidently, the higher the dopant concentration, the smaller the crystallite size.

Table – 6: Average crystallite size of Fe (III)-ZnO thin films annealed at two temperatures in nitrogen atmosphere

$x = \text{Fe}^{3+}$ at%	T=500°C	T=700°C
0%	22 nm	47 nm
5%	16 nm	23 nm
7%	15 nm	20 nm

The XRD patterns of Fe (III)-ZnO thin films synthesized at various dopant concentrations and annealed at 500°C and 700°C are shown in Figure – 53 and Figure – 54, respectively. In general, all diffraction peaks correspond to the ZnO host, which exhibit a hexagonal wurtzite structure. Furthermore, the smaller ionic radius of Fe^{3+} (0.64Å) with respect to Zn^{2+} (0.74Å) would be conducive to lattice distortions in the ZnO host. As suggested by XRD measurements, a clear shift was observed, but towards lower diffraction angles, which is indicative of an expansion of the unit cell. This trend can only be explained in terms of the actual substitution of oxygen ions (1.40Å) by larger nitrogen ions (1.71Å).

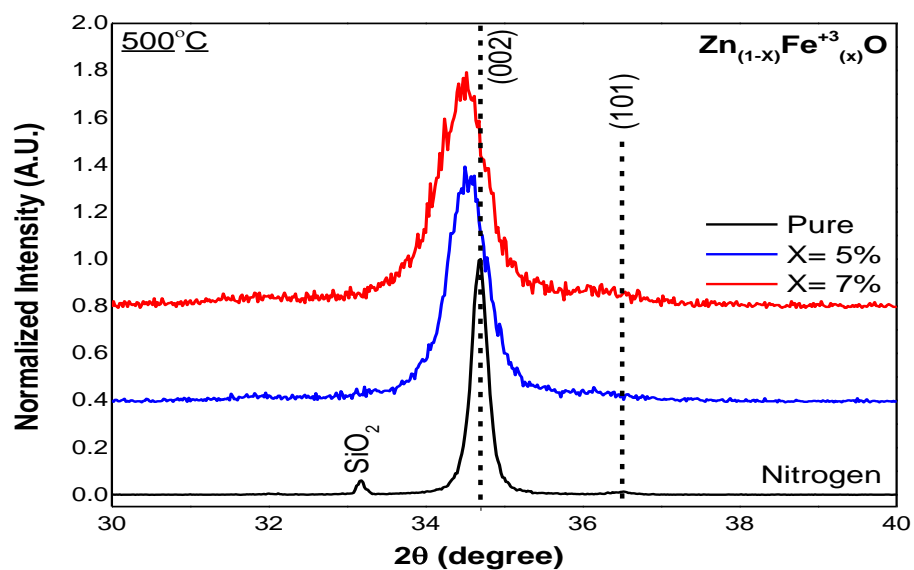


Figure – 53: XRD for Fe (III)-ZnO thin films annealed at 500°C in a nitrogen atmosphere, for one hour.

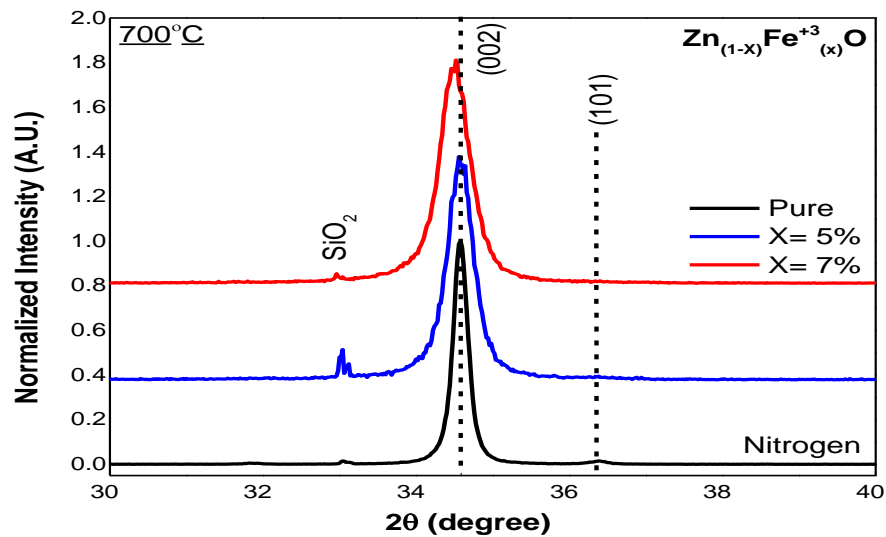


Figure – 54: XRD for Fe (III)-ZnO thin films annealed at 700°C in a nitrogen atmosphere, for one hour.

Increment of annealing temperature in nitrogen atmosphere led to superior and narrower diffraction peaks which correspond to an increase in crystallite size and qualities. The increase in annealing temperature increased the (002) peak intensity, while decreasing those of the (100) orientation [79].

4.5.2 Optical Properties of Films of Fe (III)-ZnO Thin Films Annealed in Nitrogen Atmosphere

4.5.2.1 PL Spectroscopy of Films of Fe (III)-ZnO Thin Films Annealed in Nitrogen Atmosphere

The photoluminescence spectra of Fe (III)-ZnO thin films annealed at 500°C and 700°C are shown in Figure – 55 and Figure – 56, respectively.

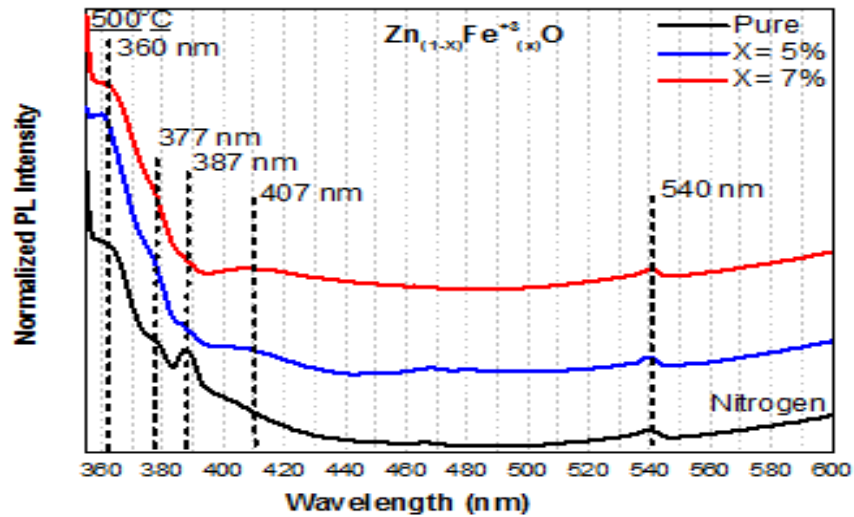


Figure – 55 PL spectroscopy for Fe (III)-ZnO annealed at 500°C in nitrogen atmosphere, with dopant concentration of x= 0, 5%, and 7%.

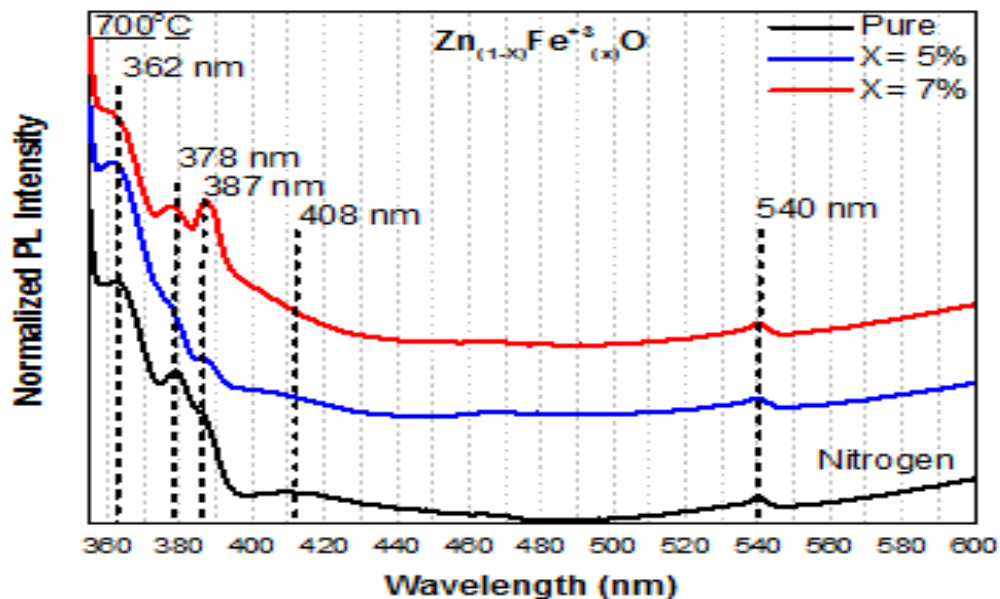


Figure – 56: PL spectra for Fe (III)-ZnO annealed at 700°C in nitrogen atmosphere, with dopant concentration of $x= 0, 5\%$, and 7% .

Figure – 55 and Figure – 56 show the PL spectra of Fe-doped ZnO thin films annealed at two different temperatures. As in the previously described systems, the spectra showed the UV emission at 362 nm and a very weak and broad green emission at 540 nm. The UV emission at 362 nm is related to the near band-edge emission, Viswanatha et al., in 2004, whereas the green emission results from the recombination of electrons with holes trapped in singly ionized oxygen vacancies (Kong et al., in 2001). The corresponding blue-shift of the band edge validates the actual incorporation of Fe in the ZnO lattice [53]. The relative intensities of the samples annealed at 500°C in air, Figure – 57, evidence a decreasing trend with the rise in the dopant concentration that is attributed to the quenching by concentration effect.

A clear trend was not observed in those samples annealed in nitrogen. The probable explanation of this later trend needs to be addressed in future works.

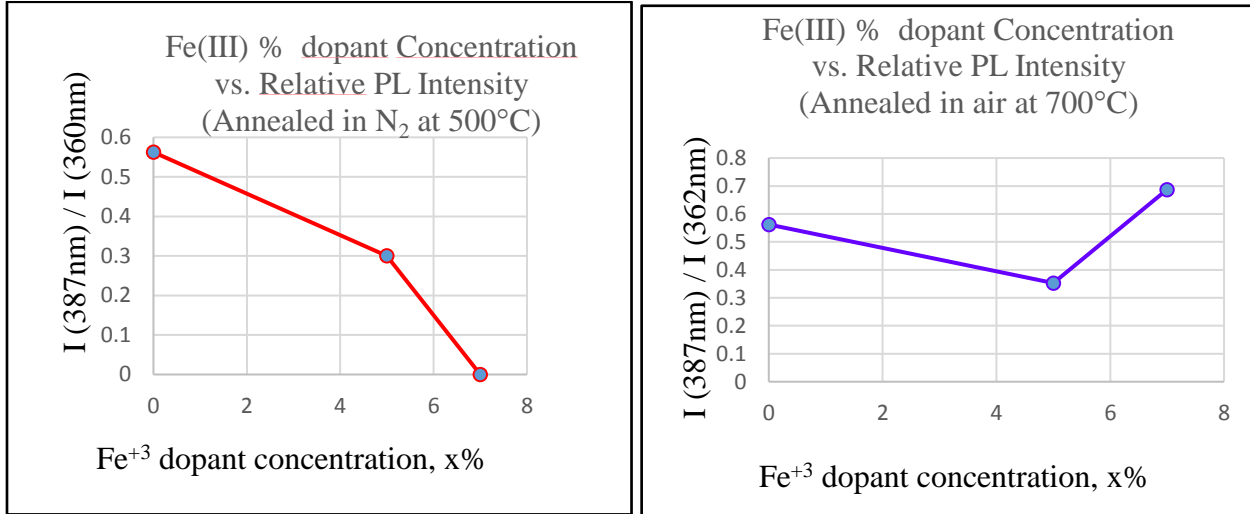


Figure – 57: Room-temperature PL relative intensity for Fe³⁺-doped ZnO thin films, at different dopant concentrations x , (a) annealed in N₂ atmosphere at 500°C and (b) 700°C .

4.5.3 Magnetic Properties of Fe(III)-ZnO Films Annealed in Nitrogen Atmosphere

Figure – 58 and Figure – 59 correspond to the films annealed at two different temperatures. All samples exhibited a paramagnetic behavior. In materials exhibiting paramagnetism, some of the atoms or ions in the material have a net magnetic moment due to unpaired electrons in partially filled orbitals, as found in transition metals and some rare earth elements. Examples include V⁺², Cr⁺², Mn⁺², Fe⁺², Co⁺², and Ni⁺² among the transition elements and Gd⁺³ among the rare earth elements [53].

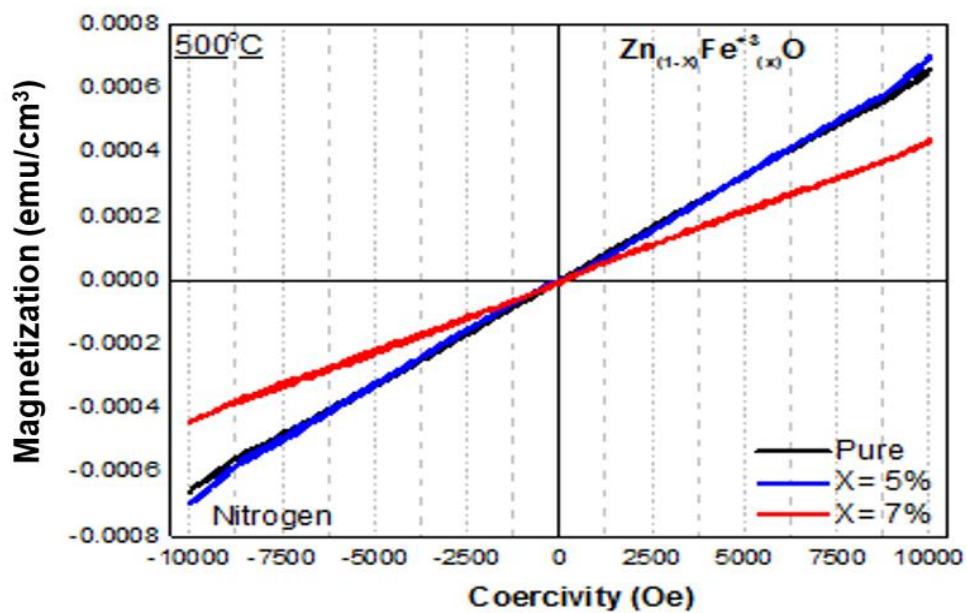


Figure – 58: M-H loop for Fe (III)-ZnO at 500°C in nitrogen atmosphere.

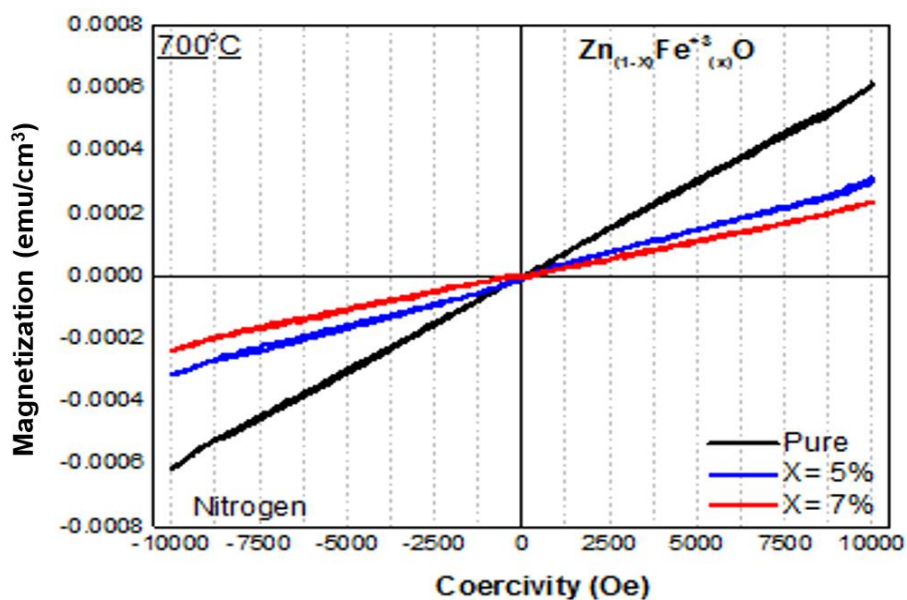


Figure – 59: M-H loop for Fe (III)-ZnO at 700°C in nitrogen atmosphere.

4.5.4 *Remarks:*

A modified sol-gel synthesis process was developed to synthesize Fe (III)-ZnO thin films. A wurtzite structure without secondary phases or impurities in the nanostructures was confirmed in all samples. In the XRD, the Fe (III)-ZnO thin films annealed at 500°C in nitrogen atmosphere, should have shifted to the right, but instead shifted to the left, probably caused by the replacement of oxygen ions (1.40 Å) with nitrogen ions (1.71 Å).

Doping of ZnO with Fe³⁺ ions enhanced optical responses at high concentration of dopants, such as, 5at% dopant concentration Fe (III) doped ZnO thin films sample, annealed at 500°C and 700°C in nitrogen atmosphere, as seen in Figure – 55 to Figure – 67. All the doped nanoparticles exhibited strong UV and violet emission at room temperature. Although, it is notable that doping at 7 at% Fe³⁺ caused the samples to display a more intense violet emission than in pure ZnO. The smaller ionic radii of the dopant should have promoted the distortion in the ZnO host, and hence, the probability of Zn_i formation leading to an intense violet emission. In other words, some of the dopant species may fill the zinc/oxygen vacancies related with this emission reinforcing the hypothesis of actual incorporation of the dopant species into the ZnO host.

5 CONCLUSIONS

The formation of pure, Fe (II) and Fe (III) doped ZnO thin films were confirmed by XRD, SEM, TEM, UV-Vis, and PL measurements. No isolated impurity phases were detected, from 5% at. to 7% at. Fe doped ZnO. We reported the influence of the dopant state and annealing conditions on the functional properties of Fe doped ZnO thin films obtained by spin coating and annealing process.

The structural, morphological, optical, and magnetic properties of sol-gel synthesis of pure and doped ZnO thin films were characterized. The pure and doped ZnO thin films had a hexagonal wurtzite crystallite structure with a preferred orientation along the (002) direction, which was attributed to the surface free energy of (002) plane, which is the lowest in ZnO films, and to the coherency strain induced by the substrate.

XRD confirmed preferential orientation for nanocrystals instead of random orientation. SEM/TEM analyses confirmed the formation of homogeneous films of pure and doped-ZnO thin films. The grains were 50nm or less in size.

The Fe(II) and Fe(III) doped ZnO thin films annealed in air and nitrogen atmosphere between 500°C and 700°C were synthesized by sol-gel technique with no evidence of a secondary phases such as; Fe, FeO, Fe₂O₃, or ZnFe₂O₄. The incorporating Fe (II) and Fe (III) ions into ZnO does not modify the wurtzite crystal structure, therefore confirming the substitution of Zn (II) by the Fe (II) and Fe (III) ions. The XRD shows that there is an expansion and contraction of the lattice as annealed in air and nitrogen atmosphere. XRD also evidenced an oxidation state from Fe (II) to Fe (III) when annealed at higher temperature in air. But, when annealed in a nitrogen atmosphere, the oxidation state of Fe (II) to Fe (III) were not exhibited. The previous suggests that

Fe (II) oxidized to Fe (III) in air annealing, while in nitrogen atmosphere annealing, the oxidation is inhibited or not promoted.

The XRD from the $Zn_{1-x}Fe_xO$, planes gradually shift towards higher diffraction angles with the increase in Fe doping. This gradual shift towards higher diffraction angles may be associated with the valence state of the Fe ions in ZnO, which can exist in the form of Fe^{2+} as well as Fe^{3+} . The ionic radii of Fe^{2+} , Fe^{3+} , and Zn^{2+} are 0.76 Å, 0.64 Å, and 0.74 Å, respectively. The replacement of Zn^{2+} in the ZnO lattice by Fe^{2+} or Fe^{3+} ions will lead to a lattice distortion. This effect of substitution due to the annealing atmosphere, explains the contraction or expansion of the unit cell.

Optical properties of a semiconductor have their origins in the intrinsic and extrinsic defects. Intrinsic defects are proper of the principal host while the extrinsic defects are related to dopants. Characteristically, defects represent one of the controversial areas of semiconductors, and ZnO is no exception. But, over the years, oxygen vacancies were believed to be the dominant shallow donors in ZnO.

PL spectra of pure and Fe-doped ZnO thin films evidenced the influence of the processing conditions on the type and concentration of different structural defects (Zn interstitials). This effect was attributed to the presence of trap states, which are associated with structural defects, due to incorporation of Zn ions in interstitial sites of host lattice and to the superficial defects.

PL spectra of pure and Fe-doped ZnO thin films evidenced the main emission band in the UV region. A shift of the exciton position in the Fe (II)-ZnO samples was observed. This shift was explained in terms of the dopants, which produce superficial defects causing changes in the

optical properties and an apparent increase in the band gap. When an electron is excited from the valence band it cannot fill these states because they are occupied and they can only go to a higher empty state inside the conduction band. An evident quenching effect was found for the annealed in air Fe (II)-ZnO thin films. The quenching-by-concentration effect observed was attributed due to the formation of trapping states by the dopant species.

The room temperature M-H measurements showed a paramagnetic response in almost all samples. It was attributed to concentrations that lie far below the percolation threshold. This is associated with nearest-neighbor cation coupling and above of this threshold there is a change in the magnetic features of the DMSs as a paramagnetic response. The observed response could be fostered by the existence of oxygen vacancies and the presence of zinc in the ZnO interstitial sites.

In turn, the Fe (III)-doped systems also produced significant results. The formation of pure and Fe doped ZnO thin films were confirmed by XRD, UV-Vis, and PL tests. No isolated impurity phases were detected. The Fe (III) dopant series, annealed in a controlled nitrogen atmosphere, with a correlation of dopant concentration, favored optical properties and retained suitable UV and violet PL intensities. The PL spectra of bare and Fe-doped ZnO thin films evidenced the main emission band in the UV region. A quenching-by-concentration effect was attributed to the formation of trapping states by the dopant species. Fe (III) doped ZnO thin films exhibited weak, but noticeable at room-temperature paramagnetism.

In general, all the films exhibited a weak paramagnetic behavior at room temperature while keeping good structural and optical properties. Despite the fact that ZnO has a short-range antiferromagnetic order, the weak behavior exhibited is attributed to the fact that the spins are not perfectly antiparallel so there is a weak canting moment of the sub-lattices producing a

macroscopic magnetization. But this phenomenon is still controversial; this weak magnetism can be an intrinsic magnetic property or an extrinsic one, due to impurities like hematite or magnetite. Consequently, the weak magnetic response in our samples cannot be attributed to those impurities or were not detectable in the XRD. This can also be confirmed by XRD patterns, which do not display these kind of impurity phases.

XRD graphs showed that nitrogen ions replaced oxygen ions when annealed in a controlled nitrogen atmosphere, as we expected. These procedure helps to control oxygen vacancies and defects, favoring photoluminescence properties. The paramagnetic signal comes from crystals whose sizes are in the range of 15 nm to 20 nm and were detectable and done at room-temperature MH loops of doped ZnO thin films.

The annealed nitrogen atmosphere samples showed a better control of oxygen vacancies and the defects associated to zinc interstitials, when compared with samples annealed in air. Furthermore, these nanostructures, open interesting possibilities for tuning the oxidation state of Fe doped ZnO in functional systems and devices. These materials are promising candidates for applications in spintronic, data storage devices, and magneto electric sensor devices. In both cases of Fe (II) and Fe (III) species, the dopants play an important role in the optical and magnetic properties. This can be attributed to the high oxygen vacancies in the ZnO host structure. These results open interesting possibilities to pursue of Fe-doped ZnO in functional systems and devices.

6 REFERENCES

- [1] Anderson Janotti and Chris G Van de Walle; Rep.Prog.Phys. 72(2009), Fundamentals of Zinc Oxide as a Semiconductor
- [2] Marco A. Gálvez Saldaña; Synthesis and Characterization of Nanostructured ZnO- and BiFeO₃-Based Multifunctional Materials, UPRM Thesis 2012
- [3] Jáuregui Rosas,Segundo; Effect of Eu³⁺ ions content on physical properties of nanocrystalline ZnO and Gd₂O₃, UPRM Thesis 2008
- [4] Martinez Julca, Milton A.; Effect of the Incorporation of Defects in ZnO Nanocrystals on the Generation of Reactive Oxygen Species for Applications in Photodynamic Therapy, UPRM Thesis 2015
- [5] G. Murtaza, Rai a,n, M.A.Iqbal a, Y.B.Xu b, I.G.Will b, Z.C.Huang; Study of Sm-doped ZnO sample sintered in a nitrogen atmosphere and deposited on nSi (100) by evaporation technique, Journal of Magnetism and Magnetic Materials 323 (2011) 3239 –3245
- [6] Kenji Ueda, Hitoshi Tabata, Tomoji Kawai, Magnetic and electric properties of transition-metal-doped ZnO films, Appl Phys Lett, 79, 988 (2001).
- [7] K. Ando¹ et al. Large magneto-optical effect in an oxide diluted magnetic semiconductor Zn_{1-x}CoxO, Appl. Phys. Lett. 78, 2700 (2001).
- [8] J. Hays et al. Effect of Co doping on the structural, optical and magnetic properties of ZnO Nanoparticles, J. Phys. Condens. Matter, 19, 266203 (2007).
- [10] Lee E-C, Kim Y-S, Jin Y-G and Chang K J 2001 Phys. Rev. B 64 085120
- [11] Harrison W A 1999 Elementary Electronic Structure (Singapore: World Scientific)
- [12] Minegishi K, Koiwai Y, Kikuchi Y, Yano K, Kasuga M and Shimizu A 1997 Japan. J. Appl. Phys. Part II 36 L1453
- [13] Look D C, Reynolds D C, Litton C W, Jones R L, Eason D B and Cantwell G 2002 Appl. Phys. Lett. 81 1830
- [14] Aoki T, Hatanaka Y and Look D C 2000 Appl. Phys. Lett.76 3257

- [15] Ryu Y R, Zhu S, Look D C, Wrobel J M, Yeong H M and White H W 2000 *J. Cryst. Growth* 216 330
- [16] Xiu F X, Yang Z, Mandalapu L J, Zhao D T and Liu J L 2005 *Appl. Phys. Lett.* 87 152101
- [17] Chu S, Lim J H, Mandalapu L J, Yang Z, Li L and Liu J L 2005 *Appl. Phys. Lett.* 92 152103
- [18] Tsukazaki A et al 2005 *Nature Mater.* 4 42
- [19] Limpijumnong S, Zhang S B, Wei S H and Park C H 2004 *Phys. Rev. Lett.* 92 155504
- [20] Carlos W E, Glaser E R and Look D C 2001 *Physica B* 308–310 976
- [21] Garces N Y, Giles N C, Halliburton L E, Cantwell G, Eason D B, Reynolds D C and Look D C 2002 *Appl. Phys. Lett.* 80 1334
- [22] Thonke K, Gruber Th, Teofilov N, Schöfelder R, Kerwien N, Waag A and Sauer R 2001 *Physica B* 308 945
- [23] Guo X-L, Choi J-H, Tabata H and Kawai T 2001 *Japan. J. Appl. Phys.* 40 L177
- [24] Meyer B K et al 2004 *Phys. Status Solidi b* 241 231
- [25] Lautenschlaeger S, Eisermann S, Meyer B K, Callison G, Wagner M R and Hoffmann A 2009 *Phys. Status Solidi RRL* 3 16
- [26] Fang Z-Q, Claflin B, Look D C, Lei Kerr L and Li X 2007 *J. Appl. Phys.* 102 023714
- [27] Fons P, Tampo H, Kolobov A V, Ohkubo M, Niki S, Tominaga J, Carboni R, Boscherini F and Friedrich S 2006 *Phys. Rev. Lett.* 96 045504
- [28] Van de Walle C G, Laks D B, Neumark G F and Pantelides S T 1993 *Phys. Rev. B* 47 9425
- [29] Kobayashi A, Sankey O F and Dow J D 1983 *Phys. Rev. B* 28 946
- [30] Chadi D J 1991 *Appl. Phys. Lett.* 59 3589
- [31] Lee W J, Kang J and Chang K J 2006 *Phys. Rev. B* 73 024117

[32] Structural studies of magnetic Fe doped ZnO nanofibers. Available from: https://www.researchgate.net/publication/259969867_Structural_studies_of_magnetic_Fe_doped_ZnO_nanofibers [accessed Jan 20 2018].

[33] Satyanarayana Talam,¹ Srinivasa Rao Karumuri,¹ and Nagarjuna Gunnam²; Synthesis, Characterization, and Spectroscopic Properties of ZnO Nanoparticles, Abstract ISRN Nanotechnology, Volume 2012, Article ID 372505

[34] <http://www.rigaku.com/> X-ray diffraction (XRD) instruments

[35] B. D. Cullity, Elements of X-ray Diffractions. Addison Wesley, MA, 1972, p. 102.

[36] Y. N. Konan, M. Berton, R. Gurny, and E. Allémann, “Enhanced photodynamic activity of meso-tetra(4-hydroxyphenyl)porphyrin by incorporation into sub-200 nm nanoparticles.” European journal of pharmaceutical sciences official journal of the European Federation for Pharmaceutical Sciences, vol. 18, no. 3–4, pp. 241–249, 2003.

[37] Yesusa K. Collantes Goicochea; Synthesis and Characterization of ZnO-based Nanostructures for Potential Biomedical Applications, UPRM Thesis 2013

[37] A. S. Risbud et al. Magnetism in polycrystalline cobalt-substituted zinc oxide, Physical Review B 68, 205202 (2003).

[38] J. M. D. Coey, M. Venkatesan, and C. B. Fitzgerald, Donor impurity band exchange in dilute ferromagnetic oxides, Nature Mater, 4, 173–179, (2005).

[39] K. Vanheusden, Correlation between photoluminescence and oxygen vacancies in ZnO phosphors, Appl. Phys. Lett. 68, 403, (1996).

[40] P. K. Samanta, Visible Emission from ZnO Nanorods Synthesized by a Simple Wet Chemical Method, International Journal of NanoScience and Nanotechnology ISSN 0974– 3081, 1, 81-90 (2009).

[41] Anderson Janotti, Chris G Van de Walle, Fundamentals of zinc oxide as a semiconductor, Rep. Prog. Phys. 72, 126501, (2009).

[42] Abdel-Baset TA, Fang YW, Anis B, Duan CG, Abdel-Hafiez M.; Structural and Magnetic Properties of Transition-Metal-Doped Zn_(1-x)Fe_xO. Nanoscale Res Lett. 2016 Dec; 11(1):115. doi: 10.1186/s11671-016-1332-x. Epub 2016 Feb 29.

- [43] A. Filipetti, V. Fiorentini, G. Capellini, A. Bosin. Anomalous relaxations and chemical trends at III-V semiconductor nitride nonpolar surfaces. *Phys. Rev. B.* 59, 8026 (1999).
- [44] U. zgör, I. Alivov, C. iu, a. Teke, M. a. Reshchikov, S. Do an, V. Avrutin, S.-J. Cho, and H. Morko , “A comprehensive review of ZnO materials and devices,” *Journal of Applied Physics*, vol. 98, no. 4, p. 041301, 2005.
- [45] Feng, C. Cheng, B. D. ao, N. Wang, and M. M. T. oy, “Photoluminescence study of single ZnO nanostructures: Size effect,” *Applied Physics Letters*, vol. 95, no. 5, p. 053113, 2009.
- [46] E.-S. Jeong, H.-J. Yu, Y.-J. Kim, G.-C. Yi, Y.-D. Choi, and S.-W. Han, “ocal structural and optical properties of ZnO nanoparticles.,” *Journal of Nanoscience and Nanotechnology*, vol. 10, no. 5, pp. 3562–3565, 2010.
- [47] Abdel-Baset TA1, Fang YW2, Anis B3, Duan CG2, Abdel-Hafiez M4, 5, 6. “Structural and Magnetic Properties of Transition-Metal-Doped Zn 1-x Fe x O”, *Nanoscale Res Lett.* 2016 Dec; 11(1):115. doi: 10.1186/s11671-016-1332-x. Epub 2016 Feb 29.
- [48] Vahak Marghussian, “The Effect of Temperature on Magnetic Behavior” *Nano-Glass Ceramics Processing, Properties and Applications*, Science Direct, 2015
- [49] C. Kittel, *Introduction to Solid State Physics*, Eighth edi. Hoboken, New Jersey: John Wiley and Sons, Inc, 2005.
- [50] Y. Q. Fu, J. K. Luo, X. Y. Du, A. J. Flewitt, Y. Li, G. H. Markx, A. J. Walton, and W. I. Milne, “Recent developments on ZnO films for acoustic wave based bio-sensing and microfluidic applications: a review,” *Sensors and Actuators B: Chemical*, vol. 143, no. 2, pp. 606–619, Jan. 2010.
- [51] T. Dietl et al. Zener Model Description of Ferromagnetism in Zinc-Blende Magnetic Semiconductors, *Science* 287, 1019 (2000).
- [52] K. Charles; *Introduction to Solid State Physics*. University of California, London Chapman & Hall, Ltd 8th edition (2005).
- [53] Talaat M. Hammad*, Stefan Griesing, Matthias Wotocek, Sylvia Kuhn, Rolf Hempelmann Uwe Hartmann and Jamil K. Salem; Optical and magnetic properties of Fe-doped ZnO nanoparticles prepared by the sol-gel method, *Int. J. Nanoparticles*, Vol. 6, No. 4, 2013

- [54] V. G. Il'ves, S. Yu. Sokovnin, and A. M. Murzakaev; Influence of Fe-Doping on the Structural and Magnetic Properties of ZnO Nanopowders, Produced by the Method of Pulsed Electron Beam Evaporation, *Journal of Nanotechnology*, Volume 2016, Article ID 8281247, 13 pages
- [55] Hall, J. R.; Hook, H. E. (1994). *Solid State Physics* (2nd Ed.). Chichester: Wiley. ISBN 0471928054.
- [56] Jullien, André; Guinier, Rémi (1989). *The Solid State from Superconductors to Superalloys*. Oxford: Oxford Univ. Press. ISBN 0198555547.
- [57] H. Morkoc, U. Özgür, *Zinc Oxide: Fundamentals, Materials and Device Technology*, Wiley-VCH Verlag GmbH Co, &Wienheim (2009).
- [58] Yamin Leprince-Wang. *Piezoelectric ZnO Nanostructure for Energy Harvesting*, Volume 1. Wiley-VCH Verlag GmbH Co, &Wienheim (2015).
- [59] G. A. Pasquevich, P. Mendoza Zelis, ´ 1 F. Golmar, S. P. Heluani, Sanjeev K. Nayak, Waheed A. Adeagbo, C. E. Rodriguez Torres,* Wolfram Hergert, Martin Hoffmann,4,5 Arthur Ernst, P. Esquinazi, and S. J. Stewart,) Oxygen-vacancy-induced local ferromagnetism as a driving mechanism in enhancing the magnetic response of ferrites, *PHYSICAL REVIEW B* 89, 104411 (2014)
- [60] U. zгүй, I. Alivov, C. iu, a. Teke, M. a. Reshchikov, S. Do an, V. Avrutin, S.-J. Cho, and H. Morko , “A comprehensive review of ZnO materials and devices,” *Journal of Applied Physics*, vol. 98, no. 4, p. 041301, 2005.
- [61] L. Feng, C. Cheng, B. D. ao, N. Wang, and M. M. T. oy, “Photoluminescence study of single ZnO nanostructures: Size effect,” *Applied Physics Letters*, vol. 95, no. 5, p. 053113, 2009.
- [62] E.-S. Jeong, H.-J. Yu, Y.-J. Kim, G.-C. Yi, Y.-D. Choi, and S.-W. Han, “ocal structural and optical properties of ZnO nanoparticles.” *Journal of Nanoscience and Nanotechnology*, vol. 10, no. 5, pp. 3562–3565, 2010.
- [63] V. A. Fonoberov and A. A. Balandin, “Optical Properties of Wurtzite GaN and ZnO Quantum Dots,” *Materials Research*, vol. 818, no. 11, pp. 1–6, 2004.
- [64] V. Ischenko, S. Polarz, D. Grote, V. Stavarache, K. Fink, and M. Driess, “Zinc Oxide Nanoparticles with Defects,” *Advanced Functional Materials*, vol. 15, no. 12, pp. 1945–1954, Dec. 2005.

[65] L. E. Halliburton, N. C. Giles, N. Y. Garces, M. Luo, C. Xu, L. Bai, and L. A. Boatner, "Production of native donors in ZnO by annealing at high temperature in Zn vapor," *Applied Physics Letters*, vol. 87, no. 17, p. 172108, Oct. 2005.

179

[66] D. Hofmann, A. Hofstaetter, F. Leiter, H. Zhou, F. Henecker, B. Meyer, S. Orlinskii, J. Schmidt, and P. Baranov, "Hydrogen: A Relevant Shallow Donor in Zinc Oxide," *Physical Review Letters*, vol. 88, no. 4, p. 045504, Jan. 2002.

[67] H. Morko and U. zгүй, *Zinc Oxide: Fundamentals, Materials and Device Technology*. Wiley-VCH, 2008.

[68] T.SrinivasuluK.SarithaK.T. Ramakrishna Reddy; Synthesis and characterization of Fe-doped ZnO thin films deposited by chemical spray pyrolysis, *Modern Electronic Materials* Volume 3, Issue 2, June 2017, Pages 76-85

[69] Nam-Trung Nguyen; *Micromixers: Fundamentals, Design and Fabrication*, A volume in *Micro and Nano Technologies* • 2nd Edition • Copyright © 2012 Elsevier Inc.

[70] A.P. Rambu, V. Nica, M. Dobromir; Influence of Fe-doping on the optical and electrical properties of ZnO films, *Superlattices Microstruct.*, 59 (2013), pp. 87-96

[71] U. Alver, T. Kilinc, E. Bacaksiz, S. Nezir; Structural and optical properties of Zn_{1-x}Fe_xO thin films prepared by ultrasonic spray pyrolysis, *Mater. Sci. Eng.*, 138 (2007), pp. 74-77

[72] T. A. Abdel-Baset, Yue-Wen Fang, B. Anis, Chun-Gang Duan, and Mahmoud Abdel-Hafiez; Structural and Magnetic Properties of Transition-Metal-Doped Zn_{1-x}Fe_xO, *Nanoscale Res Lett*. 2016; 11: 115.

[73] S. Shionoya and W. M. Yen, *Phosphor Handbook*. Boca Raton, Florida: Phosphor Research Society, 1997.

[74] W. Shan, W. Walukiewicz, J.W. Ager, K.M. Yu, H. Yuan, H.P. Xin, G. Cantwell, J.J. Song, Nature of room temperature photoluminescence in ZnO, *Appl. Phys.Lett.* 86 (2005) 191911–191913.

[75] K. Uma, S. Ananthakumar, R.V. Mangalaraja, K.P.O. Mahesh, T. Soga, T. Jimbo, A facile approach to hexagonal ZnO nanorod assembly, *J. Sol.-Gel Sci. Technol.* 49(2009) 1–5.

- [76] H. Morko and U. zgör, Zinc Oxide: Fundamentals, Materials and Device Technology. Wiley-VCH, 2008.
- [77] H. Chen, J. Ding, Sh. Ma. Violet and blue-green luminescence from Ti-doped ZnO films deposited by RF reactive magnetron sputtering. *Superlattices and Microstructures* 49, 176–182 (2011).
- [78] S. M. Hatch¹, J. Briscoe¹, A. Sapelkin, W. P. Gillin, J. B. Gilchrist, M. P. Ryan, S. Heutz, and S. Dunn, Influence of anneal atmosphere on ZnO-nanorod photoluminescent and morphological properties with self-powered photodetector performance, *Journal of Applied Physics* 113, 204501 (2013)
- [79] S. Abdullahi, M. Momoh and H. N. Yahya; Influence of nitrogen annealing on the structural and electrical properties of zinc oxide (ZnO) thin film deposited by radio frequency magnetron sputtering technique, *IOSR Journal Of Environmental Science, Toxicology And Food Technology (IOSR-JESTFT)* e-ISSN: 2319-2402, p- ISSN: 2319-2399. Volume 4, Issue 4 (May. - Jun. 2013), PP 81-85
- [80] K. J. Chen, T. H. Fang, F. Y. Hung, L. W. Ji, S. J. Chang, S. J. Young, and Y. J. Hsiao, “The crystallization and physical properties of Al-doped ZnO nanoparticles,” *Applied Surface Science*, vol. 254, no. 18, pp. 5791–5795, Jul. 2008.
- [81] V. Ischenko, S. Polarz, D. Grote, V. Stavarache, K. Fink, and M. Driess, “Zinc Oxide Nanoparticles with Defects,” *Advanced Functional Materials*, vol. 15, no. 12, pp. 1945–1954, Dec. 2005.
- [82] Chu DW, Zeng YP, Jiang DL. Synthesis and growth mechanism of Cr-doped ZnO single-crystalline nanowires. *Solid State Community*. 2007;143:308. doi: 10.1016/j.ssc.2007.05.036.
- [83] <http://microbeam.com/testing-analysis-methods/sem-morphological-analysis/>
- [84] <http://hyperphysics.phy-astr.gsu.edu/hbase/hframe.html>
- [85] A. Taabouche, A. Bouabellou, F. Kermiche, F. Hanini, S. Menakh, Y. Bouachiba, T. Kerdja, C. Benazzouz, M. Bouafia and S. Amara, "Effect of Substrates on the Properties of ZnO Thin Films Grown by Pulsed Laser Deposition," *Advances in Materials Physics and Chemistry*, Vol. 3 No. 4, 2013, pp. 209-213. doi: 10.4236/ampc.2013.34031

[86] Swee-Yong Pung, Kwang-Leong Choy¹, Xianghui Hou and Chongxin Shan Preferential growth of ZnO thin films by the atomic layer deposition technique, Nanotechnology, Volume 19, Number 43, Published 22 September 2008

[87] A.Wójcik, M.Godlewski., E.Guziewicz, R.Minikayev and W.Paszkowicz, Controlling of preferential growth mode of ZnO thin films grown by atomic layer deposition, Journal of Crystal Growth Volume 310, Issue 2, 15 January 2008, Pages 284-289

[88] Swee-Yong Pung, Nibong Tebal, Pulau Pinang, Malaysia, Kwang-Leong Choy and Xianghui Hou, Structural and optical properties of ZnO thin films deposited using atomic layer deposition technique, Proceedings of IWNA 2011, November 10-12, 2011

[89] Zsofi a Baji, Zoltan La' badi., Zsolt E. Horvath and Peter Barna , Nucleation and Growth Modes of ALD ZnO, 2012 ACS Publications, Cryst. Growth Des. 2012, 12, p.5615–p.5620

[90] Scriven, L.E. (2011). Physics and Applications of DIP Coating and Spin Coating. MRS Proceedings. 121. 10.1557/PROC-121-717.

[91] R. R. Reeber, “ Lattice parameters of ZnO from 4.2° to 296°K,” Journal of Applied Physics, vol. 41, no. 13, p. 5063, Dec. 1970.

[92] U. zгүй., I. Alivov, C. iu, a. Teke, M. a. Reshchikov, S. Do an, V. Avrutin, S.-J. Cho, and H. Morko , “A comprehensive review of ZnO materials and devices,” Journal of Applied Physics, vol. 98, no. 4, p. 041301, 2005

[93]Vibrational Sample Magnetometer;
<https://www.lakeshore.com/products/Vibrating-Sample-Magnetometer/Pages/Model-Landing.aspx>

[94] T. S. Heng, A. Kumar, C. S. Ong, Y. P. Feng, Y. H. Lu, K. Y. Zeng, and J. Ding, “Investigation of the non-volatile resistance change in noncentrosymmetric compounds.” Scientific reports, vol. 2, p. 587, Jan. 2012

[95] Frenkel exciton and Mott- Warnier exciton,
URL:http://www.oe.phy.cam.ac.uk/images/exciton_sketch.jpg

[96] J. Hays et al. Effect of Co doping on the structural, optical and magnetic properties of ZnO Nanoparticles, J. Phys. Condens. Matter, 19, 266203 (2007).

- [97] K.Sharmaa Ranu, K.Duttaa Avinash, C. Pandeya Samar Layekb, H.C.Vermab, Effect of iron doping concentration on magnetic properties of ZnO nanoparticles, *Journal of Magnetism and Magnetic Materials*, Volume 321, Issue 17, September 2009, Pages 2587-2591
- [98] Lv, Jinpeng, and Chundong Li. "Evidences of VO, VZn, and Oi Defects as the Green Luminescence Origins in ZnO." *Applied Physics Letters Appl. Phys. Lett.* 103.23 (2013): 232114. Web.
- [99] David Winarski, Synthesis and characterization of Transparent Conductive Zinc Oxide Thin Films by Sol-Gel Spin Coating Method, Thesis of Bowling Green State University, August 2015
- [100] Ton-That, C., L. Weston, and M. R. Phillips. "Characteristics of Point Defects in the Green Luminescence from Zn- and O-rich ZnO." *Physical Review B Phys. Rev.* B 86.11 (2012)
- [101] Look, D. C., G. C. Farlow, Pakpoom Reunchan, Sukit Limpijumnong, S. B. Zhang, and K. Nordlund. "Evidence for Native-Defect Donors in N -Type ZnO." *Phys. Rev. Lett.* *Physical Review Letters* 95.22 (2005): n. pag. Web.
- [102] Nature.com. Nature Publishing Group, n.d. Web. 10 June 2015.
<<http://www.nature.com/am/journal/2009/200906/full/am2009160a.html>>.
- [103] M.I. Khana, K.A. Bhattib, Rabia Qindeelc,†, Norah Alonizanc, Hayat Saeed Althobait, "Characterizations of multilayer ZnO thin films deposited by sol-gel spincoating technique." *Journal of Results in Physics: The online only, open access journal in Physics* <http://dx.doi.org/10.1016/j.rinp.2016.12.029>
- [104] N.J. Podraza, G.E. Jellison, Jr., *Ellipsometry, Encyclopedia of Spectroscopy and Spectrometry (Third Edition)*, 2017
- [105] Bakhtiar Ul Haq, R. Ahmed, A. Shaari, N. Ali , Y. Al-Douri , A.H. Reshak, "Comparative study of Fe doped ZnO based diluted and condensed magnetic semiconductors in wurtzite and zinc-blende structures by first-principles calculations", *Materials Science in Semiconductor Processing* 43 (2016) 123–128
- [106] Jacek Wojnarowicz, "Paramagnetism of cobalt-doped ZnO nanoparticles obtained by microwave solvothermal synthesis", *Beilstein J. Nanotechnol.* 2015, 6, 1957–1969. doi:10.3762/bjnano.6.200

- [107] Archita Mondal, Sanchari Sarkar, Neepamala Giri, Souvik Chatterjee, Ruma Ray; Magnetic Phase Separation in Diluted Magnetic System: $Zn_{1-x}Fe_xO$, Acta Metallurgica Sinica(English Letters), 2017, 30(6): 521-527
- [108] M.I. Khana, K.A. Bhattib; Characterizations of multilayer ZnO thin films deposited by sol-gel spin coating technique, Results in Physics Volume 7, 2017, Pages 651-655
- [109] K M Zakir Hossain, Uresha Patel, Ifty Ahmed; Development of microspheres for biomedical applications: A review, December 2014 DOI: 10.1007/s40204-014-0033-8
- [110] Asad Mahmood and Abdul Naeem; Sol-Gel-Derived Doped ZnO Thin Films: Processing, Properties, and Applications, <http://dx.doi.org/10.5772/67857>
- [111] A. El Amiri, R. Moubah, F. Lmai, M. Abid, N. Hassanain, E.K. Hlil and H. Lassri, Probing magnetism and electronic structure of Fe-doped ZnO thin films, Journal of Magnetism and Magnetic Materials, <http://dx.doi.org/10.1016/j.jmmm.2015.09.015>
- [112] T. Prasada Raoa*, S. Gokul Rajb , M. C. Santhosh Kumar, Effect of Annealing Atmosphere on Structural and Optical Properties of Nd:ZnO Thin Films; Procedia Materials Science (2014) 1631 – 1638
- [113] Huai-Shan Chin and Long-Sun Chao; The Effect of Thermal Annealing Processes on Structural and Photoluminescence of Zinc Oxide Thin Film, Journal of Nanomaterials, Volume 2013
- [114] Sessa VempatiEmail author, Joy Mitra and Paul Dawson; One-step synthesis of ZnO nanosheets: a blue-white fluorophore, Nanoscale Research Letters, 2012, 7:470 <https://doi.org/10.1186/1556-276X-7-470>
- [115] Davoud Dorrnian & Atefeh Fotovat Eskandari (2015) Effect of Laser Fluence on the Characteristics of ZnO Nanoparticles Produced by Laser Ablation in Acetone, Molecular Crystals and Liquid Crystals, 607:1, 1-12, DOI: 10.1080/15421406.2014.927414
- [116] S. Riaz, S. Naseem and Y. B. Xu; Room temperature ferromagnetism in sol-gel deposited un-doped ZnO films, J Sol-Gel Sci Technol (2011) 59:584–590, DOI 10.1007/s10971-011-2532-6